UNIVERSIDADE FEDERAL DO CEARÁ
CENTRO DE TECNOLOGIA
DEPARTAMENTO DE ENGENHARIA METALÚRGICA E DE MATERIAIS
PROGRAMA DE PÓS-GRADUAÇÃO EM ENGENHARIA E CIÊNCIA DE MATERIAIS
CURSO DE MESTRADO EM ENGENHARIA E CIÊNCIA DE MATERIAIS

ANA BEATRIZ FERREIRA SOUSA

WELDABILITY EVALUATION OF CORROSION-RESISTANT ALLOY WELD METALS FOR HIGH-TEMPERATURE SERVICE IN OIL AND GAS INDUSTRY USING TRANS-VARESTRAINT TEST

FORTALEZA
2024

ANA BEATRIZ FERREIRA SOUSA

WELDABILITY EVALUATION OF CORROSION-RESISTANT ALLOY WELD METALS FOR HIGH-TEMPERATURE SERVICE IN OIL AND GAS INDUSTRY USING TRANS-VARESTRAINT TEST

Thesis submitted to the Post-Graduate Program in Engineering and Materials Science of the Universidade Federal do Ceará, in partial fulfilment of the requirements for the degree of Master in Materials Science and Engineering.
Concentration area: Physical and Mechanical Properties of Materials.

Advisor: Prof. Dr. Cleiton Carvalho Silva

FORTALEZA
2024

Dados Internacionais de Catalogação na Publicação
Universidade Federal do Ceará
Sistema de Bibliotecas
Gerada automaticamente pelo módulo Catalog, mediante os dados fornecidos pelo(a) autor(a)

S696w Sousa, Ana Beatriz Ferreira.
Weldability Evaluation of Corrosion-Resistant Alloy Weld Metals for High-Temperature Service in Oil And Gas Industry Using Trans-Varestraint Test / Ana Beatriz Ferreira Sousa. – 2024.
139 f. : il. color.

Dissertação (mestrado) – Universidade Federal do Ceará, Centro de Tecnologia, Programa de Pós-Graduação em Engenharia e Ciência de Materiais, Fortaleza, 2024.
Orientação: Prof. Dr. Cleiton Carvalho Silva.

1. austenitic stainless steel. 2. dissimilar welding. 3. solidification cracks. 4. Trans-Varestraint test. 5. microstructural characterisation. I. Título.

CDD 620.11

ANA BEATRIZ FERREIRA SOUSA

WELDABILITY EVALUATION OF CORROSION-RESISTANT ALLOY WELD METALS FOR HIGH-TEMPERATURE SERVICE IN OIL AND GAS INDUSTRY USING TRANS-VARESTRAINT TEST

Thesis submitted to the Post-Graduate Program in Engineering and Materials Science of the Universidade Federal do Ceará, in partial fulfilment of the requirements for the degree of Master in Materials Science and Engineering.
Concentration area: Physical and Mechanical Properties of Materials.

Advisor: Prof. Dr. Cleiton Carvalho Silva

Approved at: 26/07/2024.

EXAMINING COMMISSION

_____
Prof. Dr. Cleiton Carvalho Silva (Advisor)
Universidade Federal do Ceará (UFC)

_____
Prof. Dr. Hélio Cordeiro de Miranda
Universidade Federal do Ceará (UFC)

_____
Prof. Dr. Antonio Jose Ramirez Londono
The Ohio State University (OSU)

To myself.

ACKNOWLEDGEMENTS

To my parents, Paula Andrea and Pedro Henrique, who have put in so much effort to ensure a great education for their children. Thank you for understanding my desire for postgraduate studies and for always caring about me. I cannot imagine achieving this dream without your help. To my sister, Bianca, for letting me know that my academic journey is somehow an inspiration to her. This is a privilege. I admire you so much! I promise I will continue to work hard.

I would like to express my immense gratitude to my advisor, Professor Cleiton Carvalho Silva, for his excellent guidance in my academic journey. Thank you for your careful support since I was an undergraduate student. I appreciate your belief in my potential and your constant availability for teaching and discussion. Our conversations have significantly contributed to my improvement and inspired me to pursue my goals.

To the members of the examining commission, Professor Hélio Cordeiro de Miranda and Professor Antonio Jose Ramirez Londono, thank you for your invaluable contributions to the improvement of this thesis.

To the Universidade Federal do Ceará (UFC), especially to the professors from the Departamento de Engenharia Metalúrgica e de Materiais (DEMM), who have been essential in my trajectory.

To the Laboratório de Pesquisa e Tecnologia em Soldagem (LPTS) of the UFC for providing the materials and equipment necessary for the development of this research. I extend my sincere gratitude to Professor Émerson Mendonça Miná for his invaluable guidance during my initial steps in Scanning Electron Microscopy. I also want to acknowledge the talented welder Cleiton de Paulo Gonçalves and the master's degree student Izaac Oliveira Andrade for assistance during the practical activities of this work. Additionally, I am sincerely thankful to the undergraduate students who supported me throughout this period, Francisco Edmar Cavalcante Neto and Jenifer Sofia de Souza. I hope I was able to impart knowledge to you, as I learned so much from working with you. Thank you for your excellent work.

To my beloved friends Daniely, Marcela, and Bruno. The time I spent with you has cured me from the routine. Thanks! This acknowledgement extends to all my friends. Sharing moments with you is what keeps me sane.

To my esteemed colleague, Breno Rabelo, for sharing with me all the joys and challenges of pursuing the master's degree. Taking classes and studying together with you was truly a pleasure. You inspire me so much.

To my significant other, Lucas Alves de Moraes, for unconditionally believing in my potential. I did not realise someone could cheer so much for another person until I met you. Thank you for trusting me even when I could not trust myself. I love you deeply. Thank you for all our conversations (both the scientific ones and especially the personal ones) and for always being by my side. I will always be here for you too.

I would also like to thank the Central Analítica of the UFC (funded by FINEP-CT-INFRA, CAPES-Pró-Equipamentos, and MCTI-CNPq-SisNano2.0) for enabling the use of its microscopy installations.

To the Laboratório de Aço e Gusa of the ArcelorMittal Pecém for the use of their equipment for chemical analysis of the fusion zones aiming to determinate precisely the C, N, P, and S contents.

To the Programa de Recursos Humanos da Agência Nacional do Petróleo, Gás Natural e Biocombustíveis (PRH/ANP), which is provided with investment resources from oil companies qualified under the P, D&I Clause of ANP Resolution 50/2015, for financial support through a master's scholarship.

To the São Paulo Research Foundation (FAPESP) for the support through the grant #2024/12179-0.

To the Coordination of Superior Level Staff Improvement (CAPES) and The National Council for Scientific and Technological Development (CNPq) for supporting the Graduate Program in Materials Science and Engineering of the UFC.

“Science is a way of thinking much more than it is a body of knowledge. Its goal is to find out how the world works, to seek what regularities there may be, to penetrate the connections of things.” (CARL SAGAN, 1979).

ABSTRACT

The flare in the oil and gas industry is responsible for burning harmful gases, ensuring safety. Flares are commonly made of austenitic stainless steels (ASSs), which are highly recommended for application at high temperatures and in reducing/oxidising atmospheres. Despite this, several failure cases of ASS components utilised in oil and gas production and refining have been reported in the literature, mostly related to metallurgical phenomena occurring due to harsh operation conditions. The processes of fabrication and repair per welding may also cause failures once the welding leads to nonequilibrium solidification, microsegregation of alloy elements, and potential rejection of impurities from the solid toward the interdendritic liquid, which are critical factors for the occurrence of solidification cracking. Therefore, this work aimed to assess the weldability through Trans-Varestraint Test (TVT) of consumable electrodes which can be employed in the fabrication and repair of flare components. The welds were made with the shielded metal arc welding (SMAW) using three filler metals: the ASS electrodes AWS E310-15 and AWS E347-17 and the nickel-based alloy electrode AWS ENiCrFe-2. The ASSs AISI 310S and AISI 304H were applied as the base metals. The TVTs was performed with strain levels ranging from 0.5% to 8%. The weldability was evaluated based on the susceptibility of the weld metal to solidification cracking, which was determined through the critical strain, saturated strain, maximum crack length, maximum crack distance, total crack length, and critical strain speed. Additionally, samples of the fusion zones resulting from each welded combination were investigated by light optical microscopy and scanning electron microscopy, with a focus on correlating the microstructural characteristics to the resistance to solidification cracking. Electron backscatter diffraction (EBSD) analysis was used to determine the effects of stress applied during TVT on the microstructures of the weld metals. Considering all the results analysed, the ranking from least to most susceptible to solidification cracking was as follows: (AISI 310S + AWS E347-17) > (AISI 304H + AWS E347-17) > (AISI 304H + AWS E310-15) > (AISI 310S + AWS E310-15) > (AISI 310S + AWS ENiCrFe-2) > (AISI 304H + AWS ENiCrFe-2). The weld metals most resistant to solidification cracking resulted from the tests with the AWS E347-17 electrode, for which solidification occurred in the primary ferrite/secondary austenite mode. These fusion zones consisted of a combination of austenite and δ-ferrite, and the presence of δ-ferrite is known to be beneficial for preventing solidification cracking. The welds with the AWS E310-15 electrode solidified in the fully austenitic mode, which is favourable for solidification cracking. The fusion zones of tests using the AWS ENiCrFe-2 filler metal were composed of the γ-Ni fcc phase, and evidence of the precipitation of Nb(C,N) was

found in the interdendritic volumes. The formation of secondary phases may have some influence on the cracking propensity, explaining the lower resistance to solidification cracking of these weld metals. The EBSD results showed higher misorientation levels surrounding the cracks and on subgrain boundaries. This may be attributed to the severe deformation level at which the microstructure was subjected to cracking. The regions where dislocations accumulate eventually became subgrain boundaries.

Keywords: austenitic stainless steel; dissimilar welding; solidification cracks; Trans-Varestraint test; microstructural characterisation.

RESUMO

Em plataformas e refinaria de petróleo, o *flare* (queimador) é o equipamento responsável pela queima de gases residuais, garantindo a segurança operacional. *Flares* são comumente fabricados com aços inoxidáveis austeníticos, os quais são altamente recomendados para aplicação em alta temperatura e em atmosferas redutoras/oxidantes. Apesar disso, a literatura reporta diversos casos de falha de componentes de aço inoxidável austenítico utilizados no contexto de produção e refino de petróleo e gás. Em sua maioria, estes casos de falha estão relacionados a fenômenos metalúrgicos que ocorrem devido às condições extremas de operação. Os processos de fabricação e reparo por soldagem também podem ocasionar falhas, uma vez que resultam em uma solidificação fora do equilíbrio, na microssegregação de elementos de liga e na potencial rejeição de impurezas do sólido para o líquido interdendrítico, que são fatores críticos para a ocorrência de trincas de solidificação. Portanto, estre trabalho objetivou avaliar a soldabilidade de eletrodos consumíveis candidatos ao emprego na fabricação e reparo de componentes de flares por meio de uma modificação do ensaio Trans-Varestraint. As soldagens foram realizadas pelo processo Eletrodo Revestido, usando três metais de adição: os eletrodos de aço inoxidáveis austeníticos AWS E310-15 e AWS E347-17 e o eletrodo de liga de níquel AWS ENiCrFe-2. Os aços inoxidáveis austeníticos AISI 310S e AISI 304H foram selecionados como metais base. Os ensaios Trans-Varestraint foram realizados com sete níveis de deformação, de 0.5% a 8%. A soldabilidade foi avaliada em termos da susceptibilidade a trincas de solidificação, determinada por meio da deformação crítica, da deformação de saturação, do tamanho máximo de trinca, da distância máxima de trinca, do tamanho total das trincas e da taxa de deformação crítica. Ademais, amostras das zonas fundidas resultantes de cada combinação soldada foram investigadas pelas técnicas de microscopia óptica e de microscopia eletrônica de varredura, objetivando correlacionar as características microestruturais à resistência a trincas de solidificação. Análises por Difração de Elétrons Retroespalhados (EBSD) foram utilizadas para fornecer informações sobre os efeitos da tensão aplicada durante o TVT na microestrutura dos metais de solda. Considerando todos os resultados analisados, o ranking de solda menos a mais suscetível a trincas de solidificação é: (AISI 310S + AWS E347-17) > (AISI 304H + AWS E347-17) > (AISI 304H + AWS E310-15) > (AISI 310S + AWS E310-15) > (AISI 310S + AWS ENiCrFe-2) > (AISI 304H + AWS ENiCrFe-2). Os metais de solda mais resistentes a trincas de solidificação foram os resultantes de testes com o eletrodo AWS E347-17, para os quais a solidificação ocorreu no modo ferrita primária/austenita secundária. Estas zonas fundidas consistiram em uma combinação de austenita de ferrita-δ, e a presença de ferrita-

δ é conhecida por ser benéfica para prevenir o surgimento de trincas de solidificação. As soldas com o eletrodo AWS E10-15 solidificaram no modo completamente austenítico, o qual é favorável ao trincamento na solidificação. A zonas fundidas dos testes usando o eletrodo AWS ENiCrFe-2 como metal de adição é composta da fase cúbica de corpo centrado γ-Ni, e foram encontrados precipitados Nb(C,N) nos volumes interdendríticos. A formação de fases secundárias pode influenciar na propensão ao trincamento, explicando a baixa resistência a trincas de solidificação destes metais de solda. Os resultados de EBSD mostraram que altos níveis de *misorientation* nas adjacências das trincas e em contornos de subgrão. Isso pode ser justificado pelo severo grau de deformação ao qual a microestrutura é submetida no trincamento. As regiões onde as discordâncias se acumulam eventualmente se tornaram contornos de subgrão.

Palavras-chave: aços inoxidáveis austeníticos; soldagem dissimilar; trincas de solidificação; ensaio Trans-Varestraint; caracterização microestrutural.

LIST OF FIGURES

LIST OF TABLES

LIST OF ABBREVIATIONS AND ACRONYMS

AISI	American Iron and Steel Institute
ANOVA	Analysis of Variance
ASME	American Society of Mechanical Engineers
ASS	Austenitic Stainless Steel
AWS	American Welding Society
BTR	Brittle Temperature Range
CSS	Crack Strain Speed
DDC	Ductility-Dip Cracking
DTA	Differential Thermal Analysis
DTR	Ductility-dip Temperature Range
EBSD	Electron Backscattered Diffraction
EDS	Energy Dispersive X-ray Spectroscopy
FCC	Face Centred Cubic
FN	Ferrite Number
FZ	Fusion Zone
GTAW	Gas Tungsten Arc Welding
HAZ	Heat-Affected Zone
ISO	International Organization for Standardization
LOM	Light Optical Microscopy
MCD	Maximum Crack Distance
MCL	Maximum Crack Length
MGB	Migrated Grain Boundary
OES	Optical Emission Spectrometry
PMZ	Partially Melted Zone
SCTR	Solidification Cracking Temperature Range
SEM	Scanning Electron Microscopy
SGB	Solidification Grain Boundary
SMAW	Shielded Metal Arc Welding
SSGB	Solidification Subgrain Boundary
TCL	Total Crack Length
TVT	Trans-Varestraint Test

WRC	Welding Research Council
XRF	X-ray Fluorescence
ZDT	Zero Ductility Temperature
ZST	Zero Strength Temperature

LIST OF SIMBOLS

δ	Delta
γ	Gama
%	Percentage
®	Registered trademark

CONTENTS

1 INTRODUCTION

The oil and gas industry installations execute numerous operations involving phase transformation and chemical reactions. The processing in platforms and refineries results in the evolution of gases, which may cause overpressure in the systems. Therefore, the equipment in these installations utilises safety valves to promote pressure relief when needed. Once released by valves, residual gases flow through pipes to the flare, an essential component for ensuring operational and environmental security.

A flare is the equipment responsible for safely burning gases that arise from pressure relief events in the system, harmful gases, unneeded gases, and light liquids. In platforms and refineries, this activity is called “flaring”, and it guarantees the combustion or appropriate dispersion of hydrocarbons and other extremely toxic and corrosive gases into the atmosphere, such as carbon dioxide (CO_2), hydrogen sulfide (H_2S), sulphur dioxide (SO_2), chlorine (Cl_2), and hydrogen chloride (HCl) (Mahdi, Esmaeili, 2020; Shore, 1996).

The flare stack flam91e must be lit up during platform or refinery operation. However, oil and gas production platforms usually have only one flare designed to dispose of the discharge gases generated throughout the industrial unit. Hence, any failure that extinguishes the stack flame or any occurrence that renders the flare inoperative results in an emergency shutdown procedure, resulting in millions of dollars of financial loss.

Due to the critical service conditions, high temperature and carbonaceous reducing/oxidising atmosphere, flare tips are commonly manufactured using austenitic stainless steels. The most commonly employed alloy is AISI 310S, which is highly recommended for this application. Nonetheless, several failure cases of austenitic stainless steel components in the oil and gas production and refining context have been reported in the literature. The degradation or failure of flares is often related to metallurgical phenomena (e.g., sensitisation, carburising, sigma phase precipitation, stress corrosion cracking, carbides, and hydrogen embrittlement) (Kaewkumsai, Khonraeng, Sathirachinda, 2013; Pardal et al., 2011; Neuharth, Cavalli, 2015; Yousefi, Farghadin, Farzadi, 2015).

Some of the metallurgical phenomena mentioned are consequences of thermal fatigue flare components, which are exposed to high temperatures for long periods. The cyclic loads may result in crack nucleation and propagation. However, many other flare production and operation characteristics must be considered. Fabrication or repair processes per weld, for instance, may also cause failures, as nonequilibrium solidification implies microsegregation of alloy elements and insertion of impurity elements in the weld metal, both of which are critical

factors for the nucleation and propagation of solidification cracks (Katayama, Fujimoto, Matsunawa, 1985).

The weldability definition covers various characteristics of a material subjected to welding, such as its physical properties, mechanical properties, and susceptibility to metallurgical degradation. These characteristics are usually determined by their susceptibility to cracking during welding or subsequent heat treatment (Lippold, 2005). Thus, the weldability of the material is related to its resistance to solidification cracking (Dupont, Lippold, Kiser, 2009). An adequate evaluation of solidification cracking susceptibility requires performing weldability tests. Augmented restraint tests, in which an external load induces weld pool deformation, are largely employed. These methods allow variations in test severity by applying different strain rates (Campbell, Walsh, 1993).

The Trans-Varestraint test (TVT) is one of the main augmented restraint tests (ISO TR 17641-3, 2005). It aims to analyse solidification cracking precisely (Lippold, 2005; Kannengiesser, Boellinghaus, 2014). Researchers from Osaka University developed this test, which consists of submitting a specimen to flexural loading towards the end of the welding process to deform the weld pool and its adjacencies according to a predefined strain. Flexural loading is carried out perpendicular to the welding direction; the load is applied to cross the weld bead, inducing crack formation restricted to the fusion zone (Senda et al., 1971; Arata, Matsuda, 1971; Matsuda, Arata, Katayama, 1976; Arata et al., 1977).

Considering the above discussion, this work aimed to evaluate the weldability of consumable electrodes that can be applied in the oil and gas industry to manufacture or repair flare components using Trans-Varestraint test. The austenitic stainless steels AISI 310S and AISI 304H were selected as the base metals, and the welds were executed by the shielded metal arc welding (SMAW) process utilising the austenitic stainless steel electrodes AWS E310-15 and AWS E347-17 and the nickel electrode AWS ENiCrFe-2.

Modified Trans-Varestraint tests were performed to determine the susceptibility of the samples to solidification cracks. The solidification cracks resulting from the TVTs were analysed by macrostructural and microstructural characterisation techniques to evaluate the influence of changes in chemical composition, solidification path and resulting microstructure caused by the dissimilarity between filler and base metals on solidification crack susceptibility. The main goal is to contribute to understanding the metallurgical aspects associated with solidification cracking in the dissimilar welds of corrosion-resistant alloys for service at high temperatures.

The present research is part of a contracted demand of the Centro de Pesquisas Leopoldo Américo Miguez de Mello (CENPES/PETROBRAS) to the Laboratório de Pesquisa e Tecnologia em Soldagem (LPTS) of the Universidade Federal do Ceará (UFC) and financially supported by the Programa de Recursos Humanos da Agência Nacional do Petróleo, Gás Natural e Biocombustíveis (PRH/ANP), provided with the investment resources of oil companies qualified in the P, D&I Clause of ANP Resolution 50/2015.

1.1 Objectives

1.1.1 General objective

The purpose of this work is to evaluate the weldability of austenitic stainless steels and nickel consumable electrodes that can be employed in the oil and gas industry to manufacture or repair flare tips using Trans-Varestraint test and macrostructural and microstructural characterisation techniques.

1.1.2 Specific objectives

I. To evaluate the weldability through the Trans-Varestraint test of welds produced by the SMAW process using austenitic stainless steels AISI 310S and AISI 304H as the base metals and the AWS E310-15, AWS E347-17, and AWS ENiCrFe-2 electrodes as filler metals. Thus, to define the more adequate weld combination in terms of preventing solidification cracking;

II. To determine the solidification route of the weld metal resulting from each combination of base and filler metal via thermodynamic simulation and differential thermal analysis (DTA). In addition, to utilise this analysis results to calculate the brittle temperature range (BTR) and the solidification range (ΔT_{sol}) of the weld metals;

III. To analyse the microstructural, microchemical, and crystallographic aspects of weld metal fusion zones and their effects on resistance to solidification cracking utilising light optical microscopy (LOM) and scanning electron microscopy (SEM), principally energy-dispersive X-ray spectroscopy (EDS) and electron backscattered diffraction (EBSD).

1.2 Thesis structure

This thesis consists of five chapters to fulfil the Master's degree in Materials Science and Engineering requirements, according to the rules of the Post Graduation in Materials Science and Engineering, of the Department of Metallurgical and Materials Engineering of the Universidade Federal do Ceará (UFC).

Chapter 1 encompasses the introduction section, which contains elucidations of the scientific context and relevance of this thesis. The established objectives are also presented. Chapter 2 consists of a literature review, which highlights the concepts necessary for the comprehension of this thesis. This chapter presents an overview of the solidification behaviour of austenitic stainless steel welds. Moreover, definitions related to solidification crack susceptibility and to the Trans-Varestraint weldability test are discussed.

Chapter 3 is written according to the structure of the research paper. The results from Trans-Varestraint test, thermodynamic simulation, differential thermal analysis, and light optical microscopy are presented and discussed. Chapter 4 is the second research paper. It contains a detailed microstructural analysis of the weld metals, principally executed through EBSD and energy dispersive X-ray spectroscopy (EDS) techniques. Chapter 5 summarises the conclusions obtained from the two papers.

To enhance comprehension of the structure of this thesis, a flowchart illustrating the research stages is presented in Figure 1.

Figure 1 — Flowchart of the thesis's development stages

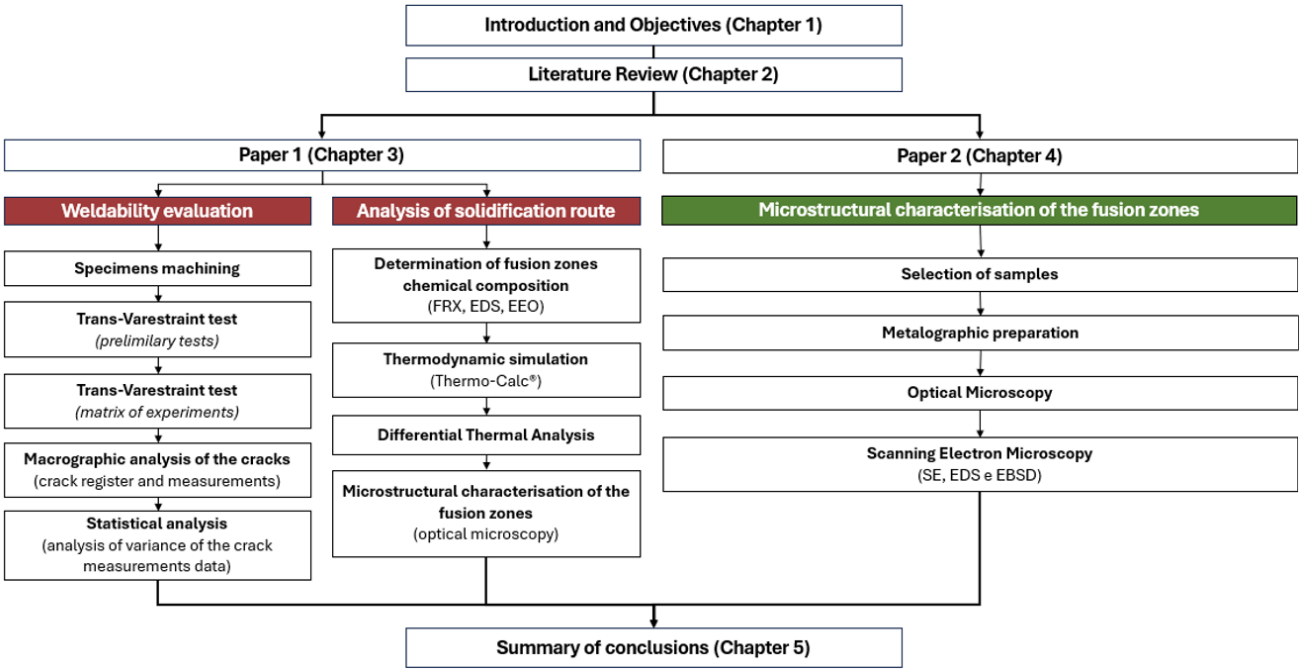

Source: elaborated by the author.

2 LITERATURE REVIEW

This chapter provides the necessary knowledge underlying the issues addressed in this thesis. Section 2.1 reviews weld metal solidification and microsegregation. Section 2.2 presents the solidification behaviour of austenitic stainless steel welds, followed by a discussion of the solidification mode in subsection 2.2.1. A more detailed explanation of solidification cracks is given in Section 2.3. The weldability concept and the Trans-Varestraint weldability test are described in Section 2.4. Section 2.5 provides an overview of SMAW.

2.1 Weld metal solidification

Solidification cracks are known to form in fusion zone solidification grain boundaries (SGBs) and solidification subgrain boundaries (SSGBs) due to several factors and are known to be among the most common defects in austenitic stainless steel welds (Brooks, Thompson, 1991; Sutton, 2013). To further evaluate the solidification cracking susceptibility of these alloys, first, it is crucial to understand some of the phenomena and mechanisms involved in weld metal solidification.

Welding arc processes, such as SMAW, imply a concentrated heat flux in the material, resulting in transient temperature gradients in the weld pool. The temperatures in the weld centre are greater than those reached in the extremities and vary as welding proceeds. Another consequence of the welding process is the high cooling rate, which leads to nonequilibrium solidification. Consequently, nonequilibrium solidification influences the microstructure of the fusion zone, affecting its mechanical properties (Kou, 2002; Safari, Forouzan, Shamanian, 2012).

The correlation between the welding parameters and the welded material characteristics is well known. For example, the cooling rate, the velocity of nucleation, and the supercooling temperature are directly related to the morphology of grain growth in the fusion zone and the intensity of the microsegregation phenomenon (Katayama, 2000).

The solidification process consists of the nucleation and growth of the solid phase at an advancing solid–liquid interface (Nelson, Lippold, Mills, 1999). Generally, crystal nucleation in the fusion zone is epitaxial, started by the arrangement of the atoms that constitute the liquid phase in the crystalline substrate, causing the substrate to grow without changes in its crystallographic orientation, as shown in Figure 2. The grain growth initiates from the substrate at the fusion line, where the weld pool wets adjacent grain boundaries and has many nucleation sites. Afterwards, competitive growth proceeds to the weld centre; grains not

preferentially oriented along the heat flow gradient direction tend to be suppressed by grains whose easy growth direction is more adequately oriented towards the heat flux (Nelson, Lippold, Mills, 1999; Kou, 2002; Sutton, 2013).

Figure 2 — Epitaxial nucleation and competitive growth in the weld fusion zone

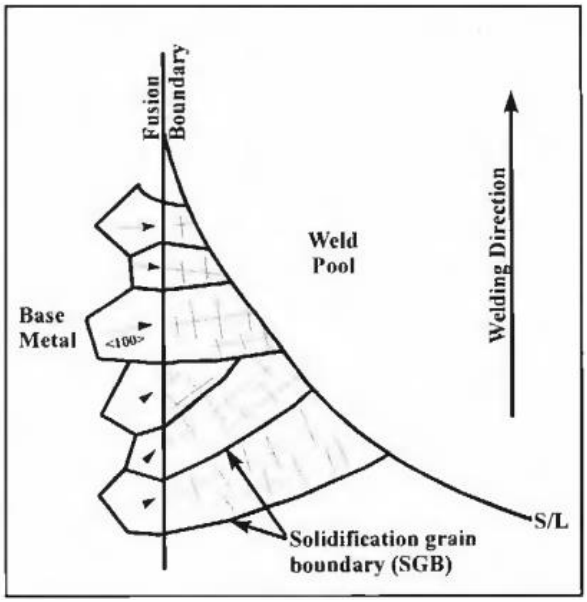

Source: Nelson, Lippold, and Mills (1999).

Unless subjected to severe thermal undercooling, a pure metal presents a planar solid–liquid interface (Kou, 2002). However, other interfaces may be obtained due to planar interface instability (Sutton, 2013). The formation of solidification substructures related to nonplanar interfaces is favoured for low thermal gradients and by solute enrichment in the liquid adjacent to the solid–liquid interface (Modenesi, Marques, Santos, 2012). Thus, following the solidification conditions, chemical composition, and other essential solidification parameters, such as the crystal growth rate (R) and liquid temperature gradient (G), a solid–liquid interface for an alloy can advance during solidification by having a planar, cellular or dendritic morphology. The dendritic interface may be cellular dendritic, columnar dendritic or equiaxed dendritic, as presented in Figure 3 (Kou, 2002; Sutton, 2013).

The formation of the morphologies presented in Figure 2b-d (i.e., the disruption of a planar solid–liquid interface) can be described by constitutional supercooling theory (Kou, 2002).

Figure 3 — Solid–liquid interfaces: (a) planar, (b) cellular, (c) cellular dendritic, (d) columnar dendritic, and (e) equiaxed dendritic

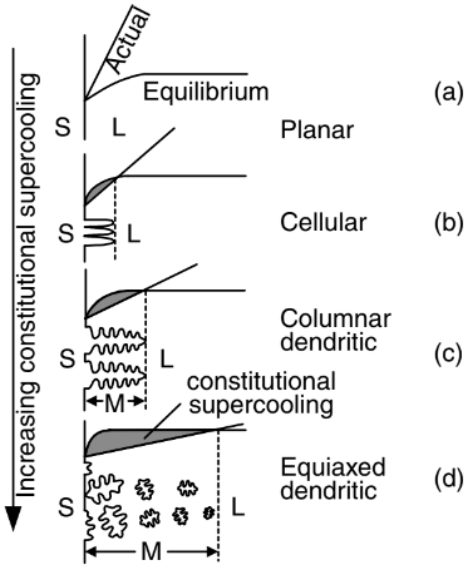

Source: Kou (2002).

2.1.1 Constitutional supercooling

The theory of constitutional supercooling was developed in the works of Rutter and Chamler (1953) and Tiller et al. (1953), and it considers only thermodynamic aspects for describing the breakdown of a planar solid–liquid interface during solidification (Kou, 2002).

Figure 4a shows a schematic of the solidification of an alloy at steady state with a planar solid–liquid interface (S/L). This schematic shows a situation in which the solute atoms in the solid phase segregate to the solid–liquid interface during the solidification, causing them to accumulate in the liquid phase. As presented in Figure 4b-c, the solute accumulation in the liquid phase does not occur uniformly. Regions closer to the solid–liquid interface are composed of a supersaturated liquid solute, which has a range of lower freezing points than that of the bulk liquid and has a composition Co/k. Here, Co is the nominal composition of the material and k is the partition coefficient. The partition coefficient is expressed in Equation 1, where C_{solid} is the solid composition and C_{liquid} is the composition of liquid.

$$k = \frac{C_{solid}}{C_{liquid}} \qquad \text{(Equation 1)}$$

Figure 4 — Constitutional supercooling: (a) solute-rich boundary layer, (b) phase diagram, (c) composition profile in liquid, and (d) liquidus temperature profile in liquid

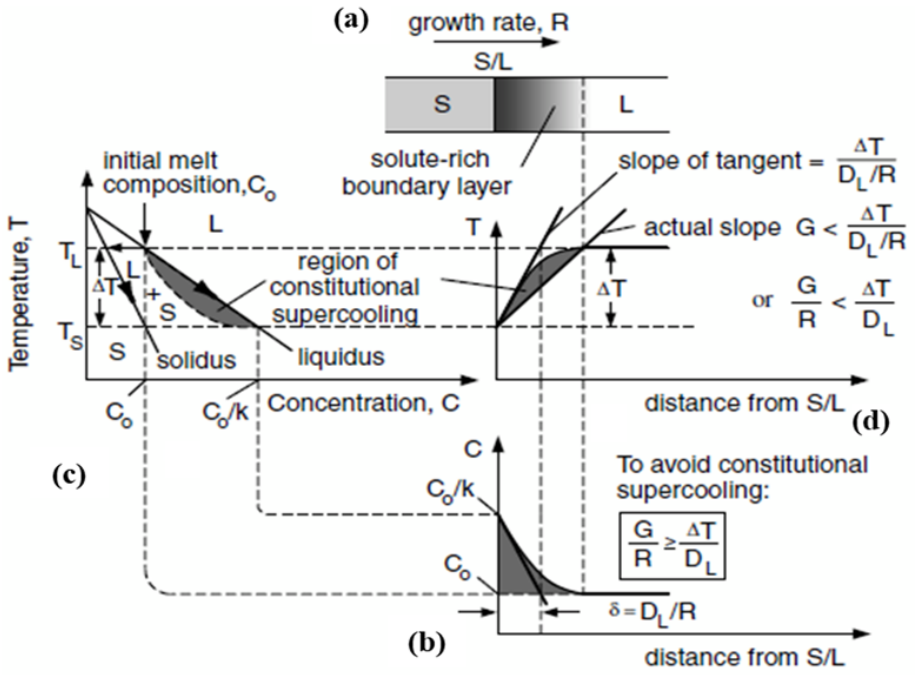

Source: Kou (2002), adapted.

No solute segregation is experienced by the liquid more distant from the solid–liquid interface. Thus, its composition remains unaltered, and its freezing point is still equal to that of the bulk liquid (Kou, 2002; Sutton, 2013). Figure 4d shows the difference between the *liquidus* and *solidus* temperatures according to the distance from the solid–liquid interface. The upper line is the slope of the tangent corresponding to the lower *liquidus* temperature, which means that a higher temperature gradient exists inside the boundary layer. As explicit in Equation 2, this liquid temperature gradient (G) is the ratio between the alloy equilibrium freezing range (ΔT), which consists of the difference between the *liquidus* and *solidus* temperatures, and the width of the solute-rich boundary layer. In turn, the solute-rich boundary layer is defined as the ratio of the diffusion coefficient of solute in liquid (DL) to the solid growth rate (R) (Kou, 2002).

$$G \geq \frac{\Delta T}{D_L/R} \qquad \text{(Equation 2)}$$

Equation 3 is a rearrangement of Equation 2. When Equation 3 is satisfied, the planar solidification mode is predominant (Kou, 2002).

$$\frac{G}{R} \geq \frac{\Delta T}{D_L} \qquad \text{(Equation 3)}$$

As solidification progresses, G decreases and R decreases. Therefore, if G decreases in a rate greater than the solidification speed, the G/R ratio becomes lower than that on the right side of Equation 3. This results in planar solid–liquid interface disruption. The liquid is then supercooled. With decreasing G/R, the solidification mode changes in the following sequence: planar > cellular > cellular dendritic > columnar dendritic > equiaxed dendritic (Kou, 2002; Sutton, 2013). The effect of G/R on the solidification morphology is shown in Figure 5.

Figure 5 — Relationships between the temperature gradient, solidification rate, and resulting grain size and morphology of a solidified microstructure

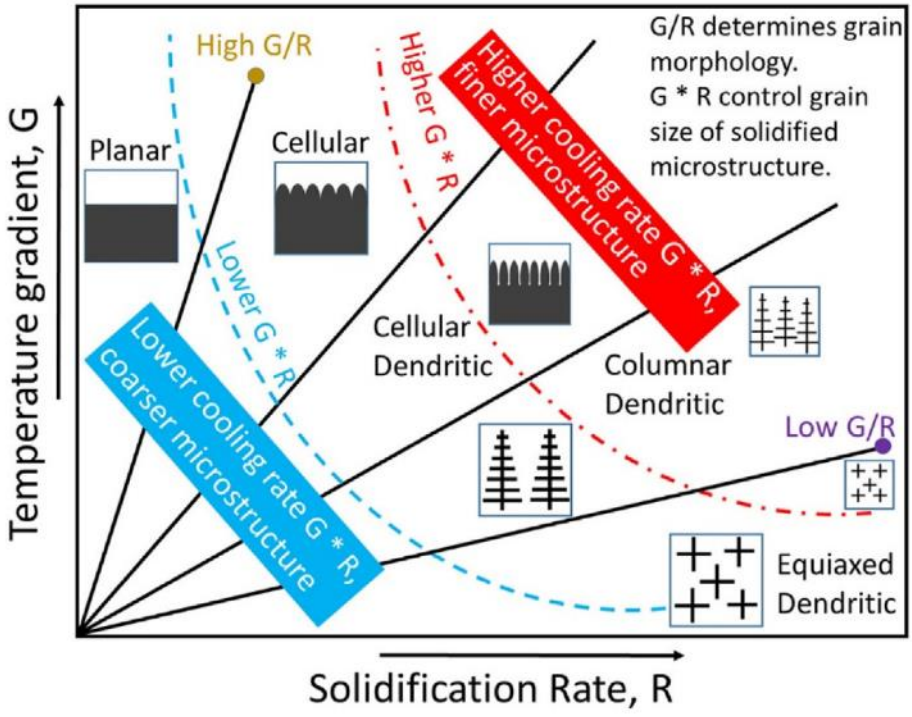

Source: Kou (2002) and Saboori et al. (2020).

2.1.2 Microsegregation

Solute elements with partition coefficients lower than 1 (meaning that their concentrations are higher in the liquid phase than in the solid phase) are rejected during the formation and growth processes of the solid phase (Santillana et al., 2012). Solute partitioning results in microsegregation, a phenomenon that Kou (2002) describes as microscopic-scale segregation.

Microsegregation can be mathematically expressed by the solute redistribution

equation, which can be derived by considering four contour conditions: 1) local equilibrium exists at the solidification solid–liquid interface, and the effect of the curvature of the interface is neglected; 2) there is no exchange of material between the volume elements and their surroundings owing to convection or diffusion; 3) diffusion in the solid is negligible; and 4) the composition of liquid in the volume element is uniform (Kou, 2002).

The solute redistribution equation is given in Equation 4, known as the Scheil equation, where C_s is the local solute concentration, k is a constant that can be calculated using Equation 5, and f is the volume fraction of the solid. In Equation 5, C_{SM} corresponds to the maximum solubility of the solid phase, and C_E is the eutectic composition.

$$C_s = kC_o(1 - f_s)^{k-1} \quad \text{(Equation 4)}$$

$$k = \frac{C_{SM}}{C_E} \quad \text{(Equation 5)}$$

The solidification curve plotted using the Scheil equation can provide relevant information on the phases formed during cooling. Since the welding process involves the microsegregation of alloy elements, thermodynamic simulations of this curve are essential for understanding the weld metal solidification route.

2.2 Solidification behaviour of austenitic stainless steel welds

Austenitic stainless steels (ASSs) are Fe-Cr-Ni alloys. Chromium confers corrosion resistance by forming a superficial protective oxide layer. Nickel is responsible for stabilising the austenite phase at room temperature. Due to their excellent mechanical properties and corrosion resistance, these materials are widely used in manufacturing components or equipment that operate under critical conditions, such as high temperatures and mild or severe corrosive environments. ASSs are typically applied in chemical, steam power, nuclear, and other energy industries. The most commonly employed austenitic stainless steels in the oil and gas industry are AISI 300 steels, which contain 16-26 wt.% Cr and 6-22 wt.% Ni (Brooks, Thompson, 1991; Plaut et al., 2007; Arata, Matsuda, Saruwatari, 1974).

A homogeneous wrought austenitic stainless steel generally solidifies with a fully austenitic microstructure, as shown in Figure 6a. The matrix phase, austenite, is a solid solution with low stacking fault energy and a high work hardening capability. Many applications require these materials to undergo welding processes. A consequence of welding is the alteration of the solidification mode depending on the chemical composition of the weld metal. Even at room temperature, it is possible to verify the presence of some retained ferrite. Due to the

solidification behaviour and subsequent solid-state phase transformations, the as-welded microstructure of austenitic stainless steel may consist of a duplex austenite-ferrite structure, as exemplified in Figure 6b (Brooks, Thompson, 1991; Plaut et al., 2007).

Figure 6 — SEM images of (a) austenitic stainless steel Super 304H and (b) duplex austenite-ferrite microstructure of the fusion zone of an AISI 304H (base metal) and AWS E347-17 (filler metal) weld

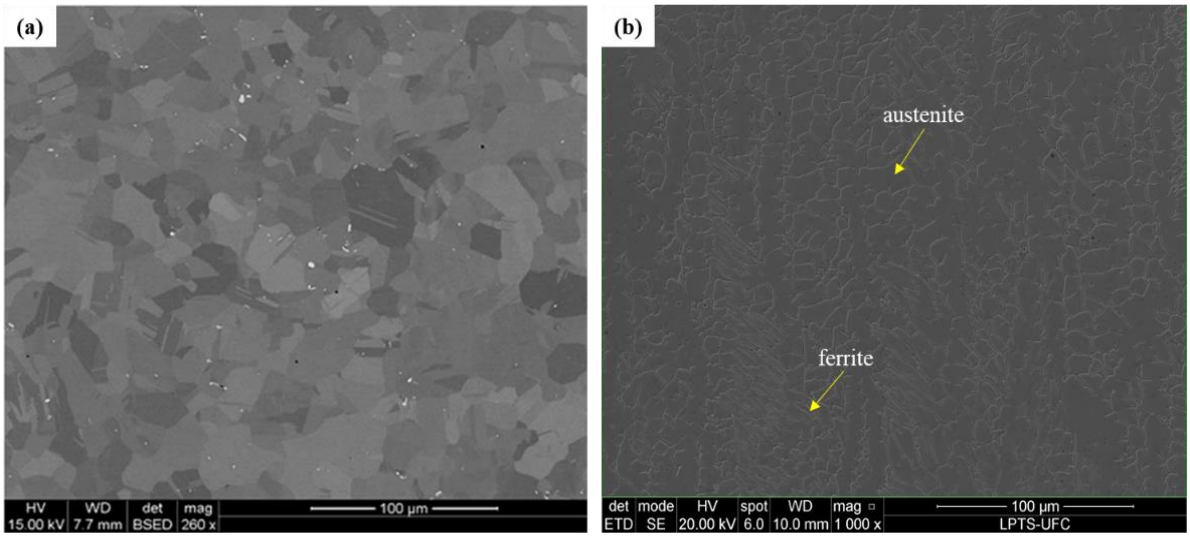

Source: (a) Zieliński, Wersta, and Sroka (2022); (b) elaborated by the author.

The solid-state phase transformations and the solidification behaviour are controlled by the chemical composition and by the welding cooling rate; both factors are related to the susceptibility of the solidification cracks and the solidification process itself (Takalo, Suutala, Moisio, 1979; Brooks, Thompson, 1991). Moreover, the welding process and filler metal composition remarkably influence the susceptibility of austenitic stainless steel weld metals to solidification cracking (Lundin, Chou, Sullivan, 1980).

ASSs are materials considered to have good weldability and are not overly sensitive to variations in welding parameters. However, in alloys with no ferrite, solidification cracking often occurs as a result of weld processes, which originate in the fusion zone due to the accumulation of low-melting eutectic liquid films composed of impurities and alloying elements (Lundin, Chou, Sullivan, 1980; Arata, Matsuda, Saruwatari, 1974; Lundin, Delong, Sponds, 1975; Shankar et al., 2003).

It is well known that the solidification cracking susceptibility of austenitic stainless steels is minimised by the presence of a certain quantity of retained ferrite (Takalo, Suutala, Moisio, 1979; Brooks, Thompson, 1991; Shankar et al., 2003). Scherer (1941) affirmed that a crack-free weld is obtained from a weld metal containing 5-35% δ-ferrite. According to Brooks

and Thompson (1991), the precision of such predictions may be affected by variations in welding conditions. Lundin, DeLong, and Sponds (1975) established that distinct ASS alloys require different amounts of δ-ferrite to prevent cracking.

Kujanpää, David, and White (1986) elucidated the beneficial effect of δ-ferrite on ASS welds. They concluded that a total of 5-20% δ-ferrite can decrease the solidification cracking susceptibility once the solidification mode of the weld metal changes to no more primarily austenitic. To better understand this aspect, the following subsection of this thesis consists of a more detailed explanation of the stainless steel solidification modes.

2.2.1 Solidification modes

The ASSs solidify with a fully austenitic microstructure, and subsequent solid-state eutectic and peritectic reactions may occur, depending on the chemical composition. During the welding process, high cooling rates result in nonequilibrium solidification, which causes microsegregation of the alloy elements. The microchemical alteration of the liquid phase may modify the solidification behaviour of these materials, and the primary phase can be either austenite or ferrite (Vitek, Dasgupta, David, 1983; Katayama, Fujimoto, Matsunawa, 1985).

According to the microchemical composition of the liquid phase, stainless steel may solidify in four different solidification modes. These modes are fully austenitic (A), primary austenite/secondary ferrite (AF), primary ferrite/secondary austenite (FA), and fully ferritic (F). Figure 7 presents a quasibinary vertical section of the Fe-Cr-Ni ternary diagram of stainless steel containing 70 wt.% Fe, separating the range of composition occurrence of the solidification modes according to the red dashed lines (Shankar et al., 2003; Brooks, Thompson, 1991).

The major alloying elements Cr (ferritizing) and Ni (austenitising) strongly influence the solidification mode. The nickel-rich side of the quasibinary diagram in Figure 6, i.e., the left side of the eutectic point, shows the A mode, containing up to 17 wt.% Cr and between 14 and 25 wt.% Ni. In this mode, almost all of the liquid phase becomes austenite during solidification, and austenite stabilisation entails the accumulation of chromium and other ferritising elements at the grain boundaries. Furthermore, the solubility of impurities in austenite is very low, which may cause intense segregation of P and S. Consequently, some residual eutectic or peritectic liquids with low melting points may quickly form at the solidification boundaries. Hence, a fully austenitic solidification mode is critical for the occurrence of solidification cracking (Koseki et al., 1994; Brooks, Thompson, 1991).

Figure 7 — Quasibinary vertical section of the Fe-Cr-Ni ternary diagram at 70 wt.% Fe showing the solidification modes

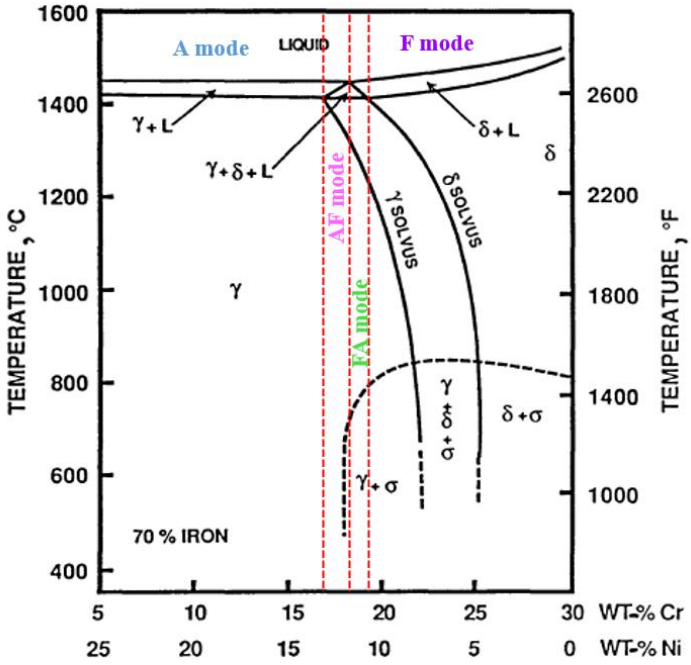

Source: Pugh and Nisbet (1950) apud Brooks and Thompson (1991), adapted.

Compared to the A mode, the AF mode is observed for alloy compositions with more Cr and less Ni. In this situation, the austenite phase nucleates and grows during solidification, and larger amounts of chromium and other ferritizing elements segregate to the grain boundaries. If the residual liquid is sufficiently enriched with ferritizing elements, some ferrite may be formed by a eutectic reaction ($L \rightarrow \gamma + \delta$-ferrite). In addition, as the temperature decreases, part of this δ-ferrite may revert into austenite by a solid-state transformation. The AF mode is also not favourable for preventing solidification cracking, as it may be easy for some residual liquid to accumulate and coalesce during the last stages of solidification (Koseki et al., 1994; Shankar et al., 2003; Brooks, Thompson, 1991).

The FA mode is shown in Figure 7 at the chromium-rich side of the quasibinary diagram, in the middle to the right limit of the eutectic triangle. During solidification, ferrite is the primary phase, and its stabilisation implies the segregation of nickel and other austenitizing elements to interdendritic volumes, where the austenite phase nuclei by a peritectic reaction. After the end of solidification, the ferrite may be partly subjected to solid-state transformation, resulting in the formation of another austenite phase, which is very similar to the austenite formed during the solidification process (Suutala, Takalo, Moisio, 1980; SHANKAR Et al., 2003; Brooks, Thompson, 1991). Shankar et al. (2003) emphasised that austenitic stainless steel weld metals retain a high percentage of δ-ferrite because of both the segregation patterns of Cr

and Ni after solidification and the rapid cooling rates during welding, which prevent diffusion of these major alloy elements.

The FA mode is known to succeed in providing crack-free welds. As previously mentioned, the presence of certain amounts of δ-ferrite is beneficial. Several authors have proposed that one of the main reasons for this difference is that impurities are more soluble in ferrite than in austenite, resulting in less segregation (Arata, Matsuda, Saruwatari, 1974; Brooks, Thompson, 1991; Lundin, Chou, Sullivan, 1980). However, this factor may not explain the overall influence of δ-ferrite. Other aspects are discussed in the following subsection of this thesis.

Finally, the F mode is verified for high-Cr and low-Ni composites. During solidification, all the liquid transforms into ferrite, and in the solid state, austenite proceeds to nucleate at ferritic boundaries, which are regions enriched in Ni and other austenitising elements (Shankar et al., 2003; Brooks, Thompson, 1991). A fully ferritic microstructure may not be advisable when considering cracking susceptibility during solidification.

There are different morphologies associated with each solidification mode. Figure 8 and Figure 9 show the possible morphologies of the austenitic stainless steel welds.

Figure 8 — Representation of the morphologies of austenitic stainless steel welds

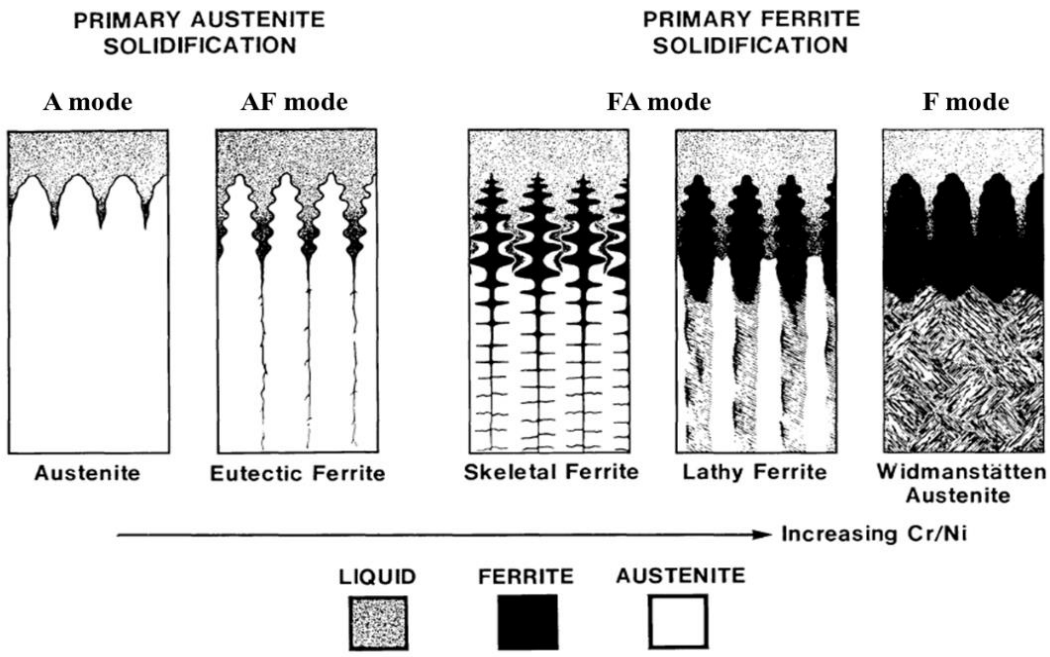

Source: Brooks and Thompson (1991), adapted.

Figure 9 — Three-dimensional views of typical austenitic stainless steel weld morphologies

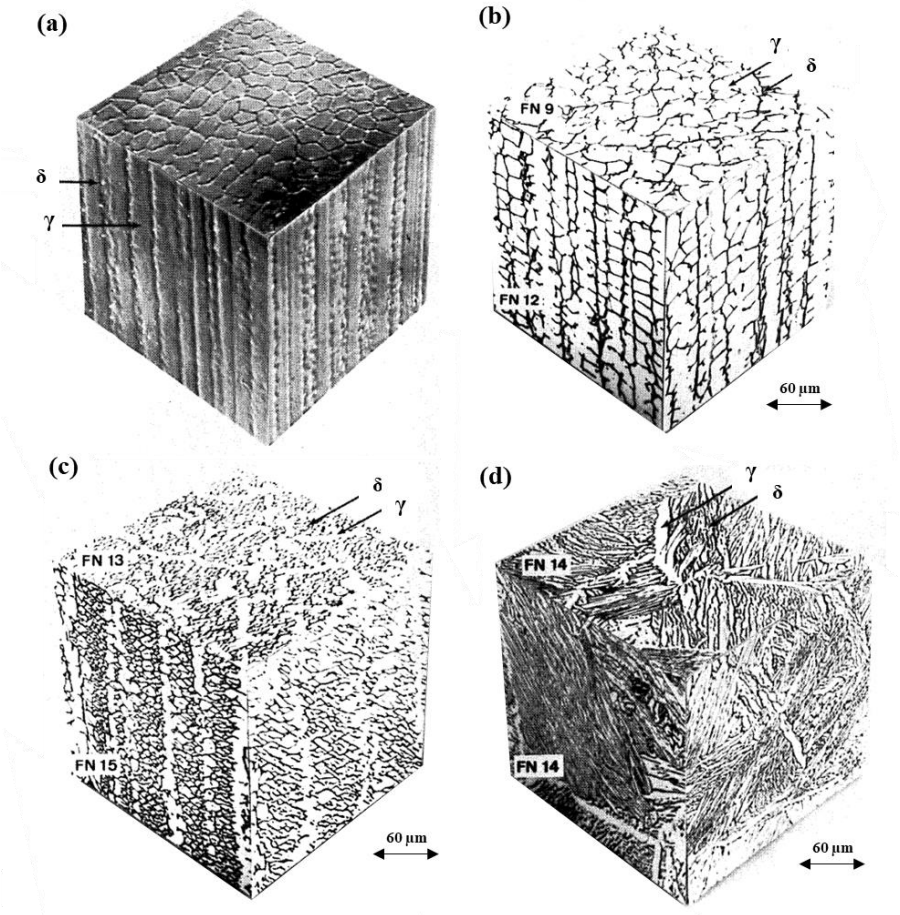

Note: Vertical welding direction. (a) Cellular primary austenite structure with intercellular ferrite in AISI 310; (b) skeletal ferrite in AISI 308; (c) lathy austenite in AISI 308 resulting from a multipass weld; (d) acicular ferrite in the upper portion of the AISI 308 multipass weld.

Source: David (1981) apud Brooks and Thompson (1991), adapted.

Cellular structures are characteristic of primary austenite solidification modes and may present some retained ferrite as isolated globules or strings in intercellular regions, as evidenced in Figure 9a. This type of retained ferrite is referred to as globular and results from the instability of other ferrite morphologies (David, 1981).

Alloy compositions solidified in the primary ferrite mode may develop the following morphologies: skeletal/vermicular ferrite (Figure 9b), lathy/lacy ferrite (Figure 9c), acicular ferrite (Figure 9d), and Widmanstätten austenite (Figure 8). Their formation mechanisms are related to the solidification process and solid-state transformations. Additionally, depending on the welding process conditions, globular ferrite may form if there is some local thermal instability, as indicated in Figure 9a (David, 1981).

Figure 9b presents skeletal or vermicular ferrite, which consists of a skeletal and

aligned network. Ferrite is localised on the core of the dendrites and is surrounded by austenite. This morphology is verified for δ-ferrite contents of 5 to 15 FN (David, 1981; Brooks, Thompson, 1991). The following subsection contains an adequate definition of the FN.

Verified for FNs in the range of 13-15, lathy or lacy ferrite is characterised by an interlaced ferrite network oriented along an austenitic matrix, in which the ferrite network has relatively regular spacing, as shown in Figure 9c. This morphology results from ferrite dissolution during cooling and more intense diffusion-controlled solid-state transformations due to the chemical composition (David, 1981; Brooks, Thompson, 1991).

In fully ferritic solidification (F mode), all the austenite nuclei grow from the parent ferrite by a solid-state transformation involving extensive diffusion (David, 1981; Brooks, Thompson, 1991). This process may result in two morphologies, Widmanstätten austenite (Figure 8) and acicular austenite (Figure 9d), both of which have a needle or plate aspect due to shear tension during growth.

Given that the welding process involves intense segregation of alloy elements and may produce regions with different microchemical, the structure of duplex (austenitic-ferritic) ASS welds is commonly a combination of the morphologies previously discussed. An example of this is presented in Figure 10, where the darker regions are the ferrite phase and the lighter regions are the austenite phase.

Figure 10 — Cross-sectional microstructure of the fusion zone of a weld between AISI 304H (base metal) and AWS E347-17 (filler metal)

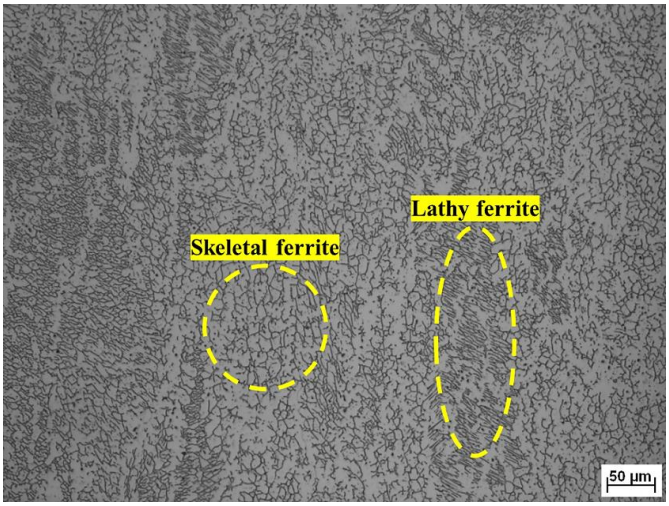

Source: elaborated by the author.

The amounts of other alloying elements also affect the solidification mode determination once they each contribute to stabilising austenite or ferrite. This significant influence was considered in the empirical elaboration of mathematical expressions that enable

the calculation of composition-related variables denominated chromium equivalent and nickel equivalent, which were used for developing diagrams for phase prediction. The chromium equivalent (Cr_{eq}) takes into account the amount of ferritising elements. Likewise, the nickel equivalent (Ni_{eq}) considers the amount of austenitizing elements (Schaeffler, 1949; Delong, 1974; David, 1981).

The Schaeffler diagram, presented in Figure 11, was published in 1949 and then used for the prediction of the ferrite content of austenitic stainless steel weld metals.

Figure 11 — Schaeffler diagram

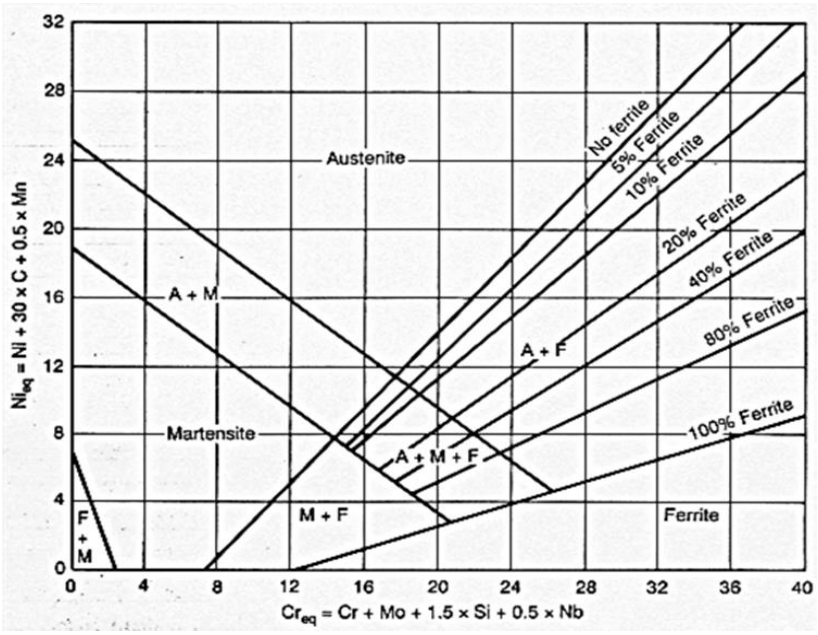

Source: ASM International (1997).

The Schaeffler expressions for Cr_{eq} and Ni_{eq} are shown in Equations 6 and 7, where the concentrations are expressed in weight percentages. Equations 6 and 7 were deemed inaccurate for the following reasons: the strong austenitizing effect of nitrogen is not considered in Ni_{eq}, manganese does not promote austenite formation at high temperatures, and its predictions are in terms of the percentage of ferrite, which is imprecise (KOTECKI, SIEWERT, 1992).

$$Cr_{eq} = \%Cr + \%Mo + 1.5(\%Si) + 0.5(\%Nb) \quad \text{(Equation 6)}$$

$$Ni_{eq} = \%Ni + 30(\%C) + 0.5(\%Mn) \quad \text{(Equation 7)}$$

Some diagrams were developed to improve the Schaeffler predictions, such as the DeLong diagram (1974), the WRC-1988 diagram, and the WRC-1992 diagram, as shown in Figure 12.

Figure 12 — WRC-1992 diagram

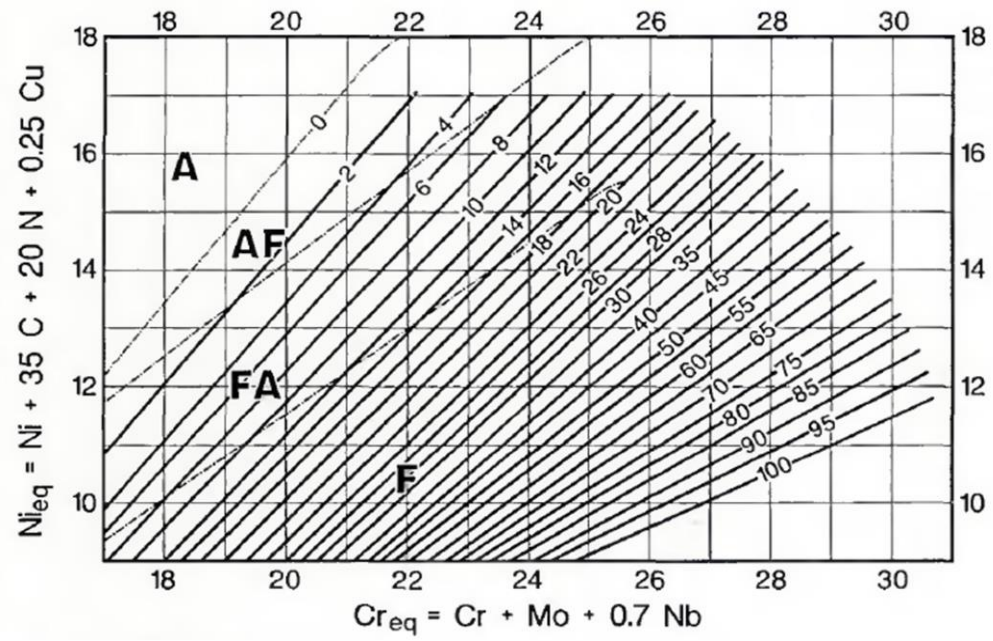

Source: Kotecki and Siewert (1992).

The WRC-1992 diagram was elaborated by Kotecki and Siewert (1992), and its expressions for Cr_{eq} and Ni_{eq} are shown in Equations 8 and 9, respectively.

$$Cr_{eq} = \%Cr + \%Mo + 0.7(\%Nb) \quad \text{(Equation 8)}$$

$$Ni_{eq} = \%Ni + 35(\%C) + 20(\%N) + 0.25(\%Cu) \quad \text{(Equation 9)}$$

Kujanpää et al. (1979) studied the correlation between solidification cracking and microstructure in austenitic stainless steel welds. A relationship was documented between the ratio of chromium and nickel equivalent to the solidification modes. Table 1 presents this information, which is part of the methodology of solidification mode prediction applied in this thesis. Notably, Kujanpää et al. (1979) considered the Schaeffler expressions for the Cr_{eq} and Ni_{eq} calculations.

Table 1 — Relationship between the Cr_{eq}/Ni_{eq} ratios and the stainless steel weld solidification mode

Solidification mode	**A**	**AF**	**FA**	**F**
Cr_{eq}/Ni_{eq}	< 1.25	1.25 – 1.48	1.48 – 1.95	> 1.95

Source: elaborated by the author based on Kujanpää et al. (1979).

2.2.1.1 Influence of ferrite

Ferrite may prevent solidification cracks from occurring in austenitic stainless steel welds. Arata and Matsuda (1974) and many other authors have demonstrated that microstructures with ferrite are less susceptible to solidification cracking than those without ferrite. However, it is essential to mention that the cracking susceptibility increases for high amounts of ferrite, according to Hull (1967).

In addition to the higher solubility of impurities, Brooks and Thompson (1991) discussed more reasons for the favourable effect of ferrite on ASS welds. Considering their conclusions, two other rationales are very plausible. The first is the ferrite/austenite boundaries, which are not wetted by liquid films as the ferrite/ferrite and austenite/austenite boundaries are; thus, forming fissures during the last stages of solidification is more difficult. The second is related to the fact that the ferrite/austenite boundaries constitute irregular paths for crack propagation. In contrast, austenite/austenite and ferrite/ferrite boundaries are smoother paths that facilitate crack growth. Figure 13 shows schematics of intersecting grains occurring during solidification, where the grain boundaries are potential crack paths.

Figure 13 — Schematics of solidification

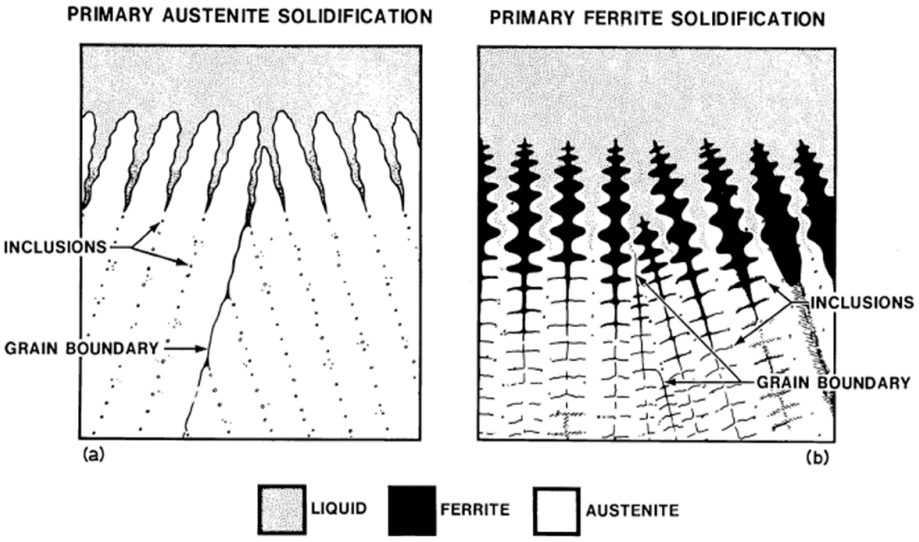

Source: Brooks and Thompson (1991).

As shown in Figure 13, in primary austenite solidification, low-melting point liquids may be confined in intercellular regions, and the lack of angled boundaries enables them to coalesce and form cracks that propagate through the filled liquid phase. However, during primary ferrite solidification, the ferrite retained in austenite grain boundaries forms a

nonuniform path, which prevents the propagation of cracks and acts as a trap for inclusions (Brooks, Thompson, 1991).

Even considering its benefits, the presence of ferrite in some applications is favourable only for small amounts since ferrite 1) decreases the material's toughness at very low temperatures, 2) has high magnetic permeability, 3) may be preferentially degraded in some corrosive environments, and 4) may transform to embrittling phases, such as sigma and chi phases, during high-temperature exposure in-service or post weld heat treatments (Hull, 1967; Lundin, Chou, Sullivan, 1980).

In light of the previous discussion, the importance of knowing the ferrite content of austenitic stainless steel welds is understandable. The ferrite content of a weld is often determined via optical microscopy image analysis, which measures the ferrite fraction area of a sample extracted from a weld through metallographic preparation. Additionally, the Welding Research Council (WRC) Subcommittee on Welding Stainless Steels standardised a non-destructive method of ferrite content determination based on weld magnetic attraction, establishing the ferrite number (FN), a variable with a value defined by a calibrated system (Kotecki, 1997).

Currently, ISO 8249 (2018) defines the FN procedure as “the measurement of the attractive force between a weld metal sample and a standard permanent magnet”. This standard describes all necessary procedures, methods, and apparatuses. It is essential to emphasise that the ferrite number does not correspond precisely to the ferrite percentage. However, they can be related; the higher the FN measured is, the greater the ferrite percentage (Kotecki, 1997).

2.3 Cracking

Crack formation occurs when a material is subjected to stresses that exceed its strength, i.e., when the material cannot absorb the stresses through deformation (Marques, Modenesi, Bracarense, 2017). Generally, cracks are classified according to their formation temperature as hot or cold cracks (Wu, Tsai, 1999). The cracks generated during welding are hot cracks, such as solidification cracks (Brooks, Thompson, 1991; Coniglio, Cross, 2013; Fink et al., 2020).

2.3.1 Hot cracking

cracks develop at high temperatures due to 1) the formation of imperfections in the mushy zone along grain boundaries during solidification or 2) reheating at temperatures below the nominal melting temperature of the alloy (Wu, Tsai, 1999). The types of hot cracks can be

divided based on their location and formation, and several classifications have been suggested in the literature. The works of Hemsworth, Boniszewski, and Eaton (1969) and Kannengiesser and Boellinghaus (2014) are noteworthy.

Hemsworth, Boniszewski, and Eaton (1969) proposed the classification of hot cracks into type 1 and type 2. Type 1 corresponds to solidification cracks and liquation cracks, which nucleate through liquid film accumulation at grain boundaries during the last stages of solidification. Type 2 cracks are called ductility-dip cracks and can be defined as cracks that nucleate in the solid-state at temperatures below the material's effective *solidus* temperature.

2.3.1.1 Solidification cracking

In the last stages of solidification, low melting point elements with partition coefficients lower than 1 segregate to the liquid between the solidified dendrites or cells, forming liquid pockets or films. These elements segregate during the entire solidification process. However, at the last stages, they are isolated from the liquid feed by the coalescence of dendrite arms. These liquid films are nucleation sites for cracks (Santillana et al., 2012; Safari, Forouzan, Shamanian, 2012).

The solidification cracking is caused by the low melting point liquid phases in the mushy zone, which allow the separation of cells or grain boundaries under the action of tensile stresses, thermal contractions, and solidification shrinkage during the weld metal cooling process. The nucleation and propagation of solidification cracks occur at temperatures close to the *solidus* temperature, commonly at the end of weld metal solidification (Modenesi, Marques, Santos, 2012).

As previously mentioned, solidification cracks form in the fusion zone along solidification grain boundaries and solidification subgrain boundaries, as shown in Figure 14, which illustrates the interfaces that may be present in a single-phase weld metal as solidification proceeds (Applett, Pellini, 1954; Brooks, Thompson, 1991; Cross, 2005; Sutton, 2013).

Figure 14 — Schematic representation of the interfaces that may exist in a single-phase weld metal following solidification

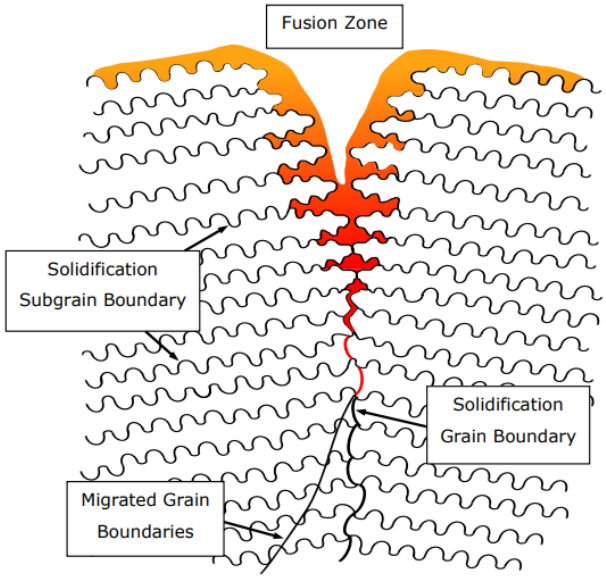

Source: Lippold, Clark, and Tumuluru (1992).

To illustrate the solidification crack morphology, Figure 15 shows a top-view image of a weld bead containing solidification cracks obtained from the Trans-Varestraint weldability test carried out by Kromm et al. (2022).

Figure 15 — Top view of solidification cracks and their lengths in the weld metal of a specimen after Trans-Varestraint test

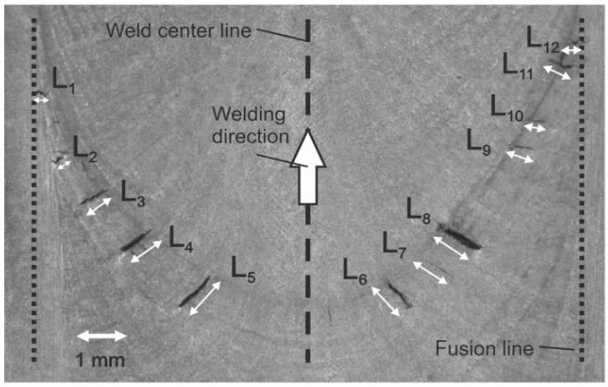

Source: Kromm et al. (2022).

A better understanding of solidification crack formation requires knowledge of the solidification stages. Based on prior works, Santillana et al. (2012) described the three stages of cast steel solidification. The explanations can represent the welding process once casting also involves nonequilibrium cooling.

In stage 1, the formation of dendrites occurs during solidification and mass feeding.

When the temperature decreases, secondary dendrite arms form. At this stage, the semisolid material has no mechanical resistance, as the dendrites are separated by liquid. Hence, if thermal or mechanical strain is applied, the resulting opening in the structure can be filled by intergranular or interdendritic liquid, a phenomenon called backfilling (Santillana et al., 2012).

Stage 2 is characterised by the coarsening and collision of dendrites during solidification and is divided into two substages: stage 2a and stage 2b. In stage 2a, the secondary dendrite arms reach and interlock, strengthening the solidified material. Even so, the liquid feeding in the network is still sufficient to prevent the formation of cracks. Stage 2a encompasses solid fractions (f_s) between 0.65 and 0.80, and the range of temperatures that corresponds to those solid fractions is known as the zero strength temperature (ZST), which is defined as the temperature at stresses that can be transmitted perpendicular to the solidification direction during cooling (Santillana et al., 2012).

Stage 2b is characterised by coarsening of the dendrite arms and interdendritic separation. When cooling advances, secondary dendrite branches become indistinct as the structure becomes similar to that of columns without visible dendrite branches. The last liquid fraction present is noncontinuously trapped between interlocking dendrites. As a result, the strength of the material is low. Therefore, any stress applied to the material may easily result in hot cracking (Santillana et al., 2012).

At stage 3, the transition from the dendritic to the grain structure occurs. Thin liquid films containing segregated elements that lower their melting points may still be present at grain boundaries. In this stage, solid-state creep is the only mechanism for the material to adapt to solidification shrinkage and thermal stresses (Santillana et al., 2012).

The increase in the plasticity of the material marks the end of solidification. The temperature at which the material becomes ductile is named the zero ductility temperature (ZDT). The brittle to ductile transition is commonly associated with solid fractions of 0.98-1.0 (Santillana et al., 2012).

Figure 16 shows a solidification structure showing the stages of solidification and the temperatures used. Here, it is also possible to observe other essential definitions that were previously mentioned. The yellow range indicates that the moments of solidification at the secondary dendrite arms increase, become coarser, and interlock, i.e., coherence between secondary dendrite arms is achieved, which is related to $0.80 \leq f_s \leq 0.90$. The green range ($0.90 \leq f_s \leq 0.98$) is equivalent to the solidification instants at which the structure changes from dendrites to grains. The mushy zone is a region where liquids and dendrites coexist at temperatures lower than the coherency temperature, which corresponds to a f_s of 0.8 (Santillana

et al., 2012).

Figure 16 — Solidification structure with characteristic temperatures and solid fractions

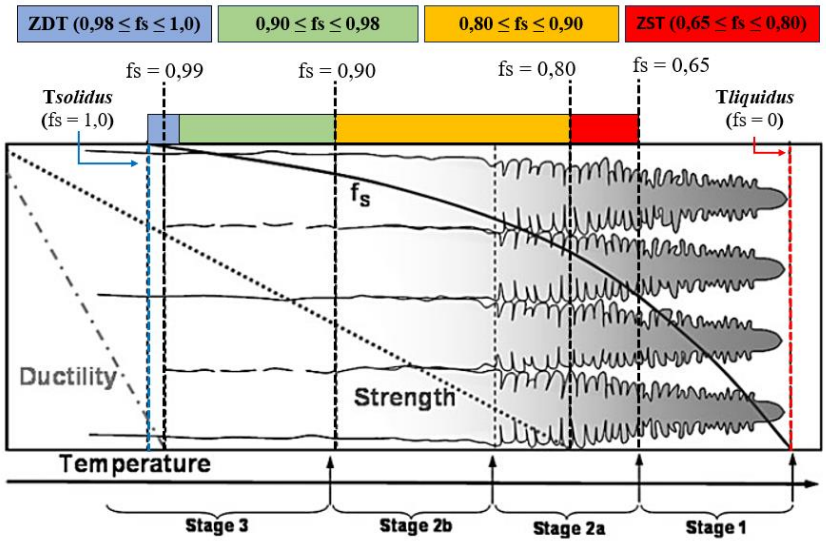

Source: Santillana et al. (2012), adapted.

The hot cracking susceptibility of a material can be qualitatively related to the range between ZST and ZDT, as shown in Equation 10. This range is defined as the brittle range temperature (BTR) and express a solidification zone in which the microsegregation and the stresses are most critical. In temperatures higher than the ZST, there is a liquid abundancy, then the accommodation of stresses is easy. When the temperature is below ZDT, the material, now completely solidified, is capable to distribute and to resist the stresses. However, in the BTR (e.g., for temperatures between ZST and ZDT), the residual liquid does not solidify for a certain period, as its melting point is low. At the same time, the solid phase, not completely formed yet, is subjected to high stresses, that are concentrate in the interlocks of dendrite secondary arms, enabling its fracture.

Comparing two alloys, for example, the one with a higher BTR remains for longer period in the critical stages of solidification and is subjected to greater thermal stresses due to contraction resulting from constraints, thus having a greater tendency to crack (Santillana et al., 2012; Aucott et al., 2018). However, some other factors must be considering when assessing the solidification cracking susceptibility of a material, as the microstructures characteristics.

$$BTR = ZST - ZDT \quad \text{(Equation 10)}$$

From the perspective of the welding process, it is necessary to consider some characteristics that influence solidification cracking. As mentioned above, the concentrated

moving heat implies a temperature gradient from the centre to the extremities of the weld metal, and the rapid cooling rate causes nonequilibrium solidification. Then, the weld metal microstructure may be planar, cellular, or dendritic, depending on the solidification conditions and the chemical composition of the alloy (Safari, Forouzan, Shamanian, 2012; Kou, 2002). Both of these factors strongly affect the origination of cracks in welds. Moreover, welding involves thermal contraction and solidification shrinkage, which may result in high stress levels in the weld metal (Safari, Forouzan, Shamanian, 2012).

Weld solidification cracking nucleation and propagation involve complex interactions between metallurgical and mechanical factors. Figure 17 shows the relationships between the weld process parameters that affect solidification cracking, such as the number of thermal cycles, and the restraint intensity. The thermal-metallurgical interactions control the solidification microstructure. In turn, thermal-mechanical interactions control local and global stresses and strains (Cross, 2005).

Figure 17 — Parameters that affects the solidification cracking in a weld

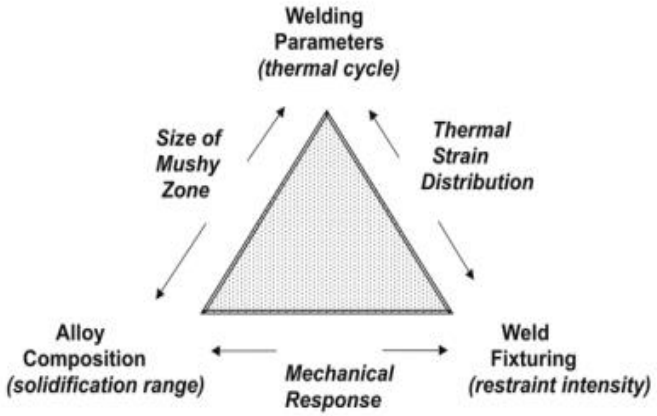

Source: Cross (2005).

Aucott et al. (2018) proposed a three-stage mechanism model for solidification cracking during steel welding. Figure 18 shows a schematic of solidification cracking, and its explanations of crack nucleation and propagation clarify the concepts discussed above. During stage I, at the last instant of solidification, as the microstructure transforms from dendrites to grains, liquid pockets are isolated at grain boundaries, where hot cracks may initiate. Stage II corresponds to the intergranular coalescence of hot cracks with each other; some cracks may propagate through the grain boundaries to dendrites, and others may not coalesce and continue to be isolated. Finally, at stage III, the crack propagates along the boundaries between

solidifying columnar dendrites with a higher liquid fraction.

Figure 18 — 2D schematic illustration of solidification cracking mechanisms

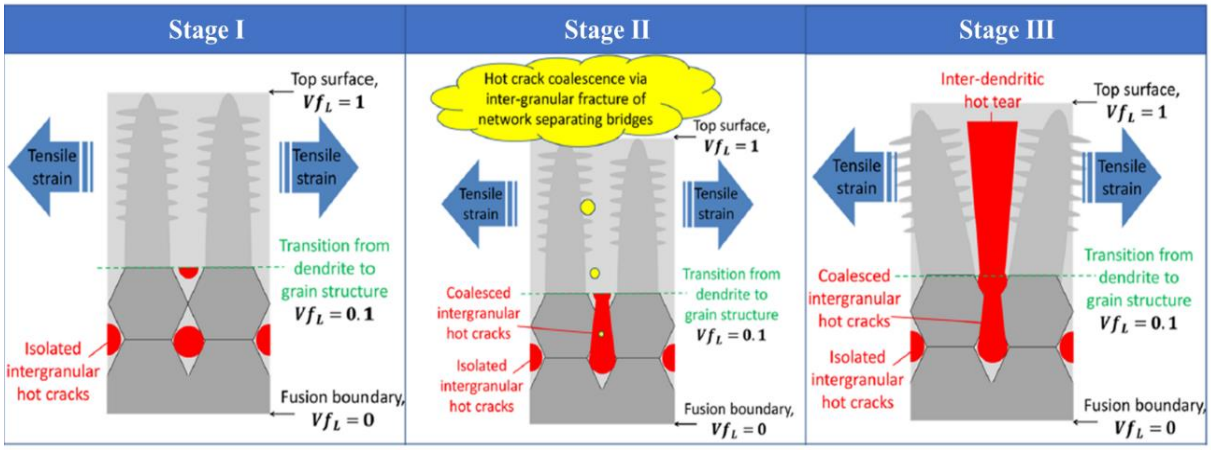

Source: Aucott et al. (2018), adapted.

A material's susceptibility to solidification cracking can be experimentally determined using weldability tests. A subsection of this literature review is dedicated to better explaining the methodology of some of these tests.

Numerous factors are known to influence the nucleation and propagation of solidification cracks. There are thermomechanical aspects, such as thermal contraction and solidification shrinkage; the extent of restraint and ductility of the weld metal in the mushy zone; and metallurgical aspects, such as solute content at the end of solidification, impurity quantity, and grain shape (Cross, 2005; Safari, Forouzan, Shamanian, 2012; Coniglio, Cross, 2013).

Predicting the occurrence of solidification cracking helps to prevent failures. Thus, many theories, models, or criteria have been proposed to describe the conditions for solidification crack initiation, considering the thermal, metallurgical, or mechanical effects or even combinations of these aspects (Safari, Forouzan, Shamanian, 2012; Coniglio, Cross, 2013; Kromm et al., 2022).

In chronological order, several examples of theories are the shrinkage-brittleness theory (Bochvar, Sviderskaya, 1947; Pumphrey, Jennings, 1948), the Strain Theory (Pellini, 1952), the Generalised Theory (Borland, 1960), the Technological Strength Theory (Prokhorov, 1962), the Modified Generalised Theory (Matsuda, Nakagawa, Sorada, 1982), and the Rappaz-Drezet-Gremaud Theory (Rappaz, Drezet, Gremaud, 1999). These theories, as well as several others, are complex and require various parameters. The ability of these methods to predict solidification cracks depends directly on the available material data.

2.3.1.2 Liquation cracking

During welding, the temperatures reached in the weld pool are usually higher than the *liquidus* temperature of the material. The melted metal constitutes the fusion zone, and a part of the heat of this zone is transmitted to adjacent regions, creating other areas that suffer metallurgical alterations. Figure 19 presents an illustration of the existing regions in a heterogeneous weld, which are the fusion zone, unmixed zone, partially melted zone, and heat-affected zone (Baeslack, Lippold, Savage, 1979; Kou, 2003).

Figure 19 — Heterogeneous regions of a fusion weld

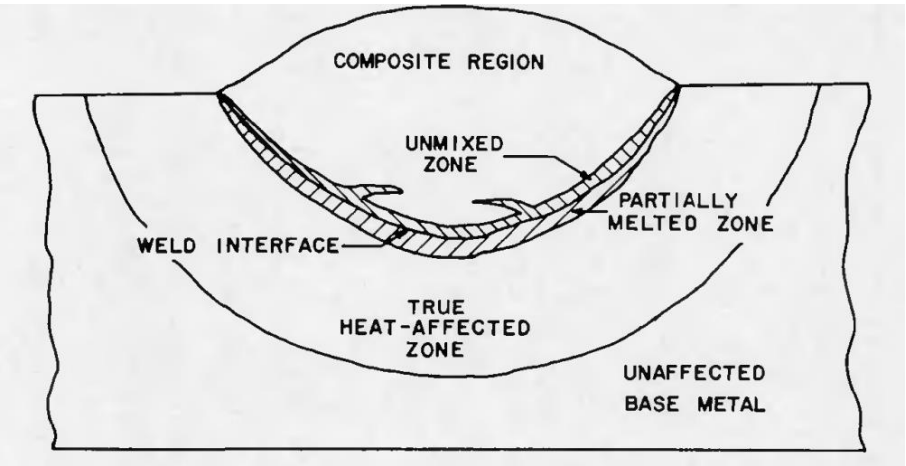

Source: Savage, Nippes, and Szekeres (1976).

The partially melted zone (PMZ) is characterised by temperatures above the eutectic temperature. Liquid in this region causes liquation, which may result in cracking, depending on many factors, such as the liquation extent, grain structure, hot ductility, and degree of solidification restraint (Kou, 2003).

As shown in Figure 20, as the liquid succeeds in wetting grain boundaries, thin liquid films can form, and when, during solidification, the material is subjected to tensile tension originating from solidification shrinkage or external sources, the material can develop liquation cracks (Kou, 2002; Modenesi, Marques, Santos, 2012).

Liquation cracks generally propagate intergranularly. They are common in austenitic stainless steel welds and are often related to inclusions, carbides, carbonitrides, and intermetallic phases, which may melt during welding and form liquid films (Modenesi, Marques, Santos, 2012).

Figure 20 — Mechanism of liquation cracking in the partially melted zone of a full-penetration aluminium weld

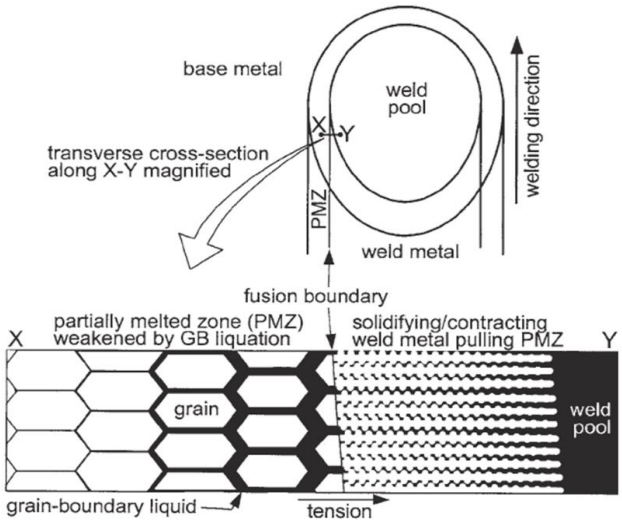

Source: Kou (2003).

Kou (2003) affirms that adequate welding conditions and the choice of materials can reduce liquation crack susceptibility. It is beneficial, for example, to have a filler metal with a *solidus* temperature higher than the base metal *solidus* temperature, a refined grain structure to minimise liquation, and lower welding energy, which provides less heat to be transmitted by the FZ. Figure 21 presents a solidification crack and a liquation crack in the aluminium circular-patch welds for comparison. Solidification cracks develop in the FZ and liquation cracks form in the PMZ.

Figure 21 — Macrographs showing cracking in aluminium circular-patch welds: (a) solidification cracking and (b) liquation cracking

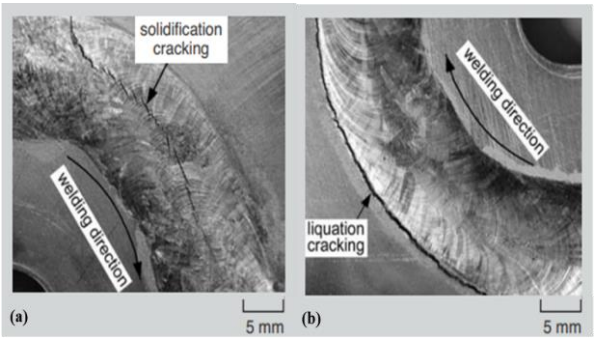

Source: Kou (2003), adapted.

2.3.1.3 Ductility-dip cracking

Austenitic stainless steel weld metals with large grain sizes and high restraint commonly develop ductility-dip cracks. Ductility-dip cracking (DDC) is an intergranular solid-

state cracking phenomenon in which cracks form below the effective *solidus* temperature due to grain boundary sliding (Li et al., 2019; Luther et al., 2022). Figure 22 shows a graphic of ductility *versus* temperature. Materials susceptible to this cracking present a loss of ductility in the range of 0 to $0{,}8T_M$, where T_M is the melting temperature of the material; in this range, face-centred cubic (FCC) alloys experience a ductility loss (Collins, Lippold, 2003; Jang et al., 2011). Luther et al. (2022) reported that $0{,}8T_M$ recrystallisation inhibits the formation of ductility-dip cracks and restricts their propagation.

Figure 22 shows evidence of the BTR and ductility-dip temperature range (DTR). By analysing the ductility curve, it can be concluded that DDC occurs when the material is subjected to external strain or stress that intercepts the DTR. These effects may be intrinsic to manufacturing or welding processes once they can imply void formation and grain boundary sliding (Collins, Lippold, 2003; Luther et al., 2022).

Figure 22 — Schematic diagram of the ductility curve at elevated temperature

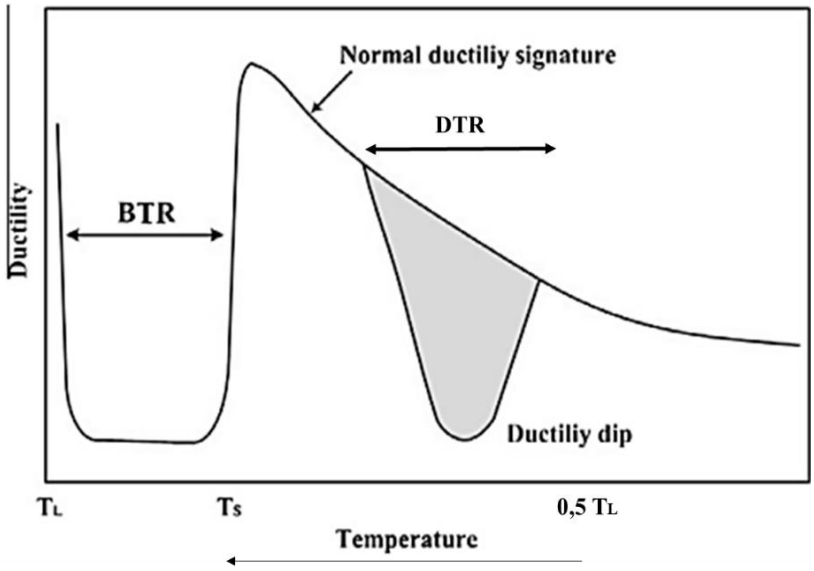

Source: Jang et al. (2011), adapted.

Once grain boundary sliding occurs, another characteristic of materials susceptible to DDC is the separation of grain boundaries (Collins, Lippold, 2003). DCC propagates along migrated grain boundaries (MGB), as presented in Figure 23 (Jang et al., 2011).

Figure 23 — Ductility-dip cracks along migrated grain boundaries in the fully austenitic weld metal

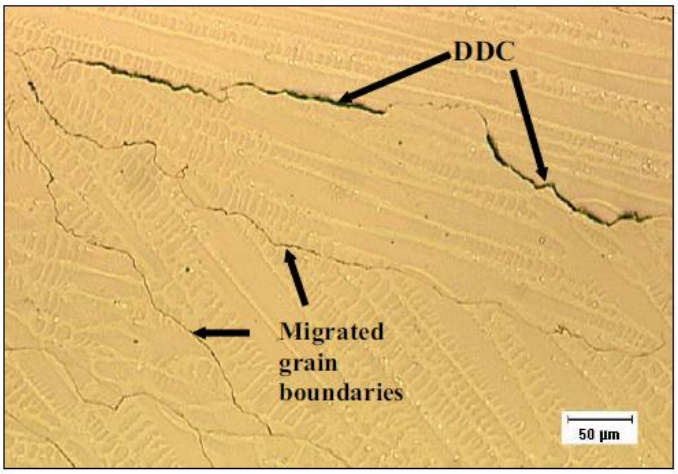

Source: Lippold (2005).

The factors known to contribute to DCC listed by Collins and Lippold (2003) are the impurity and interstitial element contents; solute, impurity and interstitial element segregation; grain growth; grain boundary sliding; grain boundary precipitation; grain boundary orientation relative to the applied strain; and multipass welding operations.

2.4 Weldability

The weldability of a material refers to its ability to be welded. More specifically, the weldability definition covers various characteristics of a material subjected to welding, such as physical properties, mechanical properties, and mainly the susceptibility to metallurgical degradation, which is usually determined by its susceptibility to cracking during welding or subsequent heat treatment (Lippold, 2005). Hence, for example, a material with good weldability is capable of 1) being adequately welded according to established conditions, 2) operating in service conditions following the requirements of its project, and 3) resisting crack formation during welding (Dupont, Lippold, Kiser, 2009).

DuPont, Lippold, and Kisser (2009) assert that the material's properties and welding process parameters influence the weldability. Thus, weldability is affected by resistance to crack propagation, fusion zone fluidity, fatigue, thermal expansion, oxidation resistance, and other factors.

2.4.1 Weldability tests

To evaluate the weldability of a material, several tests have been developed since

the 1930s (Goodwin, 1990; Lippold, 2005). Many classifications can categorise weldability tests. They can be grouped considering the methodology utilised to deform the weld pool as self-restraint or augmented restraint. The self-restraint weldability tests correspond to those where the deformation of the weld pool is promoted by forces resulting from the thermal effect of the heat source associated with thermomechanical reactions of the specimen, which is designed to crack (i.e., the deformation is promoted by solidification restraint).

In augmented restraint weldability tests, the weld pool deformation is provided by external loading through equipment. Thus, they are also referred to as externally loaded tests in the literature. This type of test is widely employed because it allows variations; the severity of the test can be controlled by applying different strain rates, which can affect crack formation and propagation (Campbell, Walsh, 1993).

For analysing hot cracks, the standard ISO TR 17641-3 (2005) states that the main augmented tests are the following: the Varestraint and Trans-Varestraint tests, the Programmable Deformation Rate, and the Hot Deformation Test. As the methodology of the present thesis consists of evaluating the solidification cracking susceptibility of corrosion-resistant weld metals using the Trans-Varestraint test, the following subsection provides more information on this test.

2.4.1.1 Trans-Varestraint test

The Trans-Varestraint weldability test is a variation of the Varestraint test, and both consist of submitting a specimen to flexural loading towards the end of the welding process to deform the weld pool and its adjacencies according to a predefined strain (Lippold, 2005; Statharas et al., 2019). The Varestraint test is employed to evaluate solidification cracks as well as liquation cracks, while the Trans-Varestraint test is applied to analyse solidification cracks (Lippold, 2005; Kannengiesser, Boellinghaus, 2014).

The Varestraint test was developed by Savage and Lundin (1965) and involves applying flexural loading parallel to the welding direction, as illustrated in Figure 24a. The load is imposed longitudinally among the weld bead, contributing to the formation of cracks in the fusion zone and the heat-affected zone (HAZ). In turn, in the Trans-Varestraint test (Figure 24b), which was created by researchers from Osaka University, flexural loading is carried out perpendicular to the direction of welding; the load is applied across the weld bead, which restricts crack formation to the fusion zone (Senda et al., 1971; Arata, Matsuda, 1976; Arata et al., 1977).

Figure 24 — Schematic representation of the flexural loading applied in the (a) Varestraint test and (b) Trans-Varestraint test

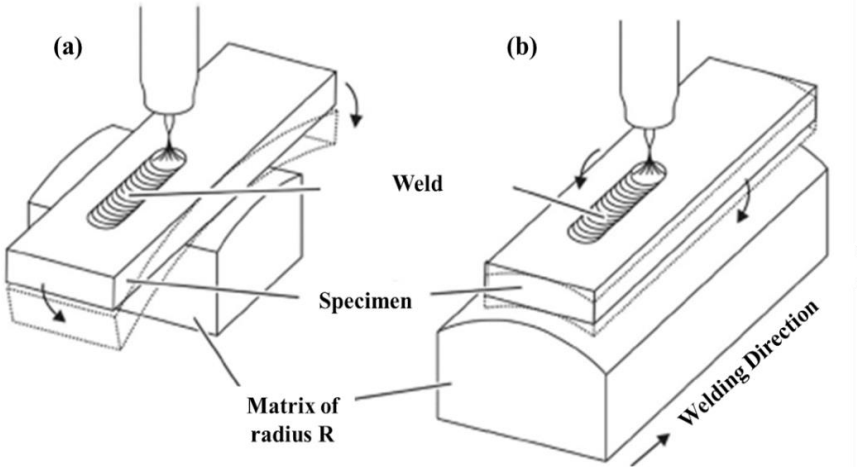

Source: Kromm et al. (2022), adapted.

As shown in Figure 24, the specimen deformation is guided by a matrix. The desired strain is then regulated by the matrix radius and specimen geometry, which is calculated by Equation 11, where ε is the percentage of strain to be applied, named the augmented strain, t is the specimen thickness, and R is the radius of the matrix (Senda et al., 1971).

$$\varepsilon = \frac{t}{2R} \, x \, 100 \qquad \text{(Equation 11)}$$

In addition to the strain, other variables of the Trans-Varestraint test can be adapted following the necessities or requirements of specific analysis, such as the welding process and the specimen bending speed. Commonly, the welding processes utilised in this test include gas tungsten arc welding (GTAW), autogenous welding or filler metal welding (Dupont, Lippold, Kiser, 2009).

2.4.1.1.1 Weldability evaluation using Trans-Varestraint test

The cracks formed at the specimen surface through the Trans-Varestraint test are usually measured under an optical microscope at a magnification of 25-50x. According to their position and length, three types of crack measurements are possible: the maximum crack length (MCL), which corresponds to the size of the longest crack; the total crack length (TCL), which is the sum of the lengths of all the cracks identified; and the maximum crack distance (MCD), which is equal to the maximum distance that a crack grew parallel to the welding direction. Figure 25 presents a schematic of cracks in a weld bead obtained by the Trans-Varestraint test and its respective MCL and MCD indications (Statharas et al., 2019).

Figure 25 — Maximum crack length (MCL) and maximum crack distance (MCD) for the Trans-Varestraint test

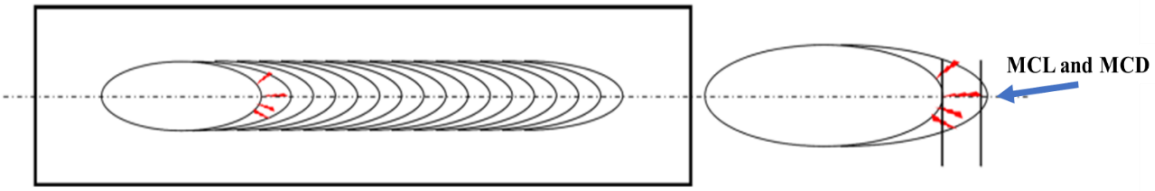

Source: Statharas et al. (2019), adapted.

The MCL, TCL, and MCD can be utilised for several analyses. The standard ISO TR 17641-3 (2005) sets out the procedure for evaluating and ranking materials regarding hot cracking susceptibility based on the TCL. The method demands plotting a graph of the TCL *versus* the augmented strain, as shown in Figure 26. Therefore, two important parameters can be determined according to the curve format. These are the critical strain (ε_{cr}), also known as the threshold strain, which is defined as the limit strain from which crack formation initiates, and the saturated strain (ε_{st}), the strain from which the total crack length does not increase considerably.

Figure 26 — Total crack length (TCL) in the fusion zone versus applied strain during transverse Varestraint testing

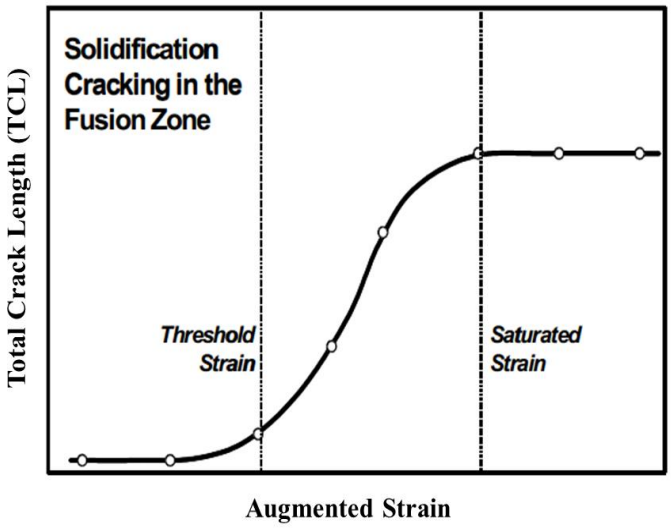

Source: Lippold (2005), adapted.

A second method to analyse Trans-Varestraint test results is to determine the solidification cracking temperature range (SCTR), which can be calculated through the expression presented in Equation 12, where MCD is the maximum crack length verified for the saturation strain condition and V is the welding velocity. Hence, SCTR corresponds to a

specific measurement of solidification crack susceptibility that enables comparisons between different materials (Lippold, Lin, 1996; Lippold, Kotecki, 2005; Statharas et al., 2019).

$$SCTR = cooling\ rate\ x\ \frac{MCD}{V} \quad \text{(Equation 12)}$$

Figure 27 represents a cooling curve evidencing the range of temperatures for solidification crack formation.

Figure 27 — Solidification Cracking Temperature Range (SCTR) calculation on a temperature versus time graph

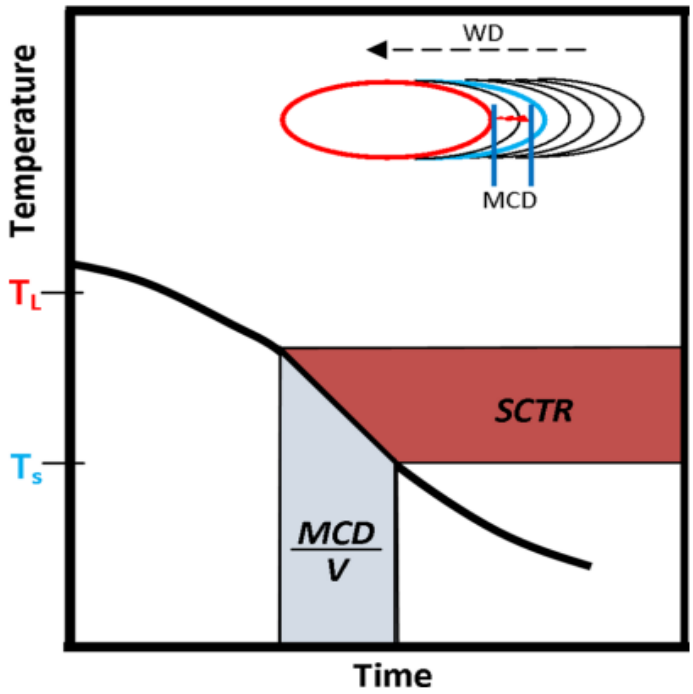

Source: Statharas et al. (2019).

The CSS is another criterion utilised here to evaluate the susceptibility of the weld metals to solidification cracking. It was determined using a graph with the crack growth curve (Figure 28). The time for cracking development (y axis) was calculated according to Equation 13, where L_{max} is the maximum crack length and V is the welding speed. After plotting the crack growth curve, the CSS can be calculated using the Equation 14, where θ is the inclination angle between the time axis and the tangent to the crack growth curve drawn from the origin (Senda et al., 1971).

$$t = \frac{L_{max}}{V} \quad \text{(Equation 13)}$$

$$CSS = tg(\theta) \quad \text{(Equation 14)}$$

Figure 28 — Estimation of CSS crack susceptibility index from the relationship between maximum crack length and percent augmented strain

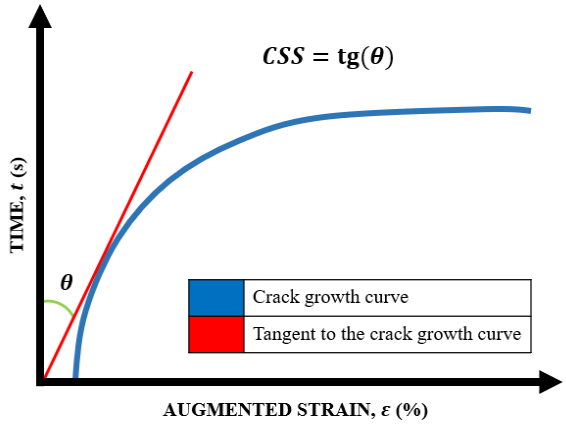

Source: Senda et al. (1971), adapted.

2.5 Shielded Metal Arc Welding

Shielded metal arc welding (SMAW) utilises an electric arc to weld a covered electrode and a weld pool. As shown in Figure 29, the covered electrode consists of a metal wire core (the filler metal) and a covering. During welding, the decomposition of the covering generates a gaseous shield (CO_2 or/and H_2) and a protective slag that isolates the metal droplets and the weld pool from environmental action (Kou, 2002; Shravan et al., 2023).

Figure 29 — Schematic representation of SMAW

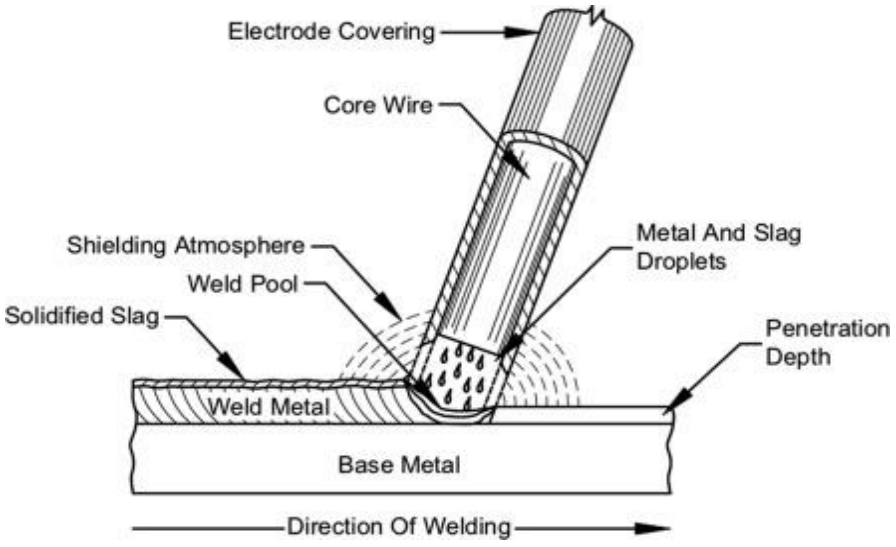

Source: Stewart (2021).

The creation of the electric arc occurs by direct contact of the electrode with the workpiece to be welded, which provokes a short circuit that causes heating. Because of the heat

of the arc, the ionisation conditions are maintained (a plasma sustains the current in the arc and the ionised state of the gas). When the arc is created, the welder identifies the weld pool and raises the electrode to an adequate arc length, aiming for an appropriate electrode consumption condition; if the current is greater than enough, the metal core wire may be overheated, causing the covering to burn before it reaches the tip. As the welding proceeds, the welder controls the feed rate and weld trajectory and must constantly verify various characteristics of the process, such as the flow of the solidifying slag, the wetting of the weld bead, and the stability of the arc (Afriansyah, Arifin, 2020).

The electrical circuit that supports the arc of the SMAW to transform an electrical line into heat is given in Figure 30. The power source has two distinct output terminals; in a series circuit, one is connected to the electrode, and the other is connected to the workpiece. Thus, the electrode behaves as a resistor. The essential elements of this circuit are the welding cable, the electrode holder, and the connection between the metal wire core and the workpiece (Afriansyah, Arifin, 2020).

Figure 30 — Typical welding circuit for SMAW

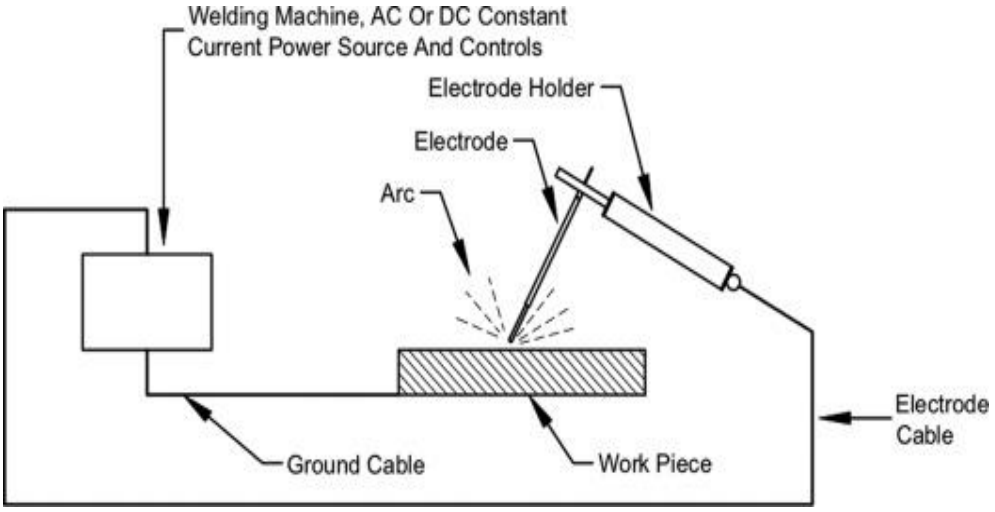

Source: Stewart (2021).

SMAW is a manual welding process and one of the most commonly used processes, principally for industrial applications. Its advantages are that it requires simple, inexpensive, and portable equipment and does not necessitate additional shielding gas (Kou, 2002; Afriansyah, Arifin, 2020; Marques, Modenesi, Bracarense, 2017). In the oil and gas industry, SMAW is commonly applied to execute repairs, fabrication, and maintenance activities.

For appropriate electrode selection, it is necessary to consider the technological, operational, and economic characteristics, such as chemical composition, weld position, metal

transfer, weld bead geometry, slag, generation of gases, and arc creation and maintenance. The electrode covering may have various effects on welding. For example, its consumption 1) facilitates arc creation and maintenance; 2) adjusts the weld metal composition by the addition of alloying elements, such as Mn and Ni, and by eliminating impurities through slag formation; 3) may promote weld metal deoxidation, desulphurisation, and dephosphorization; and 4) may reduce the cooling rate (Marques, Modenesi, Bracarense, 2017).

The electrode covering can be classified according to its composition. The welds used during the development of the present Thesis utilised basic and rutile electrodes. The basic electrodes contained 25-40% calcium carbonate ($CaCO_3$) and 20-25% fluorite (CaF_2), generating basic slag. The decomposition of $CaCO_3$ results in CO_2 formation, and this gas, in addition to slag, is responsible for weld metal protection. Metal transfer is caused by large drops, which may cause some spatter. Having no organic components, basic electrodes produce low-hydrogen-content welds, which are also influenced by adequate storage and drying. This is one rationale for its use for high-responsibility applications. Another rationale is the good mechanical properties of the weld bead (Marques, Modenesi, Bracarense, 2017).

The rutile electrode is composed of 45-55% rutile (TiO_2). This type of covering promotes very favourable operational conditions, principally related to slag removal after welding. Its hydrogen content is greater than that of basic electrodes, requiring careful drying. The weld beads produced by rutile electrodes have a good superficial appearance (Marques, Modenesi, Bracarense, 2017).

The American Welding Society (AWS) specification used in this work for the classification of covered electrodes for arc welding of stainless steels is AWS A 5.4 (Afriansyah, Arifin, 2020).

3 WELDABILITY EVALUATION OF DISSIMILAR CORROSION-RESISTANT ALLOYS WELD METALS FOR HIGH-TEMPERATURE SERVICE USING TRANS-VARESTRAINT TEST

3.1 Abstract

The flare in the oil and gas industry commonly consists of austenitic stainless steels (ASSs), which are highly recommended for application at high temperatures and in reducing/oxidising atmospheres. However, several failures of ASS components in oil and gas production and refining have been reported in the literature, mostly related to the harsh operation conditions and to the fabrication and repair per welding process. Therefore, this work aimed to assess the weldability of consumable electrode candidates for use in the fabrication and repair of flares through the Trans-Varestraint test. The welds via shielded metal arc welding using three filler metals: the ASS electrodes AWS E310-15 and AWS E347-17 and the nickel-based alloy electrode AWS ENiCrFe-2. The ASSs AISI 310S and AISI 304H were selected as the base metals. The weldability was evaluated based on the susceptibility of the weld metal to solidification cracking, which was determined through the critical strain, saturated strain, maximum crack length, maximum crack distance, total crack length, and critical strain speed. Samples from the fusion zones were subjected to chemical composition analysis. The chemical composition data were utilised for thermodynamic simulation, which, along with differential thermal analysis (DTA) and optical microscopy observation, aimed to understand the solidification route of the weld metals. Considering all the parameters investigated, the ranking from least to most susceptible to the solidification cracking weld combination was (AISI 310S + AWS E347-17) > (AISI 304H + AWS E347-17) > (AISI 304H + AWS E310-15) > (AISI 310S + AWS E310-15) > (AISI 304H + AWS ENiCrFe-2) > (AISI 310S + AWS ENiCrFe-2). The fusion zones resulting from the welds with the AWS E347-17 electrode had a duplex microstructure of austenite and δ-ferrite, and the presence of δ-ferrite was beneficial for preventing solidification cracking. The welds with the AWS E310-15 electrode solidified in the fully austenitic mode, which is favourable for cracking. The fusion zones of tests using AWS ENiCrFe-2 were composed of the γ-Ni fcc phase, and evidence of the precipitation of Nb(C,N) was found in the interdendritic volumes. The formation of secondary phases may have some influence on the cracking propensity of these weld metals, explaining the lower weldability.

Keywords: austenitic stainless steel; dissimilar welding; weldability; Trans-Varestraint test; thermodynamic simulation; differential thermal analysis.

3.2 Introduction

Austenitic stainless steels (ASS) are widely utilised to manufacture components for harsh service conditions. Typical applications include high-temperature and carbonaceous reducing/oxidising atmospheres, such as those in the oil and gas, petrochemical, steam power, and nuclear industries (Ghalambaz et al., 2017; Pardal et al., 2011; Yousefi, Farghadin, Farzadi, 2015). Alloys of AISI 300 grade are the most employed in the oil and gas industry. The flare, an indispensable component for ensuring operational and environmental safety, is frequently made of AISI 310 or AISI 321 (Yousefi, Farghadin, Farzadi, 2015). Flares are responsible for the disposal through burning of gases from pressure relief events, harmful gases, and light liquids originating during oil and natural gas processing. The gases are primarily hydrocarbons, carbon dioxide (CO_2), hydrogen sulphide (H_2S), sulphur dioxide (SO_2), chlorine (Cl_2), and hydrogen chloride (HCl) (Shore, 1996; Mahdi, Esmaieli, 2020).

The ASSs are very resistant to high-temperature oxidation. However, the literature reports many cases of failure of components made of these alloys in the context of oil and gas production and refining (Ghalambaz et al., 2017; Pardal et al., 2011; Kaewkumsai, Khoraeng, Sathirachinda, 2013). In this application, the degradation of ASSs often occurs due to metallurgical phenomena, such as sensitisation, carburising, carbides and sigma phase precipitation, stress corrosion cracking, and hydrogen embrittlement (Yousefi, Farghadin, Farzadi, 2015; Kaewkumsai, Khoraeng, Sathirachinda, 2013; Neuharth, Cavalli, 2015).

Notably, welding during fabrication or repair may also lead to potential failures (Ghalambaz et al., 2017; Mahdi, Esmaieli, 2020). Generally, flare parts are joined by gas tungsten arc welding (GTAW) or shielded metal arc welding (SMAW) processes. The welding presents a significant challenge due to the high cooling rates reached, which lead to nonequilibrium solidification, microsegregation, and potential rejection of impurities from the solid toward the interdendritic liquid. These factors are crucial for the occurrence of solidification cracking (Katayama, Fujimoto, Matsunawa, 1985).

The solidification cracks form in the fusion zone along solidification grain boundaries and solidification subgrain boundaries. This type of cracking is caused by low melting point eutectic liquid phases that accumulate in the mushy zone in the last stages of solidification, allowing the separation of cells or grain boundaries when under tensile stresses, thermal contractions, and/or solidification shrinkage during the weld metal cooling (Apblett, Pellini, 1954; Sutton, 2013; Cross, 2005). The formation and propagation of these cracks occur at temperatures close to the *solidus* temperature and are influenced by the thermal cycle,

solidification range, and restraint intensity (Cross, 2005; Santillana et al., 2012; Safari, Forouzan, Shamanian, 2012).

Solidification cracking is a major concern for preventing failures related to welding, once it affects the weldability of the material. The weldability is defined by the American Welding Society (AWS) as “the capacity of a material to be welded under fabrication conditions imposed into a specific suitably designed structure and to perform satisfactorily in the intended service” (Dupont, Lippold, Kiser, 2009). Lippold (2005) affirmed that weldability encompasses several characteristics of a material subjected to welding, such as the resistance to metallurgical degradation. Thus, among other factors, weldability is intrinsically related to the material′s susceptibility to solidification cracking.

Weldability tests are necessary for an adequate evaluation of solidification cracking susceptibility. Augmented restraint tests are largely employed in which an external load induces weld pool deformation (Campbell, Walsh, 1993). The Varestraint and Trans-Varestraint tests are among the most utilised augmented restraint tests (ISO, 2005). The Varestraint test, developed by Savage and Lundin (1967), consists of submitting a specimen to flexural loading on the plane parallel to the welding direction. The flexural loading is applied towards the end of the welding process to deform the weld pool and its adjacencies according to a predefined strain. In turn, the Trans-Varestraint test (TVT) was developed for researchers from Osaka University as a modification of the Varestraint test and aims to analyse the solidification cracking precisely. In TVT, the specimen is bent by a load applied on the plane perpendicular to the welding direction across the weld bead, inducing the cracks to form restricted to the fusion zone (Senda et al., 1971; Kannengiesser, Boellinghaus, 2014; Arata et al., 1976; Arata et al., 1977).

The results from Varestraint and Trans-Varestraint tests enable the determination of a material's threshold and the saturated strain. The threshold or critical strain (ε_{cr}) is the limit strain from which cracking initiates. The saturated strain (ε_{st}) is defined as the strain from which the length of the cracks no longer increases considerably, indicating that they have propagated the entire length of the crack susceptible region (Dupont, Lippold, Kiser, 2009). Also, the length of the cracks formed due to the tests can be measured aiming to ascertain several variables, such as: the maximum crack length (MCL), which corresponds to the size of the most extended crack; the maximum crack distance (MCD), equal to the maximum distance that a crack grew parallel to the welding direction; and the total crack length (TCL), which is the sum of the lengths of all the cracks identified (Statharas et al., 2019).

The values of ε_{cr}, ε_{st}, MCL, MCD, and TCL are frequently utilised to compare different materials regarding susceptibility to solidification cracking. The qualitative and quantitative evaluation of solidification cracking susceptibility to rank materials can be accomplished using various methodologies. The standard ISO TR 17641-3 [17] established an analysis based on the plot of curves of augmented strain *versus* TCL. Lippold and Lin (1996) proposed a methodology that analyses the solidification cracking temperature range (SCTR), which depends on the MCD, cooling rate, and welding velocity.

Through the conventional Varestraint test, Divya et al. (2023) evaluated the weldability of 304HCu stainless steel, an alloy developed as a modification of 304 SS with greater resistance to high-temperature creep, fatigue, oxidation, and corrosion. The results showed a critical strain of 1% and a saturated strain of 4%. The MCL at the ε_{st} was 1.8 mm, approximately. The authors commented that 304HCu is more susceptible to cracking at higher restraint than the stabilised 347 and 321 steels. By contrasting, the findings of Srinivasan et al. (2008) affirmed Nb stabilised 347 steel has a ε_{cr} of 0.25% and MCL at 4% of 0.9 mm, whereas Ti stabilised 321 steel has a ε_{cr} of 0.5% and MCL at 4% of 0.4 mm.

Naffakh et al. (2008), applying the Varestraint test, assessed the weldability in dissimilar welds between the base metals 310 solution-annealed ASS and as-cast Alloy 657. They examined four filler metals: Inconel 82, Inconel A, Inconel 617, and 310 ASS, and conducted test at the strain levels of 1%, 2%, and 4%. Among the nickel-based filler metals, the Inconel 82 showed a higher tendency to form solidification cracking; it presented cracks at 1% of strain and high crack lengths, while the other welds only started developing cracks at 2%. The TCL of Inconel 82 and Inconel 617 welds did not increase as the augmented strain increased from 2% to 4%, indicating a ε_{st} of 2%. On the other hand, the ε_{st} of the welds with Inconel A and 310 ASS appeared to be higher than 4%.

The critical strain rate to the time required to cause cracking (CSS) is another criterion used to assess and compare the solidification crack susceptibility of different materials (SENDA et al., 1971). Senda et al. (1971) assessed the CSS of several materials, including AISI 304 and AISI 310, which were 65×10^{-3} and $2{,}1 \times 10^{-3}$, respectively. This means the solidification cracking susceptibility of AISI 310 is much higher than in AISI 304. Related to the CSS of austenitic stainless steel and nickel alloy weld metals, the literature lacks recent information.

Although the weldability of austenitic stainless steels and nickel-base has already been studied in many works, the solidification cracking resistance of these materials, when submitted to dissimilar welding, can be very distinct. In general, the susceptibility to

solidification cracks in weld metals is affected by changes in chemical composition, solidification path, and microstructure. Particularly in dissimilar metal welding (DMW), these factors are influenced by the difference between base and filler metal chemistry, and, consequently, by the dilution level. The dilution is defined as the change in the composition of the filler metal resulting from its mixing with the base metal (Dupont, Lippold, Kiser, 2009). Here, it is worth mentioning that Lippold and Kotecki (2005) affirm that the welding of two stainless steels (e.g., materials with similar microstructure and distinct chemical composition or materials with different alloy content and microstructure) can be considered a DMW, can give rise to many microstructural combinations. The authors also highlight the DMW of ASSs to nickel-base alloys, commonly utilised to produce components resistant to more corrosive environments and that have good strength at high temperatures.

Based on the preceding discussion, this work aimed to assess weldability through a modified Trans-Varestraint test of consumable electrodes suitable for manufacturing and repairing flare components. This research provides insights into the metallurgical aspects of solidification cracking in corrosion-resistant alloys subjected to dissimilar welding. It identifies the weld metal most susceptible to cracking and examines its cracking behaviour under increased strain. The study also offers recommendations for specific base and filler metal combinations that are suitable or unsuitable for this application.

3.3 Experimental procedure

AISI 310S and AISI 304H were selected as the base metals in this work to simulate the flare conditions immediately after fabrication and before operation. Flares are frequently manufactured using AISI 310S. However, this alloy is very susceptible to solidification cracking due to its chemical composition, which leads to a fully austenitic microstructure. The AISI 304H is another austenitic stainless steel widely used for high-temperature operation. Both alloys were utilised in this work to verify the solidification cracking behaviour of fusion zones resulted from their dilution with the filler metals. Table 2 shows the chemical composition of the base metals.

Table 2 — Chemical composition of the base metals (wt.%)

Base metal	Fe	Cr	Ni	Mn	Mo	Nb	V	Cu	Ti	Si	P	S	C
AISI 310S	53.6	24.9	18.3	1.4	0.02	0.016	0.06	0.065	0.01	0.70	0.01	0.0003	0.052
AISI 304H	71.5	17.9	8.1	1.1	0.18	0.023	0.05	0.153	0.006	0.42	0.01	0.0006	0.045

Source: elaborated by the author.

The welds were performed with a manual SMAW process. The following electrodes were applied: AWS E310-15 ASS, AWS E347-17 ASS, and AWS ENiCrFe-2 nickel-base alloy. The three types of welding consumables had the diameter of 3.2 mm. Their chemical composition, shown in Table 3, was measured in samples of padding welds deposited following the procedure described in the standard ASME BPVC.II. C–2015/SFA-5.4 (ASME, 2015).

Table 3 — Chemical composition of filler metals (wt.%)

Filler metal	Fe	Cr	Ni	Mn	Mo	Ti	Si	P	S	C
AWS E310-15	50.4	26.1	21.2	1.8	0.06	0.01	0.21	0.02	0.01	0.17
AWS E347-17	67.9	20.4	9.5	1.0	0.17	0.02	0.93	0.02	0.01	0.04
AWS ENiCrFe-2	6.7	15.6	73.2	2.1	1.64	0.11	0.54	0.015	0.003	0.03

Source: elaborated by the author.

The AWS E310-15 electrode has a basic covering and is generally used for welding AISI 310S. The AWS E347-17 (rutile-acid-covered) and the AWS ENiCrFe-2 (basic-covered) consumables underwent testing to assess the effectiveness of the weld metals in preventing solidification cracking. It is essential to mention that the electrodes were dried in a furnace at 250 °C for 90 minutes to remove any moisture absorbed during storage and then maintained in an oven at 110°C. Immediately before the welding, they were allocated in a quiver at 80 °C.

The conventional Trans-Varestraint test methodology proposes the remelting of an existent weld by the tungsten inert gas (TIG) process (Senda et al., 1971). However, the present work adopted the modified TVT method developed by the Welding Research and Technology Laboratory (Miranda et al., 2018). This modified methodology involves filling a groove machined in the test plate. This allows for assessing susceptibility to solidification cracking, taking into account dilution and other welding variables. These factors are crucial in investigating the weldability of dissimilar welds.

The specimens consisted of $150^{W} \times 100^{L} \times 10^{t}$ mm plates. Before machining the grooves, various welding parameters were tested to determine the optimal setting. These tests involved depositing beads of each filler metal onto base metal plates. The welding parameters that provided stable arc and efficient metal transfer was defined to ensure high-quality welds

with good appearance. The geometry of the weld beads was used to define the dimensions of the grooves to be machined into the base metal plates for fabricating the TVT specimens. Two grooves (A and B) were designed and machined. The dimensions of grooves A and B are presented in Table 4.

Table 4 — Dimensions of the grooves utilised for tests with each filler metal

Filler metal	Groove	Length (mm)	Height (mm)	Width (mm)	Radius (mm)	Area (mm^2)	Volume (mm^3)
AWS E310-15	A	100	2.00	9.00	6.06	12.12	109.08
AWS E347-17							
AWS ENiCrFe-2	B	100	3.00	10.00	5.67	11.34	170.10

Source: elaborated by the author.

Figure 31 shows the TVT's specimens. The grooves A and B were projected to accommodate the weld beads deposited by the ASS and AWS ENiCrFe-2 electrodes, respectively. It was necessary to guarantee that the weld beads' upper surface was level with the plate surface to ensure an equal distribution of stresses in the weld bead during TVT.

Figure 31 — Representation of the TVT specimens: (a) plate with machined groove and (b) geometry of grooves A and B

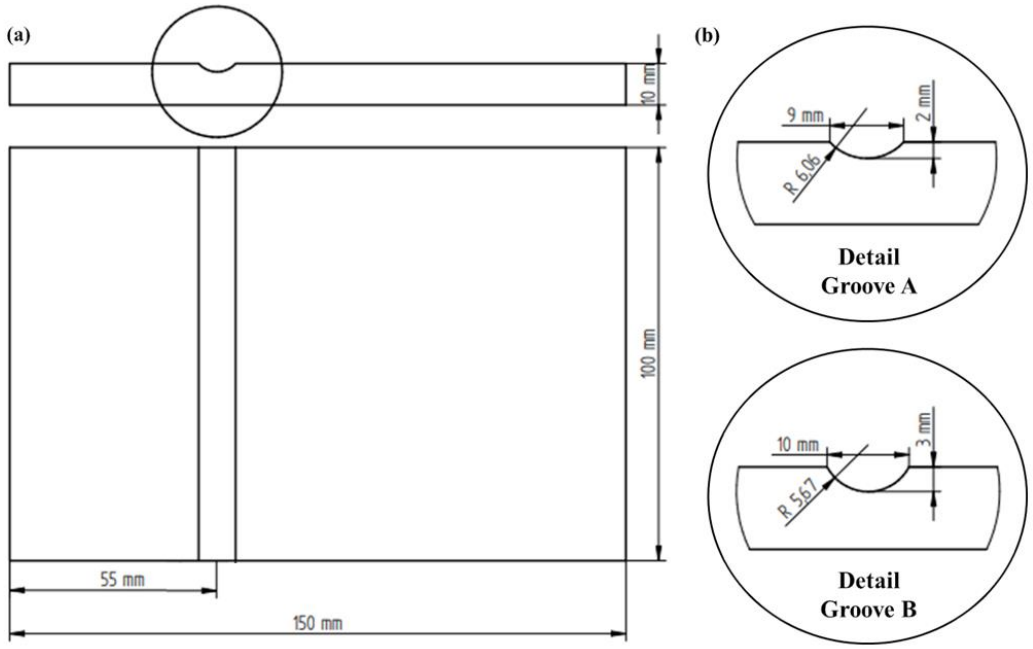

Source: elaborated by the author.

Table 5 shows the welding parameters that resulted in appropriate weld beads. The set welding speeds are informed, as are the average values of current, voltage, heat input, and electrode travel angle. The influence of the discrepancies in the heat input of the experiments

with the AWS E347-17 electrode on the results obtained in this work is discussed afterwards.

Table 5 — Welding parameters

Base metal	Filler metal	Speed (mm/s)	Current (A)	Voltage (V)	Heat input (kJ/mm)	Electrode travel angle
AISI 310S	AWS E310-15	2.5	107	26.3	1.12	0°
	AWS E347-17	2.0	123	26.4	1.62	
	AWS ENiCrFe-2	2.5	102	27.3	1.11	
AISI 304H	AWS E310-15	2.5	102	27.1	1.11	
	AWS E347-17	2.0	117	26.3	1.54	
	AWS ENiCrFe-2	2.5	100	27.3	1.09	

Source: elaborated by the author.

The welding speeds of 2.0 and 2.5 mm/s are sufficiently slow to maintain the weld pool's elliptical shape. If the welding speeds were higher, the weld pool would be more elongated, due to changes in heat flow conditions. This could alter the weld pool from elliptical to teardrop-shaped. Consequently, the length of the longest crack, which is typically initiated in the weld centre, would be maximised to the greatest extent possible (WANG et al., 2015).

Figure 32 illustrates the TVT equipment developed by Miranda et al. (2018). The main components indicated in the schematic are the unidirectional trajectory manipulator, speed reference pointer, roller, die, covered electrode, and specimen.

Figure 32 — Illustration of the Trans-Varestraint test equipment: (a) general representation of the components; specimen (b) before and (c) after bending

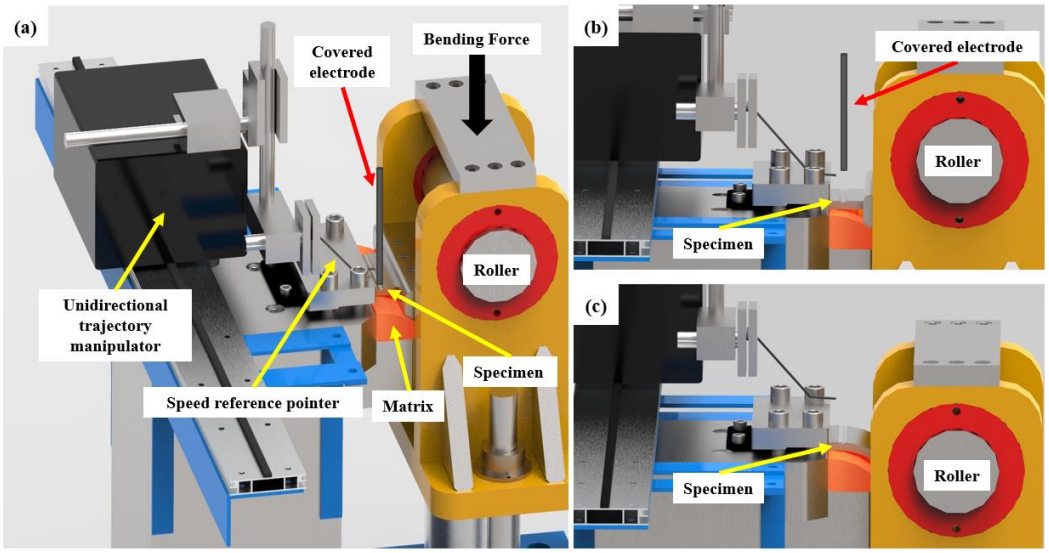

Source: elaborated by the author.

The specimens are positioned in the equipment just above the die, whose radius controls the strain level applied according to Equation 15, where ε the strain percentage

(augmented strain), t is the specimen thickness and R is the radius of curvature of the bending block (die) (Miranda et al., 2018).

$$\varepsilon = \frac{t}{2R} x\ 100\ (\%) \qquad \text{(Equation 15)}$$

Once the welding process was carried out manually, a reference pointer was coupled to a unidirectional trajectory electronic manipulator to guide the welder in controlling the welding speed, which should be the same as the one defined through the exploratory tests and not differ significantly between experiments. Variations in welding speed could lead to discrepancies in the length of the cracks resulting from the test.

The procedure begins with the welder opening the electric arc and proceeding to fill the groove, ensuring that the covered electrode′s motion speed is synchronised with the "speed reference pointer". When the welder reaches 60% (60 mm) of the groove′s total length (100 mm), a specific bending force is applied to the specimen. This force is achieved by imposing a load on the roller, causing the specimen to deform following the die radius.

The bending speed was approximately 100 mm/s, which is fast enough to ensure that crack initiation and propagation occur before the weld pool solidification is completed. The apparatus used for performing the TVTs is equipped with a bladder-type hydraulic accumulator that generates gas expansion inside, increasing the oil flow and enabling the system to apply the bending force almost immediately. The rapid bending speed is crucial for the controlled deformation process and the desired response of the welded plate.

The scope of this work first comprised performing Trans-Varestraint tests for the six combinations of base metal and filler metal using seven strain levels: (a) 0.5%, (b) 1%, (c) 2%, (d) 3%, (e) 4%, (f) 6%, and (g) 8%. Thus, 42 tests were performed to understand the behaviour of each weld metal with increasing strain in terms of crack length. The specimens tested with a strain of 8% were not machined, as illustrated in Figure 1. To achieve this strain level in the TVT equipment, the groove was machined so that the distance from the plate extremity to the groove centre was 65 mm instead of 55 mm.

Moreover, additional tests were conducted to improve the reliability of the crack measurements. Based on the preliminary test results, three strain levels were selected: (a) 1%, (b) 3%, and (c) 6%. The matrix of experiments consisted of triplicate tests of the six pairs of base metal and filler metal, totalling 54 tests. Considering that the parameters of the preliminary tests were the same as those of the 18 experiments on the matrix, only 36 additional tests were necessary.

After TVT testing, each specimen′s weld bead surface underwent a thorough polishing process using a microgrinding machine, felt tips, and polishing paste for slag removal. It is important to note that specimens from tests involving AWS E310-15 and AWS ENiCrFe-2 electrodes required an additional cleaning step due to the hard adherent slag resulting from basic coating. This kind of slag was particularly challenging to remove without causing surface damage, which would lead to inaccurate crack measurements. Alternatively, the weld beads in question underwent pickling using a 10% HCl aqueous solution for 5 minutes. Following this, they were extensively rinsed with water, neutralised in a 5% NaOH aqueous solution for 10 minutes, and then thoroughly rinsed again.

Following the cleaning processes, the surface of the specimens was inspected with a stereo microscope. The cracks were photographed and measured. The present study focused on the qualitative and quantitative evaluation of solidification cracking susceptibility, determining for every specimen the (1) maximum crack length (MCL), which corresponds to the size of the most extended crack; (2) maximum crack distance (MCD), which is equal to the maximum distance that a crack grew parallel to the welding direction; and (3) total crack length (TCL), which is the sum of the lengths of all the cracks identified (STATHARAS et al., 2019). The crack measurement data from the matrix of experiments were analysed with Statistica software via analysis of variance (ANOVA) to evaluate the influence of the base metal, filler metal, and applied strain on the susceptibility to solidification cracking.

The qualitative and quantitative evaluation of hot crack susceptibility aiming to rank materials can be accomplished using various methodologies. In the present study, this evaluation initially focused on verifying the critical strain (ε_{cr}) and saturation strain (ε_{st}) for each combination of base metal and filler metal. The critical strain is the limit strain from which cracking initiates, and the saturation strain is defined as the strain from which the length of the cracks does not increase considerably. This verification was carried out by plotting the curves of strain *versus* TCL, as established in the standard ISO TR 17641-3 (2005). The methodology proposed by DuPont, Lippold and Kiser (2009), which consists of analysing curves of strain *versus* MCD, was also applied.

The CSS was another criterion utilised here to evaluate the susceptibility to solidification cracking of the weld metals. It was determined using a graph with the crack growth curve. The time for cracking development (y-axis) is calculated according to Equation 16, where L_{max} is the maximum crack length and V is the welding speed. After plotting the crack growth curve, the CSS can be calculated by Equation 17, where θ is the inclination angle between the time axis and the tangent to the crack growth curve drawn from the origin (Senda

et al., 1971).

$$t = \frac{L_{max}}{V} \quad \text{(Equation 16)}$$

$$CSS = tg(\theta) \quad \text{(Equation 17)}$$

The weld metals' chemical composition was determined by X-ray fluorescence (XRF), energy-dispersive X-ray spectroscopy (EDS) in a scanning electron microscope (SEM), and optical emission spectroscopy (OES). Furthermore, the contents of C, N, P, and S in the fusion zones were accurately determined. The samples used consisted of chips extracted from the fusion zone of the weld beads. The C and S contents were determined by combustion using infrared technique with the Eltra CS 800 elemental analyser equipment. The N content was assessed by fusion, using the Eltra ON 900 elemental analyser equipment, also employing the infrared technique. The P content was determined by OES using an appropriately calibrated and certified spectrometer to analyse low P levels.

The chemical composition was also employed to predict the solidification modes of the austenitic stainless steel weld metals by calculating the ratio of the chromium equivalent (Cr_{eq}) and nickel equivalent (Ni_{eq}), applying Schaeffler's equations, shown in Equation 18 and Equation 19 (Schaeffler, 1949).

$$Cr_{eq} = \%Cr + \%Mo + 1.5(\%Si) + 0.5(\%Nb) \quad \text{(Equation 18)}$$

$$Ni_{eq} = \%Ni + 30(\%C) + 0.5(\%Mn) \quad \text{(Equation 19)}$$

The same analysis was carried out using the expressions established more recently during the elaboration of the WRC-1992 diagram, shown in Equations 20 and 21 (Kotecki, Siewert, 1992).

$$Cr_{eq} = \%Cr + \%Mo + 0.7/(\%Nb) \quad \text{(Equation 20)}$$

$$Ni_{eq} = \%Ni + 35(\%C) + 20(\%N) + 0.25(\%Cu) \quad \text{(Equation 21)}$$

The values of Cr_{eq}/Ni_{eq} obtained here were compared to the ranges presented in Table 6, which were determined considering the work of Kujanpää et al. (1979), who carried out several Trans-Varestraint tests in austenitic and austenitic-ferritic welds to determine the relationship between the microstructure, solidification mode and solidification cracking.

Table 6 — Relationship between the solidification modes and the Cr_{eq}/Ni_{eq} of stainless steel welds

Solidification mode	Fully austenitic (A)	Primary austenite-secondary ferrite (AF)	Primary ferrite-secondary austenite (FA)	Fully ferritic (F)
Cr_{eq}/Ni_{eq}	< 1.25	1.25 - 1.48	1.48 - 1.95	> 1.95

Source: elaborated by the author based on Kujanpää et al. (1979).

To understand the solidification route of the weld metals obtained, thermodynamic simulations were performed using the software Thermo-Calc® (version 2017b), with the database TCFE8 for weld metals rich in Fe and the database TCNI8 for Ni-rich weld metals. The solidification process was simulated under nonequilibrium conditions by plotting the Scheil-Gulliver solidification curve. Based on the simulation results, the solidification temperature range (ΔT_{sol}) and the brittle range temperature (BTR), which are important parameters for evaluating solidification cracking susceptibility, were estimated. The ΔT_{sol} is determined by Equation 22.

$$\Delta T_{sol} = T_{liquidus} - T_{solidus} \qquad \text{(Equation 22)}$$

The BTR is defined by Santillana et al. (2012) as the temperature interval in which the material experiences the final and critical stages of solidification. These stages are named 2b and 3. The coarsening of dendrite arms and interdendritic separation denotes stage 2b. It initiates at a solid fraction (f_s) of 0.80 and at a temperature known as the zero strength temperature (ZST), when the secondary dendrite arms have already reached out and are interlocked. In Stage 2b, the last liquid fraction present is discontinuously trapped between the dendrites, and the strength of the material is low, so any applied stress may easily result in hot cracking. Stage 3 of solidification begins at a f_s of 0.90. The transition from a dendritic to a grain structure occurs, and thin liquid films with low melting points may still be present at grain boundaries. In this stage, solid-state creep is the only mechanism for the material to adapt to solidification shrinkage and thermal or external stresses. At the end of solidification when the solid fraction ranges from 0.98 to 1, the plasticity of the material increases. The temperature at which the material becomes ductile is named the zero ductility temperature (ZDT).

The BTR can be calculated using Equation 23, where ZST and ZDT are the temperatures corresponding to f_s equal to 0.80 and 0.99, respectively (SANTILLANA et al., 2012).

$$BTR = ZST - ZDT \qquad \text{(Equation 23)}$$

The chemical composition of the weld metals was also utilised to calculate the level of dilution of each combination of base and filler metal through Equation 24, which considers the concentration of an element in the fusion zone (C_{ZF}), in the filler metal (C_{FM}), and in the base metal (C_{BM}). The Fe was the element selected for dilution calculation of the weld metals.

$$D_{EDS} = \frac{C_{FZ} - C_{FM}}{C_{BM} - C_{FM}}\ x\ 100\ (\%) \qquad \text{(Equation 24)}$$

Differential thermal analysis (DTA) was performed on the samples from the fusion zones to obtain a direct estimate of the phase transformation temperatures that occur upon cooling. This analysis utilised heating and cooling rates of 10 °C/min and argon 5.0 gas. The temperature range was 1050 °C to 1450 °C, encompassing the melting points of all the tested samples. The DTA data were compared to the results of the thermodynamic simulations.

DTA was also utilised to stipulate the BTR. This was possible because the extent of reactant conversion (α) can be determined as the fractional change in any physical property associated with the reaction progress. Here, the reaction is the solidification process, and α corresponds to the solid fraction (f_s). When the process progress is measured as a change in heat by DSC/DTA, α, the parameter that reflects the reaction progress from the initial state, is evaluated as the ratio of the current heat change (ΔH) to the total heat released or absorbed in the process (ΔH_{tot}), as shown in Equation 25 (Vyazovkin, 2015).

$$\alpha = \frac{\int_{t_0}^{t}\left(\frac{dH}{dt}\right)dt}{\int_{t_0}^{t_f}\left(\frac{dH}{dt}\right)dt} = \frac{\Delta H}{\Delta H_{tot}} \qquad \text{(Equation 25)}$$

DTA endothermic/exothermic peaks originating from heating/cooling can be utilised to calculate the solid fraction. The f_s is equal to the integral of the DTA peak, with values normalised from 0 to 1 (0 representing the beginning and 1 representing the end of the solidification event) (Vyazovkin, 2015). Thus, the ZST (f_s = 0.80) and the ZDT (f_s = 0.99) were obtained from the DTA cooling curves, and the BTR calculation followed Equation 23.

Samples were taken from the cross-sections of the weld bead specimens to analyse the microstructures of the fusion zones via light optical microscopy (LOM). The samples were subjected to metallographic preparation through grinding, polishing, and electrolytic etching. Table 7 shows the parameters of electrolytic etching. The results from the microstructural analysis were compared to the morphologies expected according to the prediction of solidification modes based on Cr_{eq}/Ni_{eq}.

Table 7 — Electrolytic attachment parameters

Filler Metal	Reagent	Voltage (V)	Time (s)
AWS E310-15	Oxalic acid	2.5	30
AWS E347-17			
AWS ENiCrFe-2	Chromic acid (10%)		60

Source: elaborated by the author.

3.4 Results

Figure 33a displays the deposited weld bead. The area within the red rectangle is the surface region where solidification cracks formed. This area is shown enlarged in Figure 33b, where the identified cracks are outlined in yellow. Figure 33c presents the cross-sectional view of the specimen, with the deformation on the right side is due to the bending. In Figure 33d, an enlarged view of the cross-section is shown, specifically focusing on the weld bead. This clearly shows that the groove has been completely filled, aligning with the condition of minimising weld reinforcement. As a result, the top of the weld sits flush with the surface of the plate. Furthermore, in Figure 33d, the yellow rectangle indicates the presence of a weld undercut. This defect occurred due to the bending movement during welding, which caused the liquid metal to shift to the right side, resulting in inadequate filling.

Figure 33 — Macrographs of a specimen after Trans-Varestraint test: (a) top view; (b) ampliation in the region where the solidification cracks where identified; (c) cross-section view; (d) cross-section ampliation

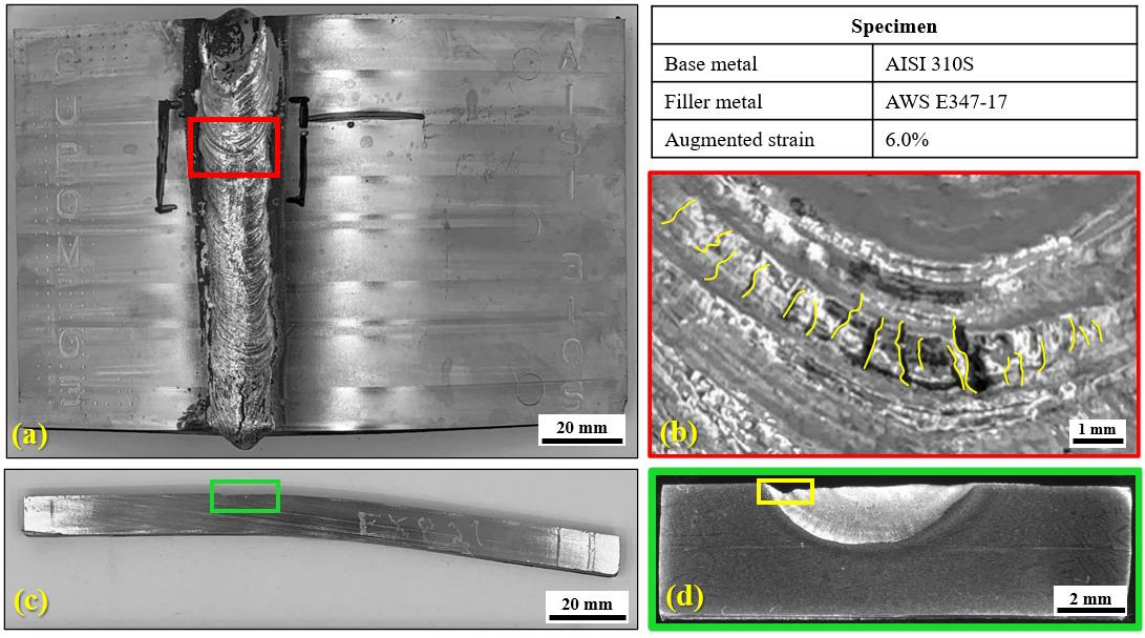

Source: elaborated by the author.

Even though the adequate filling of the grooves has been previously studied some samples exhibited a little reinforcement height. As can be understood by analysing Equation 15,

this altered the strain level applied in the Trans-Varestraint tests. To compare the nominal strain and effective strain levels, the thickness of the specimens tested at each strain level was measured to determine the effective strains. The measurements considered the weld centre, and then the little reinforcement height, when it was present in the weld bead, was taken into account.

Table 8 displays the average effective strain for each nominal strain level applied, compared to the nominal strain levels established prior to the test by selecting a matrix radius to deform a 10 mm thick specimen. For 0.5%, 1.0%, 2.0%, and 6.0% nominal strain levels, the effective strain values were very similar. For 3.0%, 4.0%, and 8.0% nominal strain levels, the differences were more pronounced, at 0.31, 0.43, and -0.46, respectively. Nevertheless, it can be noted that the effective strain did not differ significantly from the nominal strain. Therefore, it was decided to present the results in terms of the nominal strains to enhance the discussion.

Table 8 — Nominal strain and effective strain applied in the Trans-Varestraint tests

Nominal strain (%)	**Effective strain (%)**
0.5	0.53
1.0	1.07
2.0	2.16
3.0	3.31
4.0	4.43
6.0	6.18
8.0	7.54

Source: elaborated by the author.

Figure 34 shows the surface of each specimen tested. The images are zoomed macrographs artificially coloured to highlight in green the test conditions for which cracks were not detected and in light red the test conditions that resulted in cracking. Again, the cracks are outlined in yellow for better observation. The critical strains estimated based on the results presented in Figure 34 are expressed in Table 9 as ranges, once the determination of the exact values of ε_{cr} would require additional tests with strain levels intermediate to those applied in this work.

Table 9 — Critical strains (ε_{cr}) estimated according to Trans-Varestraint tests results

Base metal	**Filler metal**		
	AWS E310-15	**AWS E347-17**	**AWS ENiCrFe-2**
AISI 310S	$\varepsilon_{cr} \leq 0.5\%$	$2\% < \varepsilon_{cr} \leq 3\%$	$\varepsilon_{cr} \leq 0.5\%$
AISI 304H	$0.5\% < \varepsilon_{cr} \leq 1\%$	$1\% < \varepsilon_{cr} \leq 2\%$	$\varepsilon_{cr} \leq 0.5\%$

Source: elaborated by the author.

Figure 34 — Macrographs of the cracks resulting from the preliminary TVT: welds with the base metals (a) AISI 310S and (b) AISI 304H

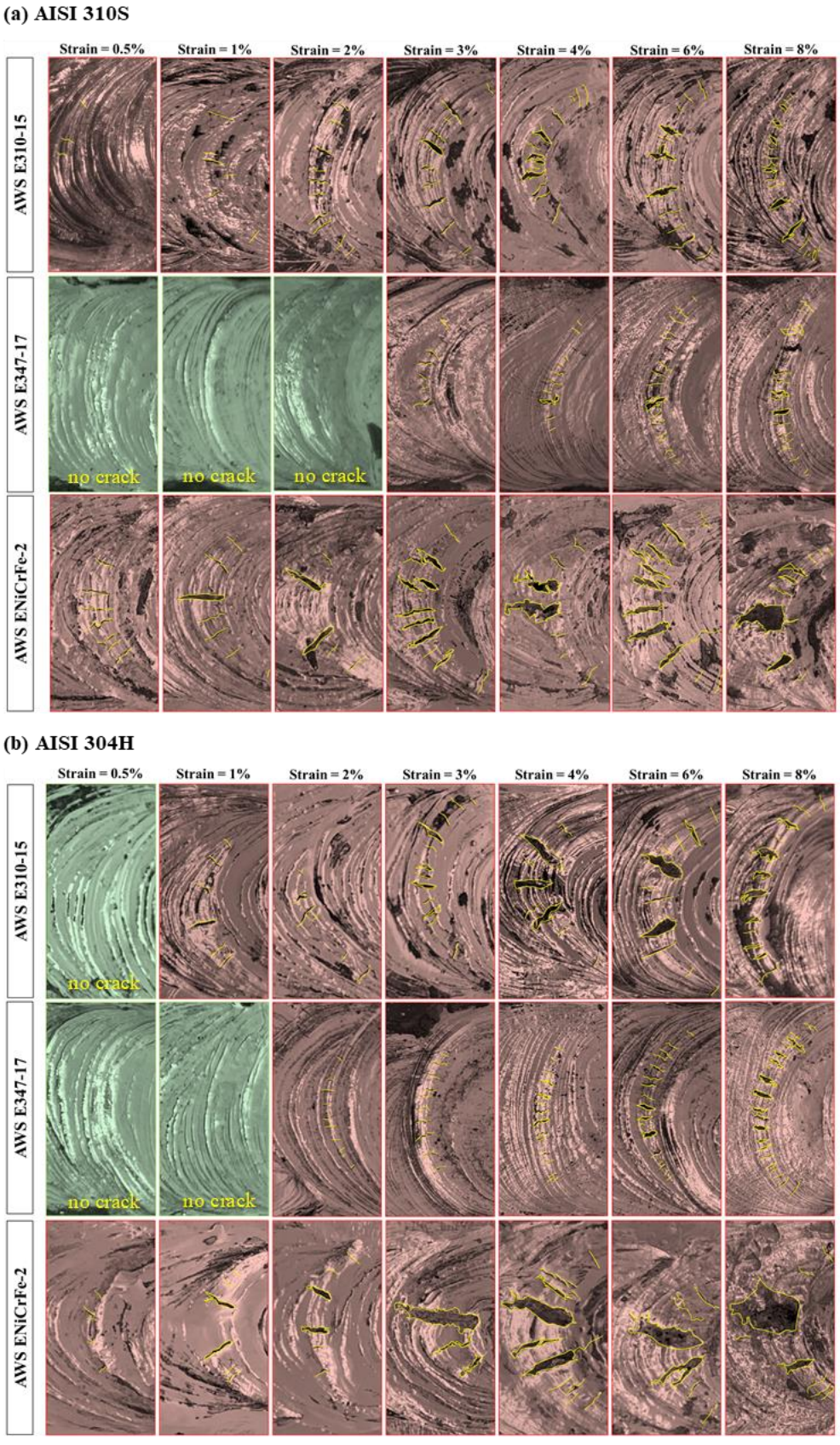

Source: elaborated by the author.

The graphs plotted using crack measurement data are shown in Figure 35, which presents curves correlating the MCL, MCD, and TCL to the augmented strain. The dashed lines are logarithm trendlines. For tests with both base metals, the fusion zones of the weld beads deposited by AWS E347-17 electrode are the least susceptible to solidification cracking, presenting the minor crack lengths and the least significant increase in crack lengths under increased strain.

The similar welding (AISI 310S and AWS E310-15) showed lesser variation in the crack lengths with increasing strain than the AISI 304H and AWS E310-15 weld, even though the combination of this electrode with AISI 304H resulted in a smaller ε_{cr}, not cracking at 0.5% strain. The tests of welds with AWS ENiCrFe-2 as filler metal showed the worst resistance to solidification cracking among the conditions evaluated, having the largest crack lengths.

For the augmented strains of 3%, 4%, 6%, and 8%, Figure 35f informs that the tests with AISI 304H specimens having AWS E347-17 as filler metal presented a higher TCL than the tests with AWS E310-15 electrode. This occurred due to the fact that the test of AISI 304H with AWS E310-15 resulted in a smaller number of cracks, in comparison to the weld with AWS E347-17. Nevertheless, the cracks were more critical, being larger and ticker, as shown in Figure 34b. In turn, more cracks formed due to TVT in the test with AWS E347-17. However, the cracks were smaller and thinner. Even so, this test ended up resulting in a higher TCL.

Figure 35 — Relationship of the crack measurements to the augmented strain: (a,d) MCL, (b,e) MCD, and (c,f) TCL

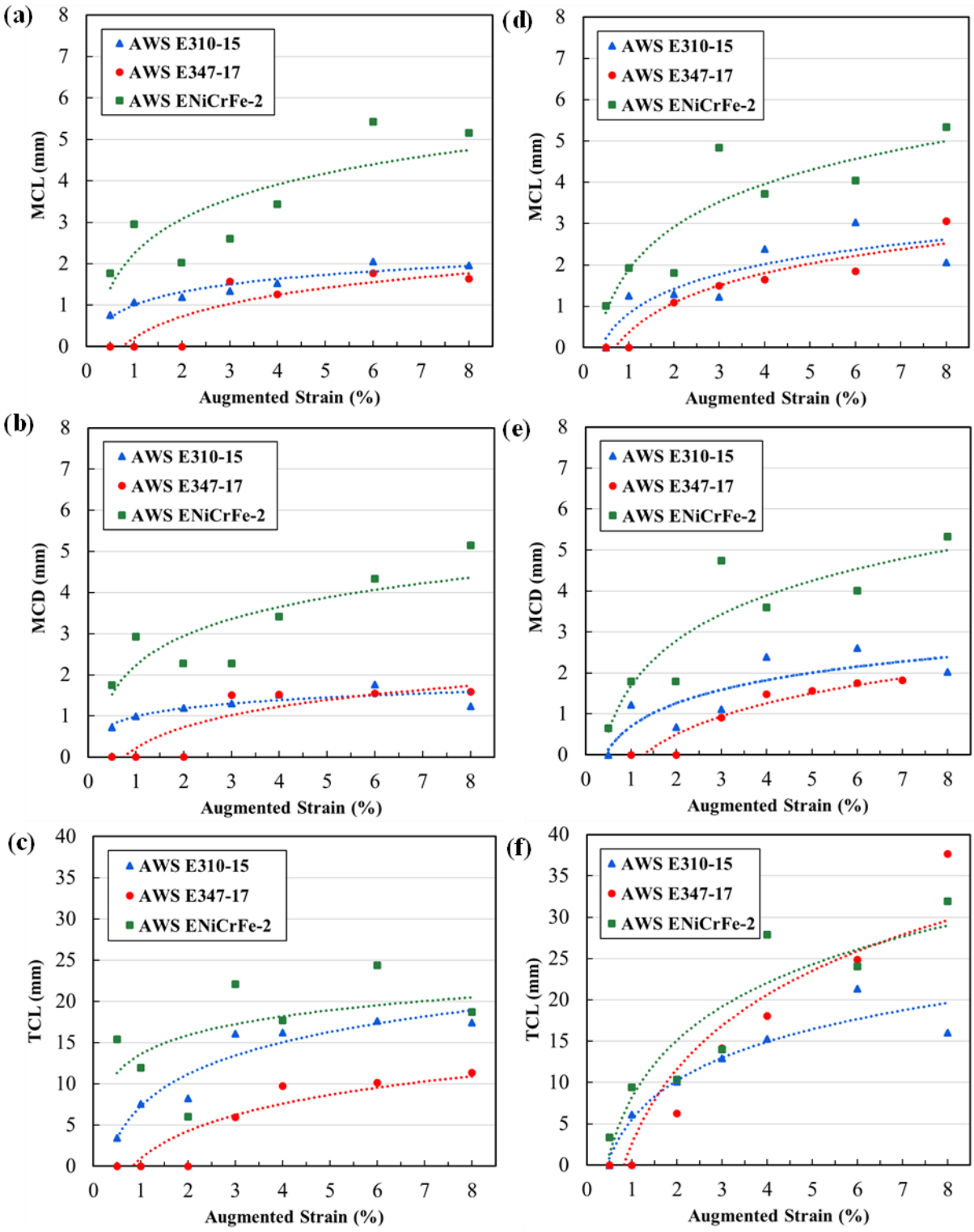

Source: elaborated by the author.

Figure 36 shows examples of the cracks formed during the Trans-Varestraint tests of the specimens of the matrix of experiments, which were carried out for strain levels of 1%, 3%, and 6%. Experiments on the matrix confirmed the behaviour observed in preliminary tests.

The weld metals resulting from the combination of the AWS E347-17 electrode with both base metals did not develop cracks at strains of 1%.

Figure 36 — Macrographs of the cracks resulting from the Trans-Varestraint tests of the matrix of experiments: welds having as the base metals (a) AISI 310S and (b) AISI 304H

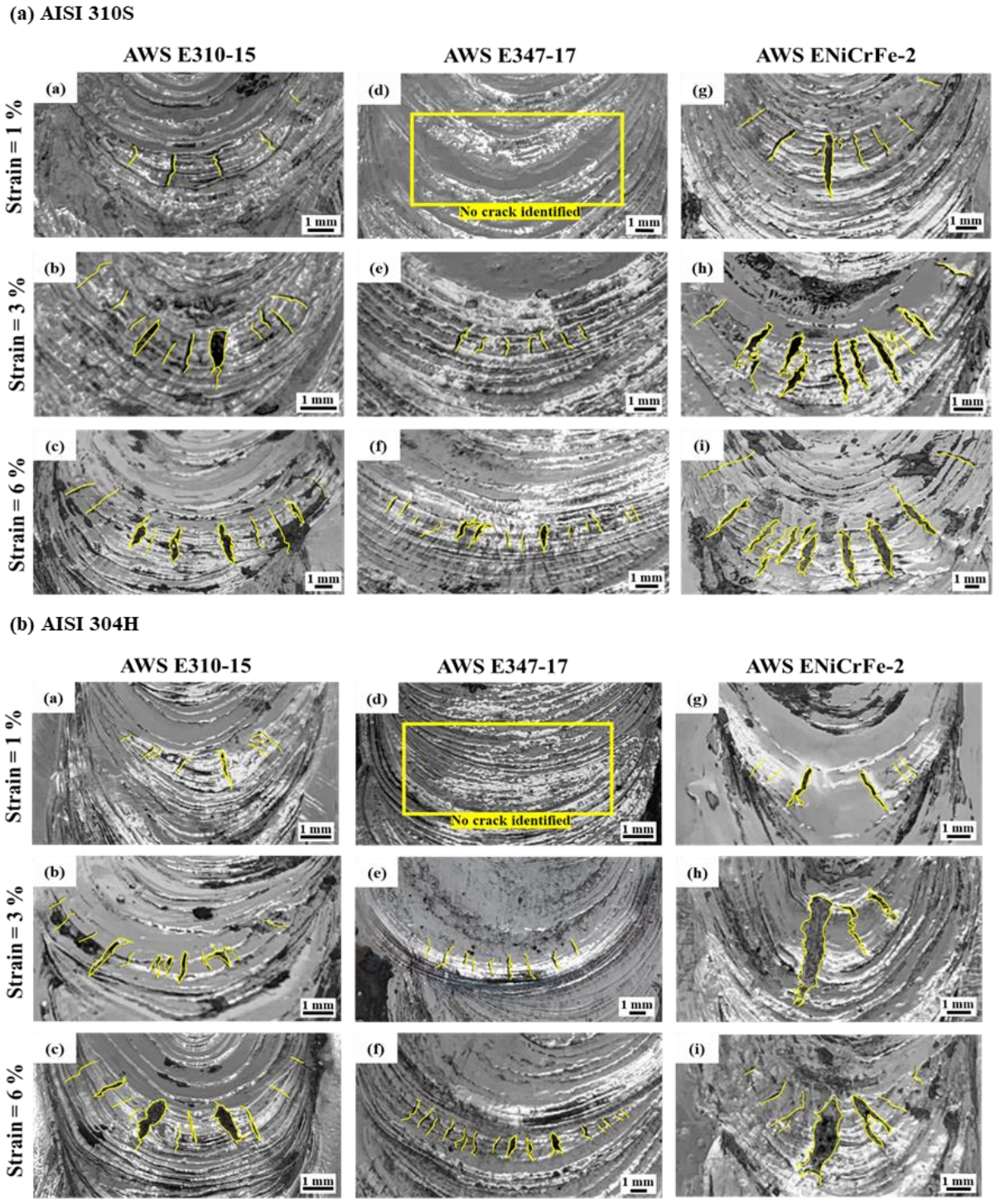

Source: elaborated by the author.

Considering the graphs in Figure 36, the saturated strains were estimated. This analysis considered the curves that correlate MCD and TCL to the augmented strain (Figure 37). Every point is the average of the three lengths collected for each TVT configuration, and the standard deviation is also represented. These results enabled the prediction of the saturated strain with statistical accuracy.

Figure 37 — Graphics of MCL, MCD, and TCL versus augmented strain resulting from the Trans-Varestraint tests of the matrix of experiments

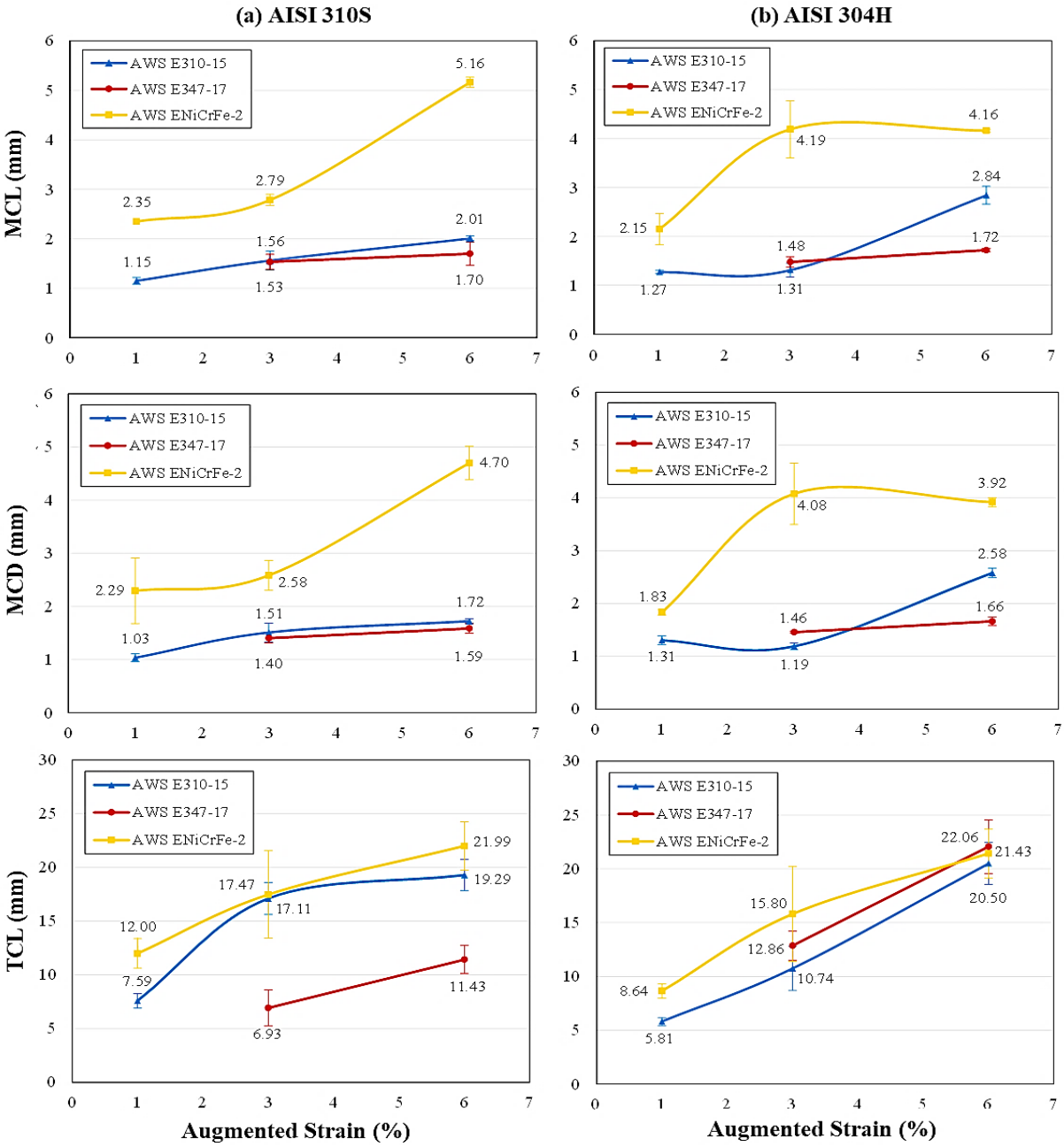

Source: elaborated by the author.

The ranges of saturated strain ranges are informed in Table 10. In comparison to the nickel-alloy weld metals, the length of the cracks of ASS weld metals stabilised at lower strain levels. Furthermore, between the tests with the ASS electrodes, the welds with AWS E347-17 had the lowest saturated strain.

Table 10 — Estimation of the saturated strain for each tested condition

Base metal	Filler metal	Saturation strain (ε_{st}) according to MCD	Saturation strain (ε_{st}) according to TCL
AISI 310S	AWS E310-15	$3\% \leq \varepsilon_{st} \leq 6\%$	$\varepsilon_{st} \geq 6\%$
	AWS E347-17	$3\% < \varepsilon_{st} \leq 6\%$	$3\% \leq \varepsilon_{st} \leq 6\%$
	AWS ENiCrFe-2	$\varepsilon_{st} \geq 6\%$	$3\% \leq \varepsilon_{st} \leq 6\%$
AISI 304H	AWS E310-15	$3\% < \varepsilon_{st} \leq 6\%$	$\varepsilon_{st} \geq 6\%$
	AWS E347-17	$3\% < \varepsilon_{st} \leq 6\%$	$\varepsilon_{st} \geq 6\%$
	AWS ENiCrFe-2	$3\% \leq \varepsilon_{st} \leq 6\%$	$3\% \leq \varepsilon_{st} \leq 6\%$

Source: elaborated by the author.

The TVT of the experimental matrix confirmed the results of the preliminary tests. In Figure 37, mainly for the graphs correlating the MCD to the augmented strain, it is shown the high susceptibility to solidification cracking of the weld metals formed through the dilution of the AWS E310-15 and AWS ENiCrFe-2 electrodes with both base metals. In turn, the tests of the welds with AWS E347-17 as filler metal presented a notorious resistance to solidification cracking; their curves associated with the crack measurements to the applied strain showed the least variation compared to the others.

ANOVA was performed based on the crack measurement results from the tests of the matrix of experiments; thus, it is essential do note that this analysis focused only on the data from tests with three strain levels (1.0%, 3.0%, and 6.0%). The confidence interval was 0.95. Hence, P values higher than 0.05 indicate that the distinction from one group to another is not statistically significant. By the other way, the conditions with statistically significant differences in the evaluated treatment had P values lower than 0.05. Table 11 shows the ANOVA results. The influence of the base metal on the MCL, MCD, and TCL was not statistically significant. Conversely, filler metal and strain treatments greatly affected the crack lengths.

Table 11 — P values of ANOVA resulting from the crack measurements of tests of the matrix of experiments

Crack measurement	Treatment		
	Base Metal	Filler Metal	Strain
MCL	0.53225	*0.00000*	*0.00000*
MCD	0.33324	*0.00000*	*0.00000*
TCL	0.61283	*0.00000*	*0.00000*

Source: elaborated by the author.

The graphics from ANOVA are shown in Figure 38. According to Figure 38a-c, it is possible to verify that the alternation of base metals does not results in significant changing of the crack lengths. Figure 38d-f shows the MCL, MCD, and TCL variations due to the type of filler metal used. Figure 38d-e shows that the extent of the cracks in the fusion zones of the weld beads deposited by the three types of electrodes significantly differ from each other in terms of crack length. Therefore, the influence of the filler metal on the weldability was highly evident.

Figure 38 — Graphics of ANOVA for evaluating the influence of the base metal, filler metal, and strain treatments: (a,d,g) MCL; (b,e,h) MCD, and (c,f,i) TCL

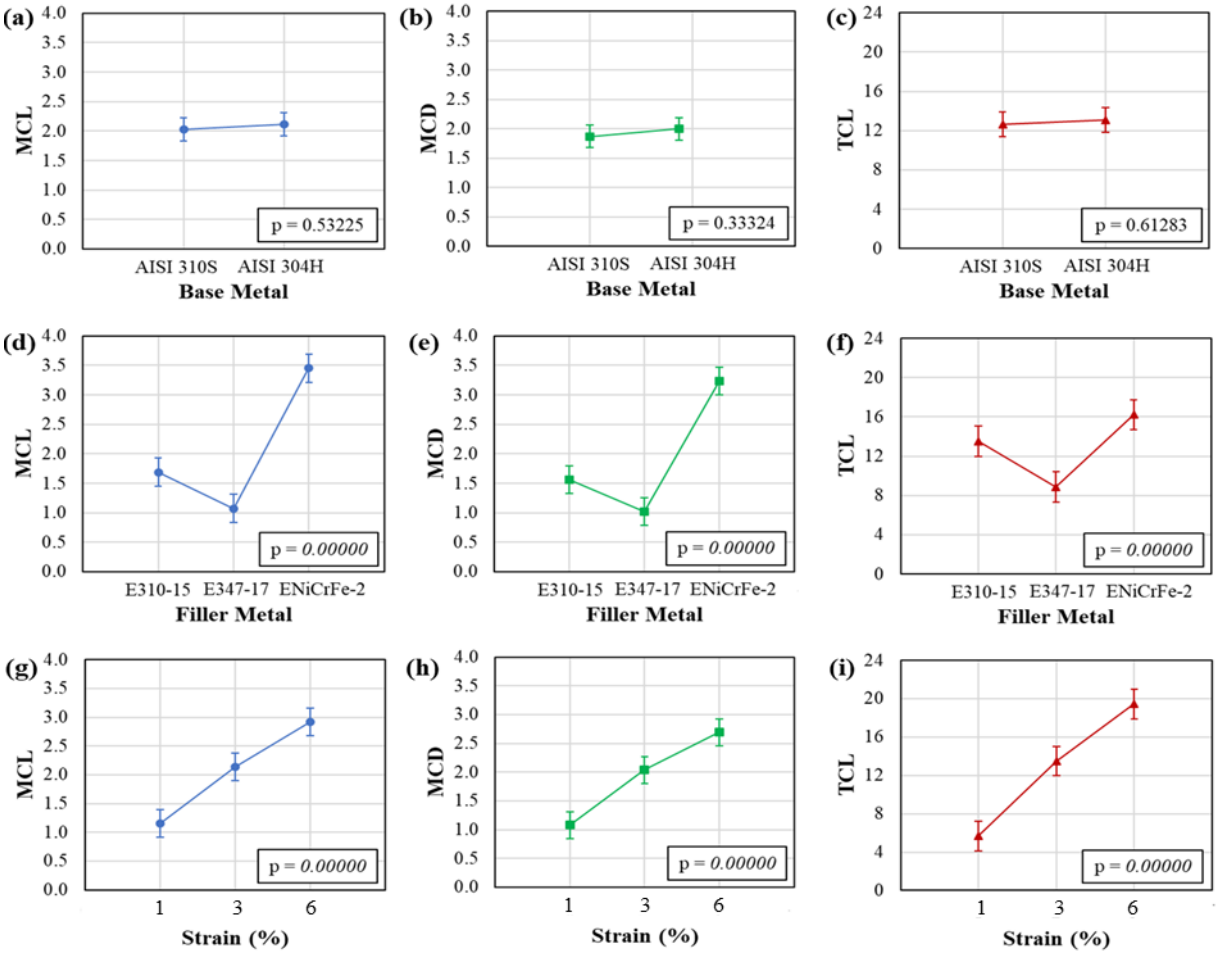

Source: elaborated by the author.

Figure 38 highlights again the fact that the tests with the AWS ENiCrFe-2 filler metal had MCL and MCD values more expressive than those from the tests with other filler metals. However, the comparison of the TCL obtained from tests with AWS NiCrFe-2 to those measured for the welds with AWS E310-15 indicates that, for this parameter, these filler metals yielded very similar TCL values, thereby not presenting a well-defined statistical distinction.

Figure 38g-i shows the effect of the strain applied on TVT on the crack measurements. For the three types of filler metals studied in this analysis, the increase in strain led to a notorious increase in the length of the cracks. This behaviour was expected because the augmented strain is one of the most critical parameters of the Trans-Varestraint test.

Figure 39 presents the results from evaluating the solidification cracking resistance, specifically focusing on the critical strain rate to time required for cracking (CSS) within each type of weld metal. The graphs detail the correlation between the time required for crack formation and the corresponding augmented strain. The crack growth curves, represented by dashed lines, follow logarithmic trendlines. It was observed that welds using AWS ENiCrFe-2 as filler metal exhibited the lowest CSS values, indicating a heightened susceptibility to solidification cracking. This means that these weld metals require a lower strain threshold over a specific time to initiate crack development during the TVT apparatus actuation. In contrast, the specimens tested from AISI 310S and AISI 304H, using AWS E347-17 electrode, presented the highest CSS values, 5.464×10^{-3} (1/s) and 3.690×10^{-3} (1/s), respectively. These values represent a greater resistance to solidification cracking. Therefore, the CSS analysis aligns with and reinforce the conclusions reached through other assessments carried out in the present study.

Figure 39 — Estimation of the CSS value of each weld metal tested

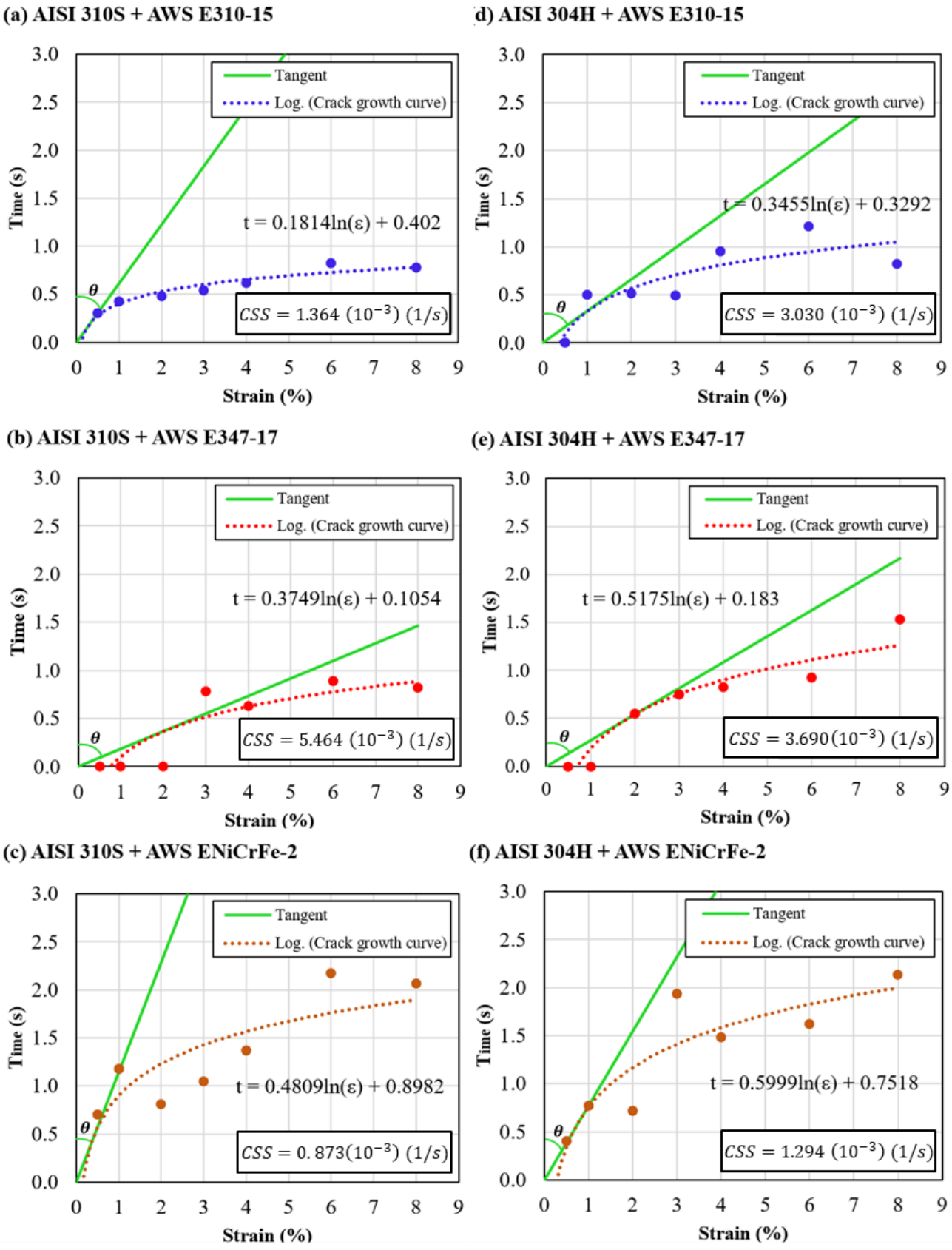

Source: elaborated by the author.

Table 12 presents the chemical composition of the fusion zones of the welds studied in this work, as determined by XRF, EDS, and OES. The results indicate any significant differences among the three methods. However, OES enabled the determination of the content of more elements.

Table 12 — Chemical composition of the fusion zones

Technique	Base Metal	Filler Metal	Fe	Cr	Ni	Mn	Mo	Nb	V	Cu	Ti	Si	Co	W	Ta	Hf	C
XRF	AISI 310S	AWS E310-15	52.1	25.6	20.5	1.7	0.06	0.01	0.01								
		AWS E347-17	62.6	22.1	13.2	1.0	0.12	0.39	0.11				0.32				
		AWS ENiCrFe-2	31.6	21.3	42.7	2.0	1.02	1.31			0.033						
	AISI 304H	AWS E310-15	56.7	23.2	16.5	1.7	0.68		0.08		0.222	0.70					
		AWS E347-17	69.8	19.9	9.1	0.6	0.16	0.28									
		AWS ENiCrFe-2	35.7	17.5	42.4	2.0	1.15	1.16									
EDS	AISI 310S	AWS E310-15	50.7	26.6	19.6	2.1						0.40					
		AWS E347-17	62.1	22.2	12.5	1.5		0.30		0.30		1.00					
		AWS ENiCrFe-2	30.1	21.4	42.5	2.4	1.00	1.40		0.20		0.80					
	AISI 304H	AWS E310-15	56.6	24.1	16.0	2.1						0.40					
		AWS E347-17	68.4	20.2	8.7	1.2		0.20		0.20		0.90					
		AWS ENiCrFe-2	34.1	17.6	41.2	2.4	1.60	1.80		0.40		0.60					
OES	AISI 310S	AWS E310-15	51.82	25.84	19.27	1.87	0.03	0.01	0.07	0.08	0.014	0.29	0.22	0.32			0.101
		AWS E347-17	62.72	21.47	12.87	1.16	0.10	0.10	0.06	0.06	0.020	0.88	0.22	0.25			0.041
		AWS ENiCrFe-2	31.85	19.55	43.18	1.80	1.18	0.88	0.04	0.04	0.012	0.69	0.17	0.12	0.28	0.12	0.052
	AISI 304H	AWS E310-15	58.43	22.69	15.93	1.88	0.07	0.02	0.05	0.09	0.013	0.27	0.10	0.30			0.092
		AWS E347-17	69.18	19.18	8.84	0.93	0.15	0.36	0.06	0.09	0.020	0.70	0.16	0.22			0.042
		AWS ENiCrFe-2	36.78	16.29	41.56	1.80	1.30	0.93	0.03	0.07	0.015	0.51	0.10	0.11	0.32	0.10	0.056

Source: elaborated by the author.

Table 13 — Contaminant content for each combination of base and filler metal

Base Metal	Filler Metal	C	N	P	S
AISI 310S	AWS E310-15	0,101	0,026	0,031	0,005
	AWS E347-17	0,041	0,027	0,018	0,006
	AWS ENiCrFe-2	0,052	0,01	0,018	0,006
AISI 304H	AWS E310-15	0,092	0,03	0,03	0,004
	AWS E347-17	0,042	0,028	0,033	0,008
	AWS ENiCrFe-2	0,056	0,073	0,019	0,005

Source: elaborated by the author.

The OES data was utilised to determine the dilution level of the weld metal following Equation 24. Figure 40 shows the dilution calculated based on the Fe content of the base metals, filler metals, and fusion zones. It can be seen that AISI 310S tended to mix more with the filler metals. Furthermore, the substantial groove area of the specimens led to quite high dilution levels.

Figure 40 — Dilution level of each weld metal determined according to the chemical composition

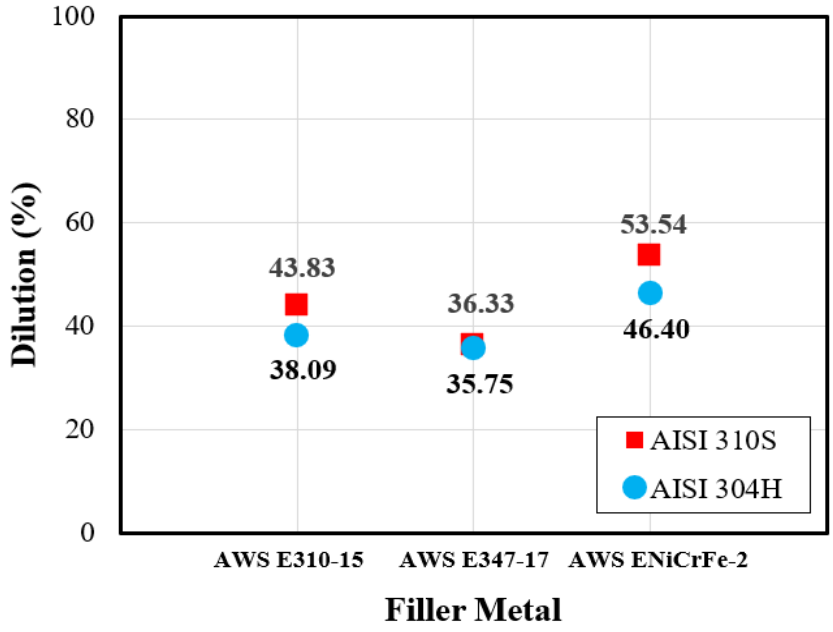

Source: elaborated by the author.

The data presented in Table 12 were utilised to calculate the chromium equivalent and nickel equivalent ratio for each tested combination of base and filler metal. By comparing the ratios obtained here to those in Table 6, the solidification modes of the austenitic stainless

steel weld metals were estimated. The results are shown in Table 14. The fusion zones were expected to solidify in fully austenitic (A) mode for the welds of both base metals with the AWS E310-15 electrode. The chemical composition of the welds with the AWS E347-17 electrode as the filler metal indicated solidification in the primary ferrite/secondary austenite (FA) mode.

There was a notable difference in the prediction of solidification modes using Schaeffler's and WRC-1992 equations. For the weld of AISI 310S with the AWS E347-17 electrode, Schaeffler's equations indicated a Cr_{eq}/Ni_{eq} associated with the FA mode. In contrast, the equations used to develop the WRC-1992 indicated a primary austenite/secondary ferrite (AF) mode.

Table 14 — Solidification modes determined according to Cr_{eq}/Ni_{eq}

Base metal	Filler metal	Schaeffler				WRC-1992			
		Cr_{eq}	Ni_{eq}	Cr_{eq}/Ni_{eq}	Mode	Cr_{eq}	Ni_{eq}	Cr_{eq}/Ni_{eq}	Mode
AISI 310S	AWS E310-15	26.31	23.24	1.13	A	25.88	23.35	1.11	A
	AWS E347-17	22.94	14.68	1.56	FA	21.64	14.85	1.46	AF
AISI 304H	AWS E310-15	23.18	19.63	1.18	A	22.77	19.77	1.15	A
	AWS E347-17	20.56	10.57	1.95	FA	19.58	10.89	1.80	FA

Source: elaborated by the author.

Figure 41 presents the Scheil–Gulliver curves resulting from the thermodynamic simulation of each weld metal composition analysed. The graphics also exhibit the curve for equilibrium solidification (red dashed line), i.e., considering a low cooling rate.

The simulation corresponding to the AISI 310S and AWS E310-15 combination showed that austenite (γ) is expected to be the primary phase formed during cooling. The solidification route was as follows: $L \rightarrow L + \gamma \rightarrow L + \gamma + \delta\text{-ferrite} \rightarrow L + \gamma + \delta\text{-ferrite} + carbonitride \rightarrow L + \gamma + \delta\text{-ferrite} + carbonitride + MnS \rightarrow L + \gamma + \delta\text{-ferrite} + carbonitride + M_{23}C_6 + MnS$. The composition of the carbonitride was predicted to be rich in titanium and niobium. In addition, the carbide $M_{23}C_6$ was indicated to be mostly $Cr_{23}C_6$. The simulated solidification route of the weld metal resulting from the dilution of the AWS E310-15 electrode with AISI 304H was very similar, except for the absence of $M_{23}C_6$. It was: $L \rightarrow L + \gamma \rightarrow L + \gamma + \delta\text{-ferrite} \rightarrow L + \gamma + \delta\text{-ferrite} + carbonitride \rightarrow L + \gamma + \delta\text{-ferrite} + carbonitride + MnS$. The estimation of the phase composition also suggested that this carbonitride was Ti- and Nb-rich.

The δ-ferrite is predicted as the first solidified phase for welds with the AWS E347-17 electrode. According to the simulations, its combination with both base metals has identical solidification routes: $L + \delta\text{-ferrite} \rightarrow L + \delta\text{-ferrite} + \gamma \rightarrow L + \delta\text{-ferrite} + \gamma + carbonitride \rightarrow L + \delta\text{-ferrite} + \gamma + carbonitride + MnS$. In these cases, the carbonitride was again expected to

be mainly composed of Nb and Ti.

Welding of AISI 310S and AWS ENiCrFe-2 is indicated to lead to the following solidification route: $L \rightarrow L + \gamma\text{-}Ni \rightarrow L + \gamma\text{-}Ni + carbonitride\ 1 \rightarrow L + \gamma\text{-}Ni + carbonitride\ 1 + carbonitride\ 2$. These two types of carbonitrides were considered identical, and the simulation indicated that both are rich in Nb, Ta, and Hf. The weld of this electrode with AISI 304H exhibited analogous solidification behaviour, with the exception of not forming carbonitride 2.

Figure 41 — Scheil–Gulliver solidification curves

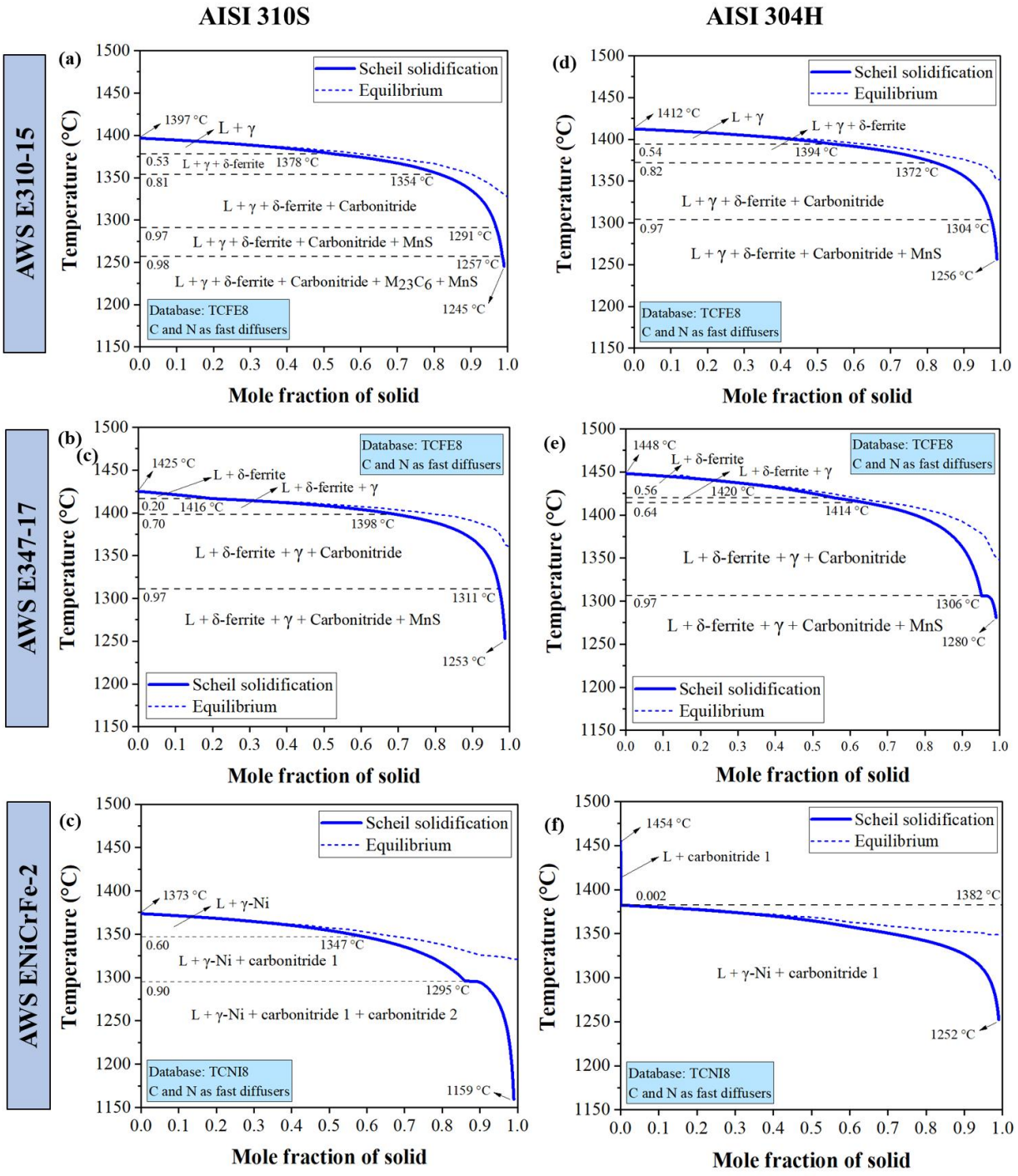

Source: elaborated by the author.

The molar fraction of each phase at the end of the solidification process estimated by thermodynamic simulation is shown in Table 15.

Table 15 — Weld metal phase composition at the end of the solidification stage according to thermodynamic simulation

Filler metal	Phase	Base Metal	
		AISI 310S	AISI 304H
		Mole fraction	Mole fraction
AWS E310-15	Austenite (γ)	0.85	0.85
	δ-ferrite	0.14	0.14
	Carbonitride	0.0002	0.0002
	$M_{23}C_6$	0.0009	
	MnS	0.0001	0.0001
AWS E347-17	δ-ferrite	0.59	0.66
	Austenite (γ)	0.40	0.33
	Carbonitride	0.0003	0.003
	MnS	0.0001	0.0002
AWS ENiCrFe-2	γ-Ni	0.99	0.99
	Carbonitride 1	0.0006	0.008
	Carbonitride 2	0.005	

Source: elaborated by the author.

The temperatures at the beginning ($T_{liquidus}$) and at the end ($T_{solidus}$) of solidification were estimated based on the Scheil–Gulliver diagram data. The solidification ranges (ΔT_{sol}) were calculated subtracting $T_{liquidus}$ and $T_{solidus}$ from the fusion zones. Figure 42 shows the results. For both base metals, the weld with the AWS ENiCrFe-2 electrode presented the highest values of ΔT_{sol}, followed by the weld metal resulting from the deposition of the AWS E347-17 electrode.

Figure 42 — Fusion zone solidification range according to thermodynamic simulations for combinations with (a) AISI 310S and (b) AISI 304H as the base metal

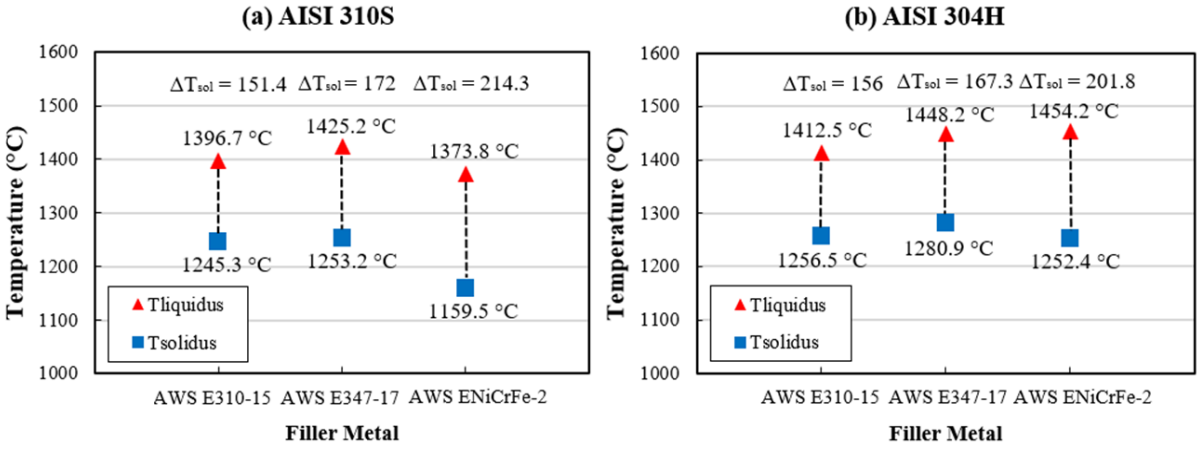

Source: elaborated by the author.

Figure 43 contains the BTR values calculated through thermodynamic simulation data for all weld metals. The fusion zone resulting from the AWS ENiCrFe-2 and AISI 310S welds had a BTR of 156.4 °C, which is 21.6 °C higher than the second greatest value of 134.8 °C

and corresponds to the welding of the AWS E347-17 electrode with AISI 310S.

Figure 43 — Brittle temperature ranges determined using thermodynamic simulation data

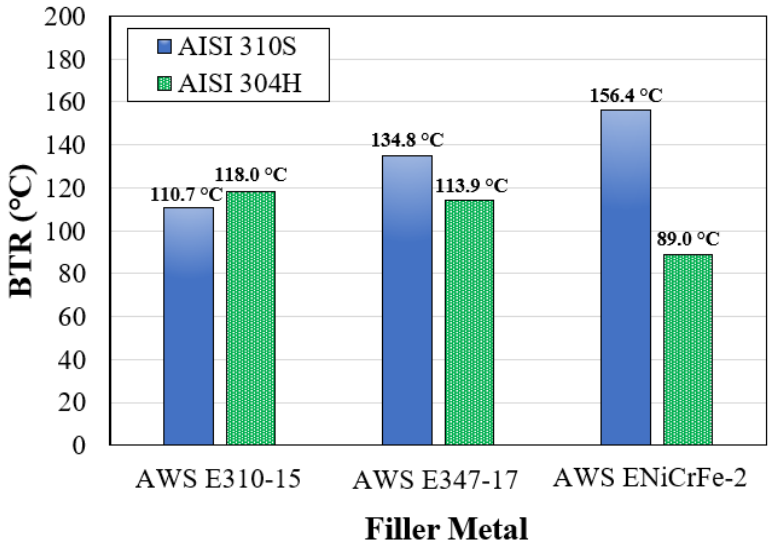

Source: elaborated by the author.

The cooling curves obtained from DTA are presented in Figure 44. The $T_{liquidus}$, $T_{solidus}$, and ΔT_{sol} are identified in the graphs. The $T_{liquidus}$ corresponded to the temperature at the beginning of the solidification event (at the first point that constituted the peak, when the curve changed from the baseline). Similarly, $T_{solidus}$ was considered the temperature at the end of the solidification event. The thermodynamic simulation data, specifically the formation temperature of each phase, was utilised to interpret the DTA graphs.

For the welds with the AWS E310-15 electrode (Figure 44a and Figure 44d), only one peak was detected during solidification, which corresponded to the formation of the austenite phase. The weld of AISI 310S with AWS E347-17 (Figure 44b) exhibited one peak at 1415.7 °C. However, this prominent peak appeared to suppress another peak at 1423.6 °C. Hence, this event was understood as the formation of primary δ-ferrite and secondary austenite during cooling. This behaviour was also observed for the AISI 304H and AWS E347-17 welds (Figure 44e), but for this sample, the existence of two peaks (1448.1 °C and 1416.7 °C) was more evident.

Figure 44c shows the DTA cooling curves of the AISI 310S and AWS ENiCrFe-2 welds. The peak at 1359.3 °C was attributed to the formation of the γ-fcc phase of nickel (γ-Ni). In turn, the peak at 1294.7 °C is believed to be related to the precipitation of carbonitrides. The analysis of the AISI 304H sample weld with AWS ENiCrFe-2 revealed three peaks that occurred during the solidification event. The first two peaks (at 1458.4 °C and 1370.6 °C) were

attributed to the formation of γ-Ni and carbonitrides. Nevertheless, the third peak (1308 °C) near the end of solidification, which is not very pronounced, does not match any phase predicted by thermodynamic simulation.

Figure 44 — DTA cooling curves

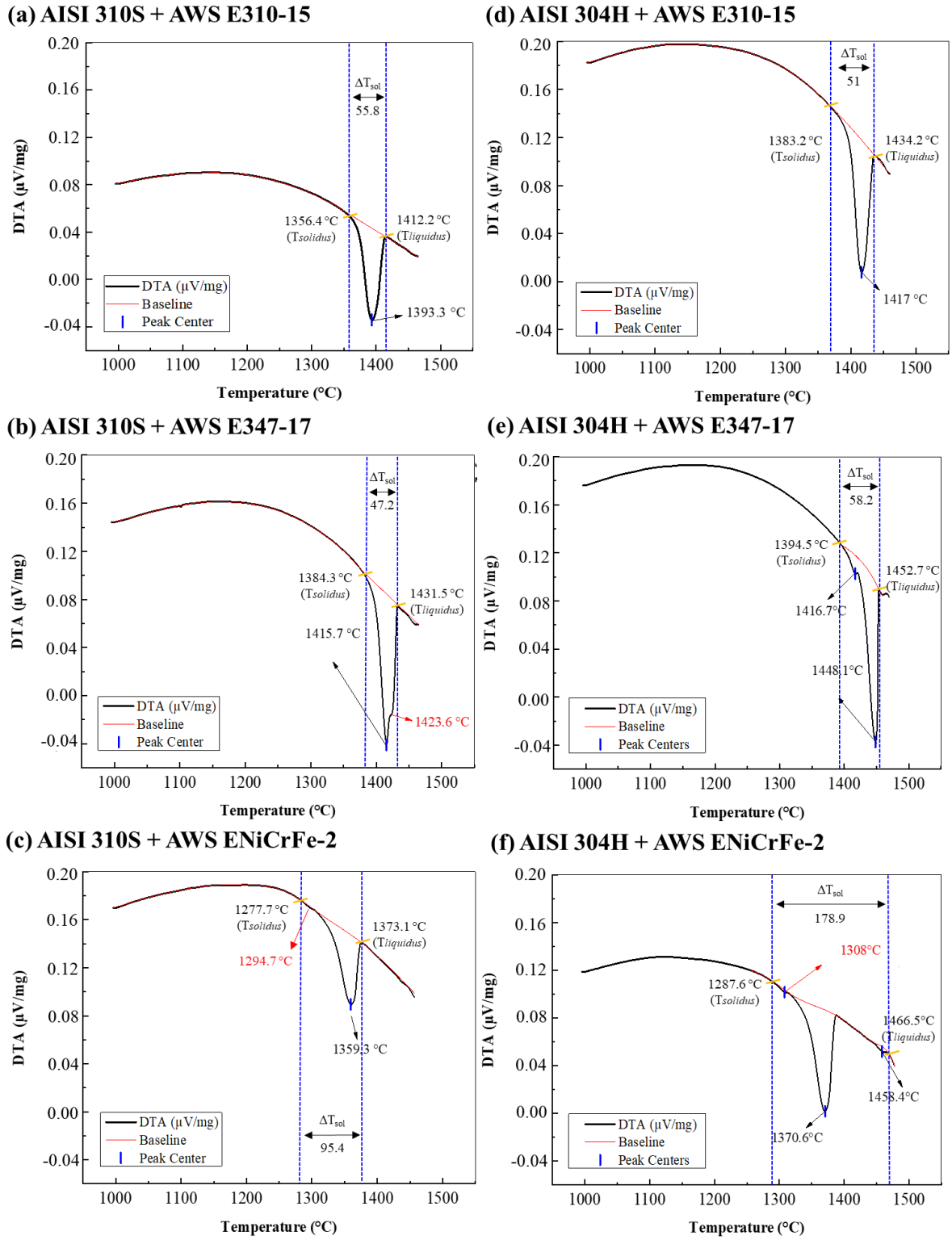

Source: elaborated by the author.

Figure 45 shows an example of the integration of the DTA curve for the estimation of the BTR.

Figure 45 — Integration of the DTA curve resulting from the welding of AISI 310S with AWS E347-17 electrode

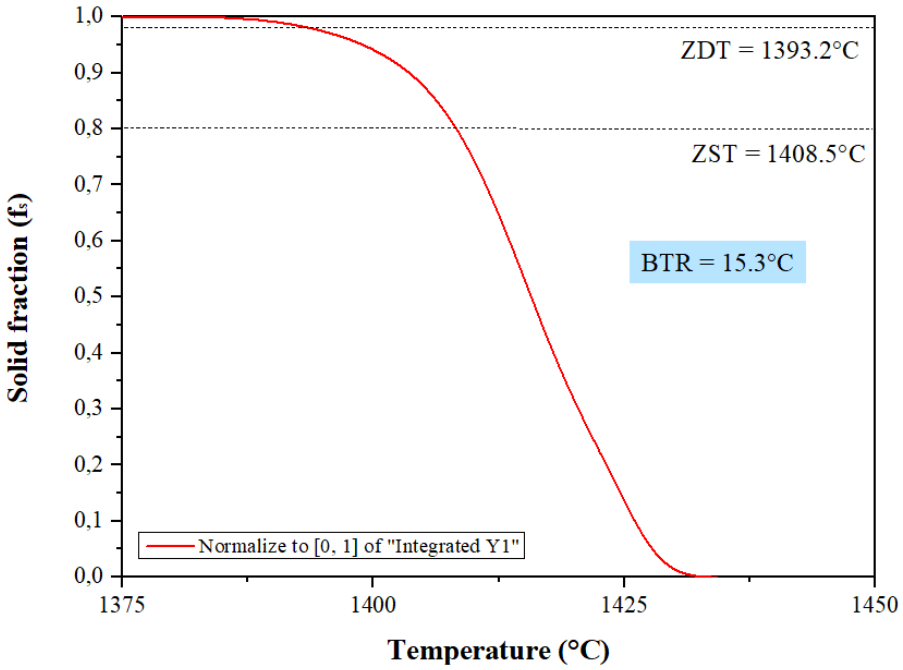

Source: elaborated by the author.

The BTR values obtained through DTA are shown in Figure 46 for a direct comparison with the BTR values calculated via thermodynamic simulation data presented in Figure 43.

Figure 46 — BTR values determined through DTA data

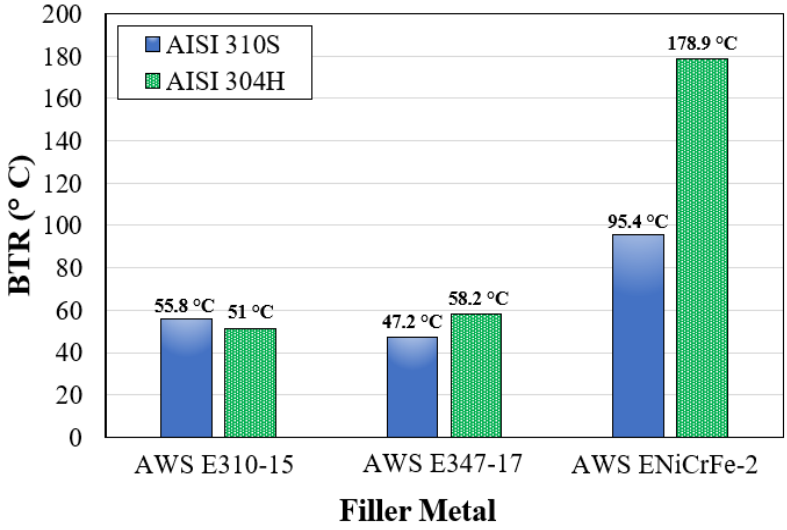

Source: elaborated by the author.

Table 16 also compares the BTRs calculated based on thermodynamic simulation to the values obtained using DTA data. All BTR values indicated by the DTA are lower than those from the thermodynamic simulation.

Table 16 — Comparison between the solidification range and brittle temperature range obtained by thermodynamic simulation and differential thermal analysis

Base metal	Filler metal	Thermodynamic simulation		DTA	
		Solidification range	BTR	Solidification range	BTR
AISI 310S	AWS E310-15	151.4	110.7	38.3	13.7
	AWS E347-17	172.0	134.8	47.2	15.3
	AWS ENiCrFe-2	214.3	156.4	88.4	53.6
AISI 304H	AWS E310-15	156.0	117.0	51.0	11.7
	AWS E347-17	167.3	113.9	54.2	23.8
	AWS ENiCrFe-2	201.9	89.0	178.9	44.0

Source: elaborated by the author.

The microstructures of the fusion zones are shown in Figure 47. The LOM analysis allowed the identification of inclusions distributed along all the fusion zones, which are indicated by the red arrows.

The welds with the AWS E310-15 electrode (Figure 47a,d) were confirmed to solidify in the A mode, with a columnar dendritic morphology. The welds with the AWS E347-17 electrode solidified in FA mode, resulting in a duplex microstructure of ferrite and austenite; the core of the dendrites (darker regions) is δ-ferrite, which is surrounded by an austenite phase. The fusion zone of the welds of AISI 310S and AWS E347-17 has δ-ferrite with a vermicular morphology (Figure 47b). In turn, the weld of this electrode with AISI 304H (Figure 47e) has both vermicular and lacy δ-ferrite.

Columnar dendrites were also included in the morphology for the combination utilising AWS ENiCrFe-2 as the filler metal (Figure 47c,f). In addition to the γ-Ni phase, etching revealed tiny particles that precipitated on the interdendritic regions, as indicated by the yellow arrows.

Figure 47 — Light optical micrographs of the fusion zones at 100× and 500× magnifications

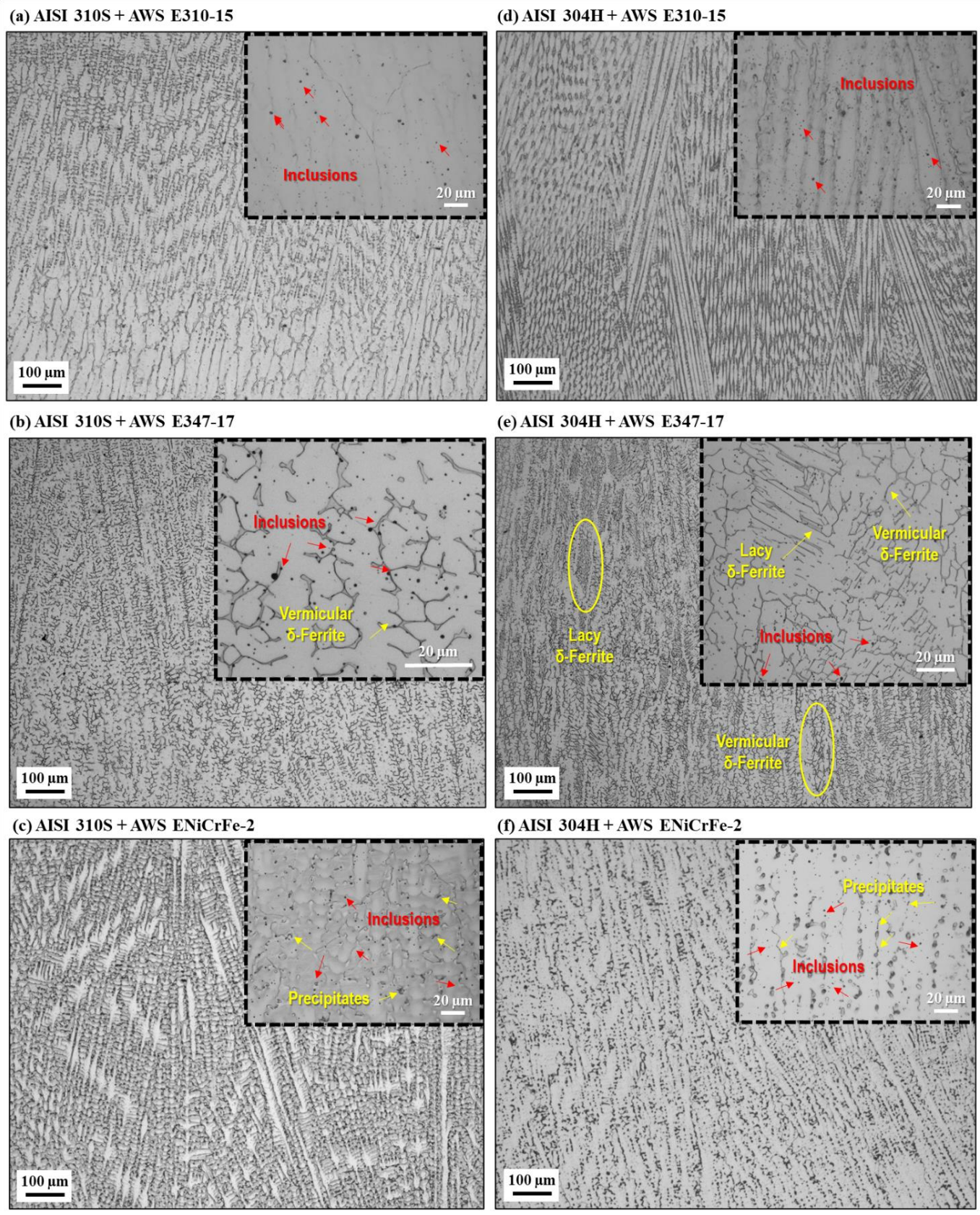

Source: elaborated by the author.

3.5 Discussion

Lippold and Kotecki (2005) review the basic concepts associated with hot cracks and outline methods to quantify the susceptibility of these types of cracking. The authors confirmed that (1) the critical strain of most fully austenitic stainless steel weld metals and Ni-base alloys ranges between 0.5% and 2.0%, and (2) the saturated strain of these alloys is within the range of 5.0 to 7.0%. As shown in Table 9, the first affirmation is in agreement with the majority of results obtained in the present work. The only condition for which this was not true is the welding of AISI 310S with AWS E347-17, which presented an ε_{cr} higher than 2% and less than or equal to 3%. The second statement was also confirmed here. However, when assessing the saturated strains, it is essential to note that in some cases the interpretations of the MCD and TCL curves *versus* augmented strain led to different ranges ε_{st} ranges. Any reliable elucidation of the cause of this discrepancy would necessitate additional tests conducted under identical conditions, which would likely lead to the alignment of these curves and facilitate more consistent estimates.

According to the critical strain, saturated strain, and crack measurements, the welds with AWS ENiCrFe-2 electrode were the most susceptible to solidification cracking among the combinations tested. In turn, the welds with the AWS E347-17 electrode presented the highest resistance to solidification cracking. The evaluation of the critical strain rate to time required to cause cracking (CSS) corroborated with the conclusion obtained by analysing other variables. The TVT of the weld bead deposited by AWS ENiCrFe-2 in both base metal specimens resulted in the lowest CSS values, indicating that only a small strain is needed to initiate solidification cracks under the tested conditions. Conversely, the tests with AWS E347-17 produced the highest CSS values.

The analysis of the chemical composition of the fusion zone contributed to several observations. For tests utilising the AWS E310-15 electrode, the weld metal composition caused the solidification in the A mode, implying a fully austenitic microstructure, as shown in Figure 47a and Figure 47d. Nonetheless, in tests using the filler metal AWS E347-17, the weld metal solidified in FA mode (Figure 47b and Figure 47e). This occurred because the welds with AWS E347-17 had lower contents of austenitising elements, such as Ni, Mn, and C (Table 12). The retention of δ-ferrite was determined by the segregation patterns of Cr and Ni after solidification in austenitic stainless steel welds, which are very intense, and by the rapid cooling rates reached during welding, which prevent the diffusion of these major alloy elements (Shankar et al., 2003).

The ANOVA results (Figure 38) showed a statistically significant difference between the test results for the three filler metals. The TVT results presented in Table 9 and Table 10 can be understood by analysing the chemical composition of the fusion zones formed from the dilution of each electrode with both base metals.

The TVT results can be understood by analysing the chemical composition of the fusion zones. Impurities and minor elements originating from the base or filler metal segregate towards the liquid, changing its chemistry locally as solidification progresses. Segregation significantly influences the cracking susceptibility of austenitic stainless steel (Aucott et al., 2018). Impurities such as P, S, and N tend to accumulate in intercellular or interdendritic volumes with solute elements (e.g., Mn, Si, and Al), forming low-melting-point liquid pockets or films that serve as crack nucleation sites (Brooks, Thompson, 1991; Arata et al., 1978). The solubility of the impurities in austenite is low, which may cause the primary solidifying austenite to reject the boundaries, where they gather and tend to form eutectic or peritectic liquids with low melting points, such as Ti and Nb. Furthermore, austenite/austenite boundaries are smoother pathways that facilitate crack growth (Arata et al., 1976; Arata et al., 1977; Brooks, Thompson, 1991; Kujanpää, 1985; Shankar et al., 2003; Saida et al., 2012).

The presence of some δ-ferrite in welds using AWS E347-17 helps improve weldability. Arata, Matsuda, and Saruwatari (1974) demonstrated that microstructures with δ-ferrite are less susceptible to solidification cracking than those without ferrite. Several authors have discussed the reasons for the favourable effect of ferrite on ASS welds. Based on their conclusions, the most plausible reasons are as follows: (i) the solubility of impurity elements is notably greater in δ-ferrite than in austenite, leading to less microsegregation; (ii) the fact that the ferrite/austenite boundaries are not wetted by liquid films such as ferrite/ferrite and austenite/austenite boundaries; thus, forming fissures during the last stages of solidification is more difficult; and (iii) the morphology of the ferrite/austenite boundaries, which are irregular paths for crack propagation (Brooks, Thompson, 1991; Kujanpää, 1985; Arata, Matsuda, Saruwatari, 1974; Lundin, Chou, Sullivan, 1980).

Kujanpää et al. (1970) tested several materials and developed an empirical diagram to correlate impurities' content to the susceptibility of austenitic stainless steels to solidification cracking. Reproduced in Figure 10, this diagram is divided into two regions, “cracking” and “no cracking”, based on the tendency to form solidification cracks. The placement corresponding to each austenitic stainless steel weld metal analysed in this work is indicated, considering the values of Cr_{eq}/Ni_{eq} and (P+S) content. The fusion zones originating in the welds with AWS E310-15 are located on the left side of the graphic in the “cracking” region. In turn,

the weld metal of the welds with AWS E347-17 electrode is placed on the right side ("no cracking" region).

Figure 48 — Relationship of chemical composition, in terms of impurity content and chromium and nickel equivalent ratio, to the solidification cracking susceptibility of austenitic stainless steel weld metals

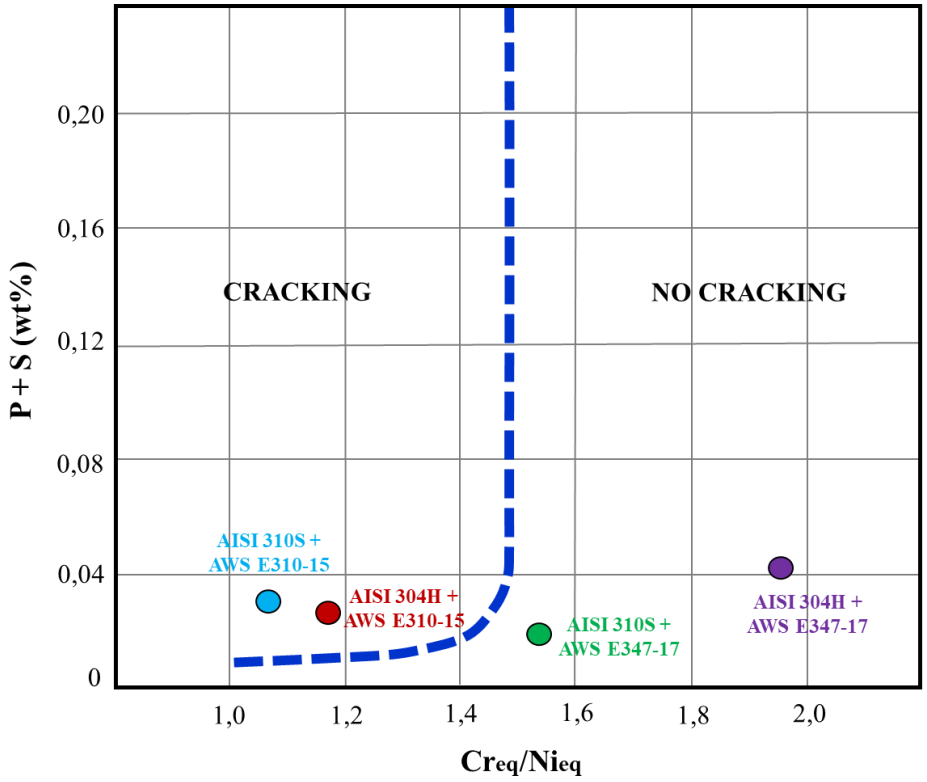

Source: Kujanpää et al. (1979), adapted.

The lower resistance to solidification cracking of welds with AWS ENiCrFe-2 electrode may be due to the precipitation of secondary phases. Microstructural observation revealed the presence of precipitates in the fusion zone. According to works that investigated the weldability of nickel alloys, the low resistance to solidification cracking of their fusion zones can be related to the formation of a Nb-rich brittle phase in interdendritic regions during weld metal solidification (Caironi et al., 1993; Belloni et al., 2001; Naffakh, Shamanian, Ashrafizadeha, 2009; Kuo, Lee, Tu, 2003).

The formation of inclusions on the fusion zones was attributed to the SMAW process, in which the slag-metal reactions involve the oxidation of alloy elements, which originate from oxides that may be trapped in the weld metal as solidification advances (Kou, 2003).

The DTA did not detect the formation of all phases predicted by the thermodynamic

simulation. For example, the formation of $M_{23}C_6$, a critical carbide formed in austenitic stainless steels, was not confirmed in the welds with the AWS E310-15 electrode. This can be explained by the fact that for these materials, the precipitation of $M_{23}C_6$ is not common during rapid cooling and usually occurs after exposure at high temperatures for some time (Kaneko et al., 2011). Another example of this is the precipitation of MnS, which is theoretically expected in all austenitic stainless steel weld metals. This may occur because Mn tends to combine with S at the end of the solidification process (Brooks, Thompson, 1991). Saida et al. (2013) showed that granular inclusions containing Mn and S were observed at the cell boundaries of a commercial type 310 weld metal. However, no evidence of MnS was detected through DTA, which led to a considerable decrease in the solidification range. Additionally, the investigation of the fusion zones using DTA did not reveal the presence of carbonitrides in the ASS weld metals. This also decreased the ΔT_{sol}.

Otherwise, the thermal analysis results agreed with the microstructural observations. Considering this, the values of BTR calculated via DTA data appeared to be more coherent. This was expected, especially because DTA is an empirical experiment and may be more accurate than thermodynamic simulation.

The susceptibility to hot cracking can be qualitatively related to ΔT_{sol} and to the BTR. Materials with a high BTR remain in the critical stages of solidification for a longer period than those with a low BTR. Consequently, they are subjected to more contraction stresses due to thermal constraints, making them more prone to cracking (Santillana et al., 2012; Aucott et al., 2018). However, even considering the calculations through DTA data, the BTR values of the tests with the AWS E347-17 electrode were greater than those verified for the tests with the AWS E310-15 electrode. This finding diverges from the TVT results, which show that the combination of AWS E347-17 with both base metals is the most resistant to solidification cracking. Therefore, it is believed that the microstructural aspects of the welds with AWS E347-17 play a major role. Even so, these weld metals are less susceptible to solidification cracking after spending more time in the last stages of solidification, due to their chemical composition which allows the formation of δ-ferrite.

Based on the results, it was possible to assess the susceptibility to solidification cracking of all tested combinations. Here, the dilution levels reached nearly the upper limit for the welding method used, meaning that, in practice, the fusion zone often contains less amount of base metal. Therefore, it can be concluded that the high dilution levels indicate that the cracking behaviour observed in this work for the six combinations of base and filler metals is very representative and allowed the assessment of the fusion zones under critical conditions.

The Trans-Varestraint test consists of submitting the fusion zone to a critical condition during solidification by applying high external stress, which favours the occurrence of solidification cracks. In the welding process, this stress level is generally not reached during weld metal cooling. Hence, it is necessary to note that the weld metals that presented cracks after the tests performed in this study did not necessarily crack during a typical welding procedure. However, as TVT reflects the tendency for solidification cracking, it can be affirmed that weld metal compositions resulting from the deposition of the AWS ENiCrFe-2 and AWS E310-15 electrodes with both base metals are more likely to fail than those resulting from the deposition of AWS E347-17. Consequently, the employment of welds with similar compositions should be avoided or well-controlled, aiming to prevent premature failures.

The finding clearly indicates that the weld metals produced by diluting both base metals with AWS E347-17 electrode exhibited markedly enhanced resistance to solidification cracking when compared to other welding combinations tested. However, it is crucial to consider how variations in experimental setups may have impacted the analysis of this study. To accurately compare the susceptibility of different materials to solidification cracking using Trans-Varestraint test, it is imperative that all tests are conducted under similar conditions. Kromm et al. (2022) emphasise that crack lengths are not solely a function of materials properties but are also affected by the specific parameters of the applied tests. Consequently, direct comparisons of crack lengths across distinct conditions are not valid.

In the present study, we differentiated the welding tests conducted with AWS E347-17 from those using AWS E310-15 and AWS ENiCrFe-2 fillers. Each welding parameter was tailored to optimised the characteristics of the weld beads for the respective base and filler metal combinations. A modified Trans-Varestraint test was conducted using these optimised parameters. The heat input for welds utilising AWS E310-15 and AWS ENiCrFe-2 electrodes ranged between 1.09 and 1.12 kJ/mm, with the slight variation attributed to the manual welding technique employed. Conversely, the welds using AWS E347-17 exhibited a markedly higher heat input. This discrepancy in heat input is likely to have affected the crack measurements obtained.

In the experiments conducted with AISI 310S and AISI 304H specimens using the AWS E347-17 electrode, the heat inputs recorded were 1.62 and 1.54 kJ/mm, respectively. These differences in heat input can be attributed to slight variations in welding speed and current settings; specifically, the AWS E347-17 welding was performed at a lower welding speed and higher current, thereby increasing the heat input. The higher heat input leads to a reduced cooling rate, allowing for a prolonged solidification time of the weld metal, which

promotes the microsegregation of impurity elements. This microsegregation is a significant contributor to solidification cracking. Furthermore, the increased temperature gradient associated with greater heat input is likely to result in the formation of larger cracks in the welds.

The analysis indicated that had the Trans-Varestraint tests using AWS E347-17 been executed under the same heat input conditions as those applied in the tests with AWS E310-15 and AWS ENiCrFe-2 electrodes, the observed crack lengths would likely have been further minimised. This underscores the exceptional resistance to solidification cracking exhibited by the fusion zones resulting from the dilution effects of AISI 310S and AISI 304H with the AWS E347-17 filler metal.

Further in-depth microstructural analysis through advanced techniques is scheduled to enhance the characterisation of these weld metals. There is a need to investigate the presence of precipitates and other features that more effectively correlate the morphology, cristallography and composition of the phases with the weldability of the weld metal. These analyses are crucial and compounds an upcoming study by the authors, aimed at a thorough examination of the microstructure.

3.6 Conclusion

This work contributes to understanding the metallurgical aspects associated with solidification cracking of corrosion-resistant alloy weld metals for high-temperature applications. The weldability of three electrode candidates for application in manufacturing flare′s components was successfully assessed through the Trans-Varestraint test in terms of the susceptibility to solidification cracking, considering as parameters the critical and saturated strains, the critical strain speed, and the solidification mode. Based on the results obtained, the following conclusions were drawn:

I) The ranking from least to most susceptible to the solidification cracking weld combination is as follows: (AISI 310S + AWS E347-17) > (AISI 304H + AWS E347-17) > (AISI 304H + AWS E310-15) > (AISI 310S + AWS E310-15) > (AISI 304H + AWS ENiCrFe-2) > (AISI 310S + AWS ENiCrFe-2).

II) The welds with AWS E347-17 electrode exhibited the highest critical strain among the welds evaluated. The AISI 310S test developed cracks at a strain of 3%, whereas its combination with AISI 304H showed cracks at a strain of 2%. Furthermore, the weld metal produced from the deposition of this electrode with

both base metals had the lowest variation in crack lengths with increasing strain, resulting in the lowest saturated strain.

III) The tests of welds with AWS E310-15 and AWS ENiCrFe-2 filler metals showed a considerably lower critical strain than those with AWS E347-17 electrode. The weld metals resulting from the dilution of AWS E310-15 and AWS ENiCrFe-2 electrodes with the base metals also exhibited the highest saturated strain. They showed significant variation in crack lengths with increasing strain. The TVT tests of welds with AWS ENiCrFe-2 resulted in larger cracks.

IV) The tests of AISI 310S and AISI 304H specimens with AWS E347-17 led to the highest CSS values, 5.464×10^{-3} (1/s) and 3.690×10^{-3} (1/s), respectively, indicating a greater resistance to solidification cracking. In turn, the tests of AISI 310S and AISI 304H specimens with AWS ENiCrFe-2 presented the lowest CSS values, 0.873×10^{-3} (1/s) and 1.294×10^{-3} (1/s), then the required strain level applied in a certain time to start cracking is the smallest between the other conditions tested.

V) The fusion zones of the tests with the AWS E310-15 electrode solidified in the A mode, resulting in a fully austenitic microstructure that is favourable for cracking. The solidification of the welds resulting from the dilution of AWS E347-17 with both base metals remained in FA mode, which is beneficial for preventing solidification cracking.

VI) The fusion zones in the tests using the AWS ENiCrFe-2 filler metal consisted of the γ-Ni fcc phase. Their microstructure also showed evidence of secondary phase precipitates. The presence of these secondary phases may influence the cracking tendency, helping to explain the lower resistance to solidification cracking.

4 ORIENTATION IMAGING AND MICROCHEMISTRY ANALYSIS OF DISSIMILAR METAL WELDS OF CORROSION-RESISTANT ALLOY UNDER TRANS-VARESTRAINT TESTING

4.1 Abstract

Austenitic stainless steel (ASSs) and nickel-based alloys are employed in applications that require high-temperature and corrosive environments. The fabrication of equipment often involves welding procedures. However, welding these materials can cause solidification cracking, which is one of the main concerns for preventing the premature failure of components. The present work is a comprehensive study that aimed to understand the behaviour of dissimilar corrosion-resistant weld metals subjected to external stress during the Trans-Varestraint test. It was conducted a detailed microstructural characterisation of the samples using advanced techniques such as light optical microscopy and scanning electron microscopy, including energy dispersive X-ray spectroscopy (EDS) and electron backscatter diffraction (EBSD). The fusion zones resulting from the dilution of AWS E310-15 with both base metals had a completely austenitic microstructure. The fusion zones of the samples from the welds produced with the AWS E347-17 electrode solidified in the primary ferrite/secondary austenite mode, thus containing some δ-ferrite. The welds with AWS ENiCrFe-2 were mainly composed of the γ-Ni phase and the formation of Nb(C,N) precipitates in interdendritic volumes was very notable. The EBSD results showed higher misorientation levels surrounding the cracks and sub-grain boundaries.

Keywords: austenitic stainless steel; dissimilar welding; solidification cracking; Trans-Varestraint Test; microstructural characterisation; EBSD.

4.2 Introduction

Austenitic stainless steel (ASSs) and nickel-based alloys are employed in applications that require high-temperature and corrosive environments. They are frequently utilised for manufacturing equipment in the nuclear, chemical, petrochemical, and oil and gas industries and are recognised for having high strength and creep resistance at high temperatures and corrosion resistance in harsh atmospheres (Kolts, 1989; Dupont, 1996; Rashmi, Bhavsar, 2001; Mcloughlin et al., 2005; Abou-Elazm et al., 2009; Pardal et al., 2011; Yousefi, Farghadin, Fazardi, 2015; Ghalambaz et al., 2017; Mahdi, Esmaeili, 2020; Jiang et al., 2023).

The fabrication of components often involves welding procedures, such as gas tungsten arc welding (GTAW) or shielded metal arc welding (SMAW). However, the welding of ASSs and nickel-based alloys presents a significant challenge due to the high cooling rates achieved, which cause nonequilibrium solidification, microsegregation, and potential rejection of impurities from the solid toward the interdendritic liquid (Katayama, Fujimoto, Matsunaga, 1985). These factors are crucial for the occurrence of solidification cracking, a major concern for preventing premature failures related to welding. The need for research in this area is underscored by the potential impact on preventing premature failures in critical applications.

Solidification cracking, a common issue in welding, can occur in the fusion zones of welds as a result of the formation of low-melting-point eutectic films, mainly composed of impurities and other segregated elements, in the interdendritic regions at the final critical stages of solidification. The nucleation mechanism of a solidification cracking is related to the rupture of these thin liquids, which act as crack nucleation sites under external stress, solidification shrinkage and/or constriction. The propagation proceeds with subsequent coalescence of the intergranular liquid (Aucott et al., 2018; Liu et al., 2023).

The weldability of materials is directly associated with solidification cracking susceptibility (Dupont, Lippold, Kiser, 2009). Several weldability tests were used to assess the solidification cracking resistance. The Trans-Varestraint test, a widely utilised method, is an augmented restraint weldability test in which an external load is applied during welding to induce weld pool deformation. The material is forced to bend downwards following a matrix radius, and the bending plane is perpendicular to the weld direction, restricting crack formation to the fusion zone (Senda et al., 1971; Arata, Matsuda, 1976; Matsuda, Arata, Katayama, 1977; Arata et al.; 1977). This test is particularly significant in the present study as it allows us to observe the effects of stress on the microstructure of dissimilar corrosion-resistant weld metals, providing crucial insights into the behaviour of these materials under strain during cooling.

The results of TVT examination often focus only on crack measurements (ISO TR 17641-3, 2005; Dupont, Lippold, Kiser, 2005; Statharas et al., 2019). However, meaningful information on the behaviour of weld metals that undergo strain during cooling may be obtained when analysing the microstructural changes provoked by the external stress applied in the tests. Hence, microstructural characterisation techniques are fundamental tools for determining the solidification cracking susceptibility of materials.

Electron backscatter diffraction (EBSD), for example, can be employed to quantify deformation, once the deformation of crystal lattices affects its patterns (Wright, Nowell, Field, 2011). EBSD technique is widely applied to assess plastic deformation and can detect the effects

of dislocations accumulating in the lattice during deformation (Brewer et al., 2009). The patterns captured by EBSD can determine grain morphology, crystallographic orientation, and other information about the present phases, which are related to the properties and performance of materials. Consequently, this analysis may be important in studying the phase heterogeneity of welds. Additionally, it can be helpful for failure investigations, contributing to understanding the influence of grain boundaries on fracture and crack behaviour, as well as grain boundary sliding (Stojakovic, 2012).

Therefore, the present work aimed to study the behaviour of dissimilar corrosion-resistant weld metals subjected to the Trans-Varestraint test (TVT) to better comprehend previous results. The findings of this study have practical implications, as they provide valuable information on the effects of stress on microstructure. This knowledge can be applied to enhance the understanding of the metallurgical features of solidification cracking in dissimilar welding, thereby contributing to the development of more reliable and durable components.

The materials were samples from austenitic stainless steel and nickel alloy fusion zones of specimens subjected to TVT. In previous work (Chapter 3), the weldability of these weld combinations was assessed through crack measurements and by analysing the solidification route of each combination of base and filler metal. Here, detailed microstructural characterisation of the samples was carried out using light optical microscopy (LOM) and scanning electron microscopy (SEM) techniques, such as energy dispersive X-ray spectroscopy (EDS) and EBSD.

4.3 Experimental Procedure

Samples of the weld beads of specimens subjected to TVT were analysed. The welding procedure is detailed in a previous work, as well as the methodology of TVT (Chapter 3). The welds were performed by the SMAW process with AISI 310S and AISI 304H as the base metals. Three different covered electrodes were employed as filler metals: (1) AWS E310-15, which has an austenitic stainless steel core, (2) AWS E347-17, also a stainless steel electrode, and (3) AWS ENiCrFe-2, a nickel alloy electrode.

Figure 49 explains the origin of the weld bead samples studied here. Figure 49a shows a schematic of the TVT equipment utilised, showing a specimen after bending. In Figure 49b, the top view of a tested specimen is presented. The red dashed line marks the region of the weld bead where the cracks were identified on the surface. As indicated in Figure 49c, the samples for microscopy were taken from the cross-section of this area, which is adjacent to the region of the end of cracking and, at the moment of welding, corresponds to the location of the

solid–liquid interface (S/L).

Figure 49 — (a) Representation of the TVT equipment; (b) top view of a specimen having cracks resulting from TVT on the surface; (c) a macrograph of the cross-section of a sample

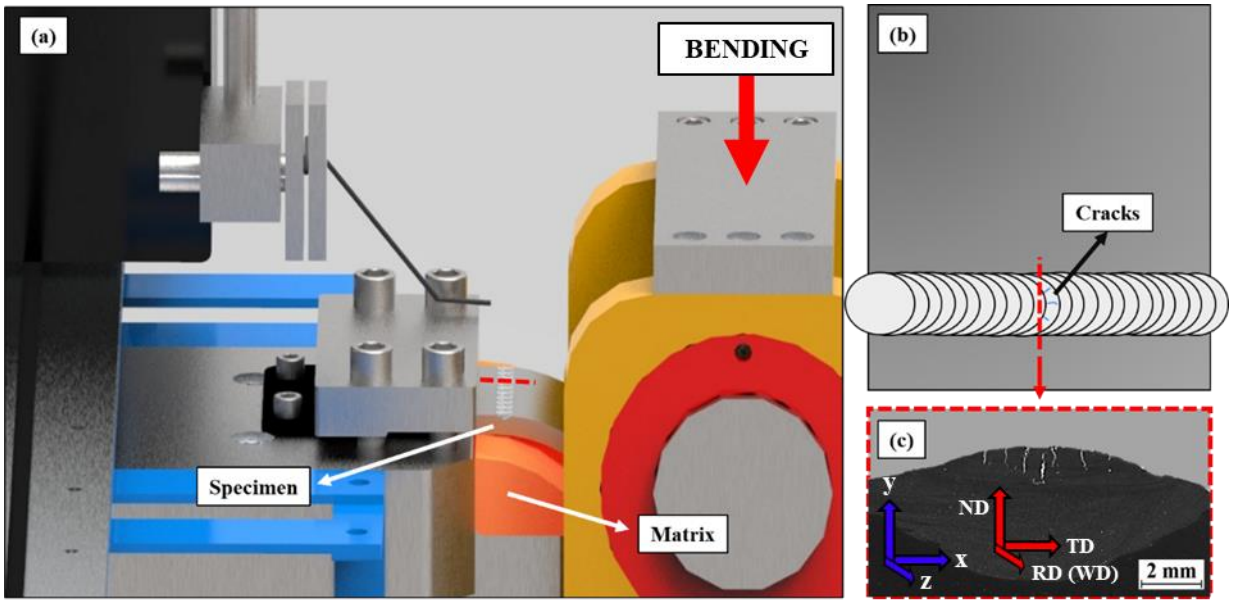

Source: elaborated by the author.

Table 17 shows the base metal, filler metal, and strain level applied in the TVT of the six samples analysed. These conditions were chosen for microstructural characterisation based on a previous assessment of each type of weld metal. In prior study (Chapter 3), Trans-Varestraint tests were performed in triplicate applying strains of 1%, 3%, and 6%. Based on these strain levels, the tests of the welds with the AWS E310-15 and AWS ENiCrFe-2 electrodes showed cracks at 1% of augmented strain. However, the weld metals from the welds with AWS E347-17 only started developing cracks at 3% of strain. Therefore, the samples corresponding to the strain level at 1% were chosen for analysing the welds with AWS E310-15 and AWS ENiCrFe-2. Conversely, the samples from tests with 3% of strain were selected for assessing the welds with AWS E347-17.

Table 17 — Welded combination and strain level used in the TVT

Sample	Base Metal	Filler Metal	Strain applied in TVT
A	AISI 310S	AWS E310-15	1%
B		AWS E347-17	3%
C		AWS ENiCrFe-2	1%
D	AISI 304H	AWS E310-15	1%
E		AWS E347-17	3%
F		AWS ENiCrFe-2	1%

Source: elaborated by the author.

The chemical composition of the fusion zones of the weld bead samples was determined by optical emission spectroscopy (OES). The results are shown in Table 18.

Table 18 — Chemical composition of samples' fusion zones

Element (wt.%)	Sample					
	A	B	C	D	E	F
Fe	51.82	62.72	31.85	58.43	69.18	36.78
Cr	25.84	21.47	19.55	22.69	19.18	16.29
Ni	19.27	12.87	43.18	15.93	8.84	41.56
Mn	1.87	1.16	1.80	1.88	0.93	1.80
Mo	0.03	0.10	1.18	0.07	0.15	1.30
Nb	0.01	0.10	0.88	0.02	0.36	0.93
V	0.07	0.06	0.04	0.05	0.06	0.03
Cu	0.08	0.06	0.04	0.09	0.09	0.07
Ti	0.014	0.020	0.012	0.013	0.020	0.015
Si	0.29	0.88	0.69	0.27	0.70	0.51
Co	0.22	0.22	0.17	0.10	0.16	0.10
W	0.32	0.25	0.12	0.30	0.22	0.11
Ta	-	-	0.28	-	-	0.32
Hf	-	-	0.12	-	-	0.10
C	0.101	0.041	0.052	0.092	0.042	0.056
N	0.026	0.027	0.01	0.03	0.028	0.073
P	0.031	0.018	0.018	0.03	0.033	0.019
S	0.005	0.006	0.006	0.004	0.008	0.005

Source: Chapter 3.

The samples were subjected to metallographic preparation through the following processes: grinding with 80, 120, 220, 320, 400, 600, 1200, 2500, and 5000 grit sandpaper, polishing with 6, 3, and 1 μm grit diamond paste, and automatic polishing for at least 10 hours with a colloidal silica suspension.

The microstructural characterisation utilised LOM and SEM, aiming to correlate the microstructural characteristics to the susceptibility to solidification cracking. For SEM analysis, secondary electron (SE), energy dispersive X-ray spectroscopy (EDS), and electron backscatter diffraction (EBSD) were performed.

The EBSD results were analysed trough Channel 5 package to obtain maps of band contrast, inverse pole figure (IPF), phase, kernel average misorientation (KAM), and Taylor factor (TF). In the KAM investigation, the values were calculated up to the third-nearest neighbour and for a subgrain angle of 5°. The investigation into the IPF and Taylor factor maps was concentrated on the z-coordinate, which is aligned with the deformation plane subjected to bending during the TVT (x, y), as illustrated in Figure 48. The objective of analysing Taylor factor maps was to elucidate the crystallographic characteristics of each fusion zone situated at the cessation points of crack propagation. This analysis aimed to enhance our understanding of stress accommodation effects on the microstructure, particularly focusing on the

microstructural attributes of grains that solidified in the vicinity of the cracks.

For the tests of the combinations with the AWS E347-17 electrode, which presented a biphasic fusion zone microstructure, the EBSD phase maps were compared to the results from a ferritoscope examination. Ferritoscope inspection followed the procedure described in the standard ISO 8249. Several measurements of the ferrite content of the weld beads were performed, and then the average value and the standard deviation were calculated.

Additionally, samples from regions of the weld beads without cracks were taken to optical microscopy analysis. These samples were ground, polished with diamond paste, and electrolytically etched according to the parameters presented in Table 19.

Table 19 — Electrolytic etching parameters

Filler Metal	Reagent	Voltage (V)	Time (s)
AWS E310-15	Oxalic acid	2.5	30
AWS E347-17			
AWS ENiCrFe-2	Chromic acid (10%)		60

Source: Chapter 3.

4.4 Results

4.4.1 Welds with the AWS E310-15 electrode

Figure 50 shows the microstructure of the fusion zones resulting from the deposition of the AWS E310-15 electrode on specimens of AISI 310S (sample A) and AISI 304H (sample D). These weld metals underwent primary austenite solidification in the fully austenitic (A) mode, with a columnar dendritic morphology. The LOM analysis also enabled the identification of inclusions distributed along the fusion zones. Examples of inclusions are indicated by the red arrows in the ampliations (images with black-dashed edges) in Figure 50a and Figure 50b.

Figure 50 — LOM micrographs (100× and 500×) of the fusion zones of (a) sample A (AISI 310S + AWS E310-15, deformed at 1%) and (b) sample D (AISI 304H + AWS E310-15, deformed at 1%); (c) secondary electron image and EDS maps of a particle identified in the fusion zone

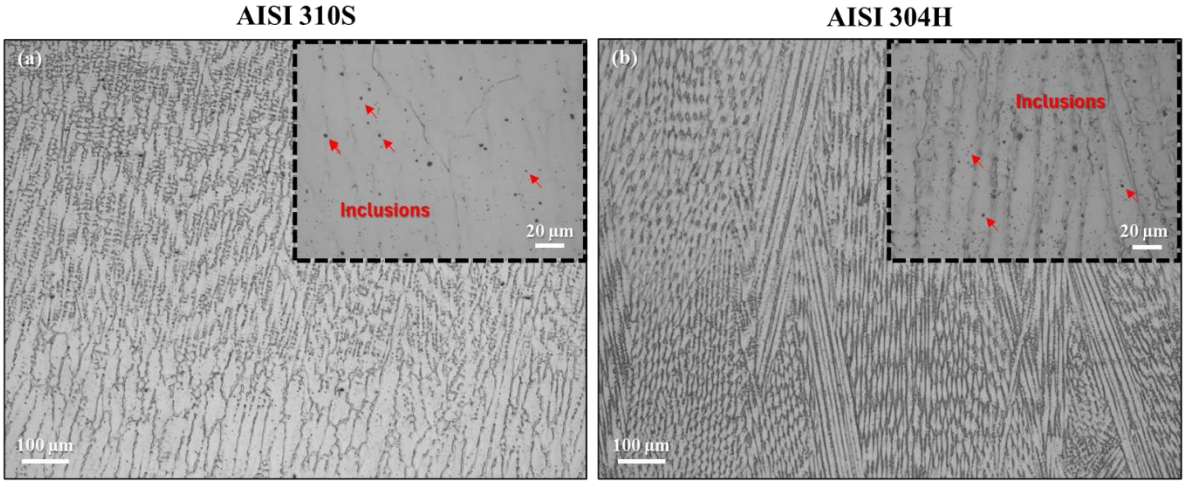

Source: elaborated by the author.

EDS analysis of sample D was conducted to collect information on the chemical composition of the particles detected by LOM. The secondary electron (SE) image of the region studied, which consists of the interdendritic region, and the EDS maps are shown in Figure 51. According to the results, this region has a central round particle rich in Mn and O, possibly an MnO inclusion surrounded by an area enriched in P, Cr, Mo, and Nb. The smaller round particles found in the fusion zone of sample D are likely SiO inclusions.

Figure 51 — Secondary electron image and EDS maps of a particle identified in the fusion zone of sample D (AISI 304H + AWS E310-15, deformed at 1%)

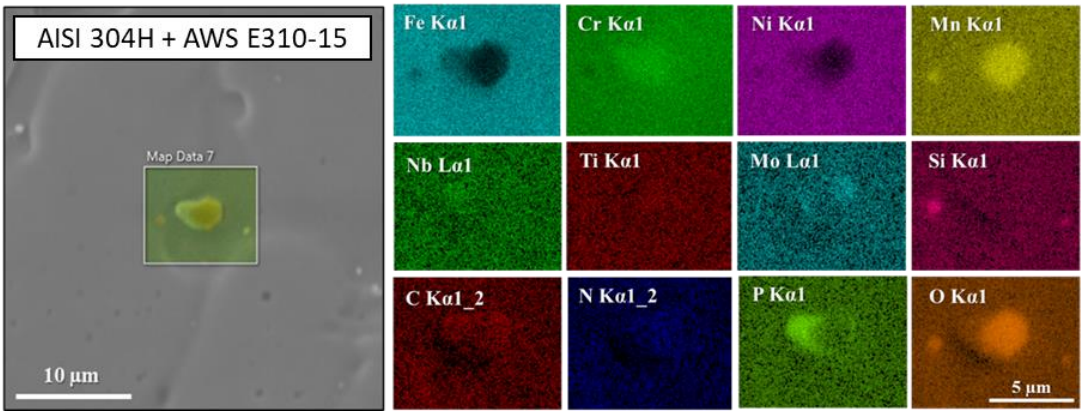

Source: elaborated by the author.

Figure 52 shows the EBSD results for sample D. Figure 52a and Figure 52b present the band contrast map and phase map, respectively, of the fusion zone region analysed at a

magnification of 250×. In Figure 52a, the austenite (γ) grains are grey, while the black areas correspond to cracks. As shown in Figure 52b, the only phase identified by EBSD was γ.

The two areas marked by red and blue dashed rectangles in Figure 52a were further examined at a magnification of 1000× to analyse the effects of the TVT's augmented strain on the microstructure. The results are presented in Figure 52e-h and Figure 52i-l. Figure 52e displays the band contrast map of the red-dashed rectangular region. The black lines are the grain boundaries between regions with misorientation angles greater than 15°. The subgrain boundaries, which have misorientation angles between 2° and 15°, are delimited by red lines (MUNÕZ et al., 2020).

The KAM map can identify deformed regions (Rui et al., 2021). Comparing Figure 52e to the KAM map shown in Figure 52f, the regions with greater misorientation are (1) adjacent to the cracks and (2) subgrain boundaries. The IPF map (Figure 52g) shows that some crystals near the cracks rotated during solidification. The colour changing, marked by the yellow arrows, indicates these rotations; the areas coloured in tones of light blue and purple indicate changes in the crystallographic orientation within the same grain.

Figure 52 — Results from the EBSD analysis of sample D (AISI 304H and AWS E310-15 weld, deformed at 1%): (a,e,i) band contrast; (b) phase; (f,j) KAM; (c,g,k) IPF; and (d,h,l) Taylor factor maps

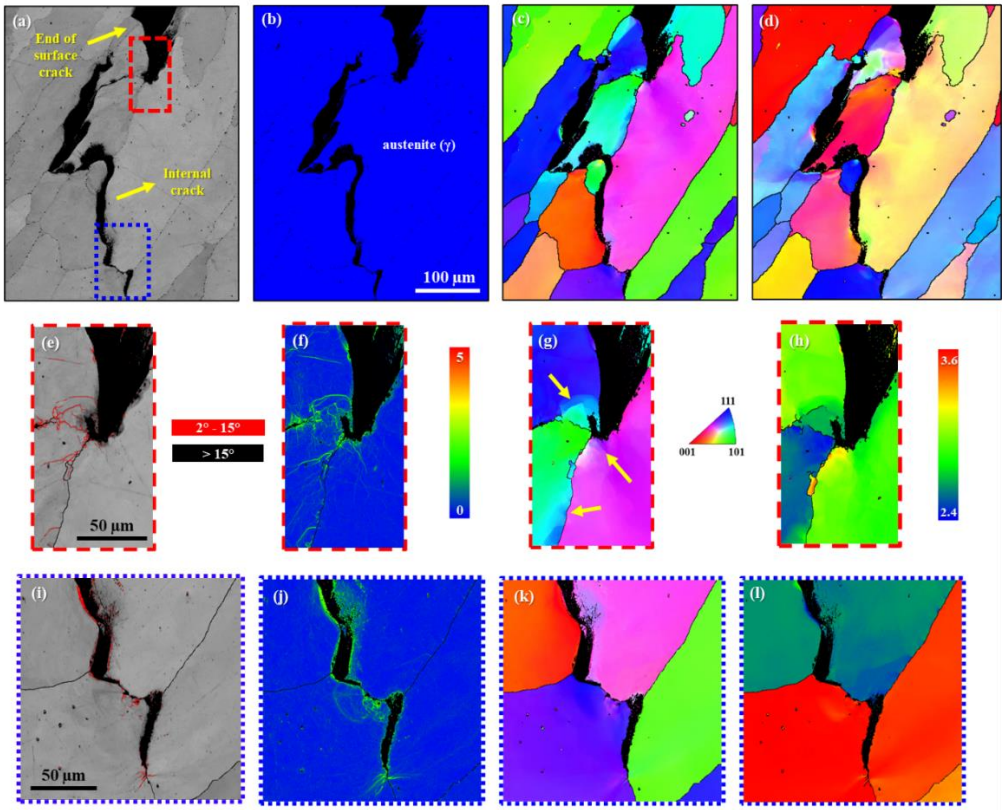

Source: elaborated by the author.

Figure 52h displays the Taylor factor map. The TF is a parameter calculated geometrically, representing the predicted yield response of a single crystal to shear strain when subjected to stress, considering its nearest neighbours (Taylor, 1938). For sample D, Figure 52 illustrates that the cracks tended to cease growing once they encountered high Taylor factor grains, which are more resistant to plastic deformation. Near the crack tips, the Taylor factor is slightly lower than that in other regions of the same grains.

The area marked by the blue-dashed rectangle in Figure 52a shows the same characteristics of the first ampliation, as shown in Figure 52i-l. Furthermore, the information from the EBSD analysis described above for sample D is also valid for sample A. In both samples, the grains with higher Taylor factors are oriented along the <111> and <101> directions.

4.4.2 Welds with the AWS E347-17 electrode

The microstructures of the fusion zones from the welds with the AWS E347-17 electrode utilising the AISI 310S (sample B) and AISI 304H (sample E) base metals are shown in Figure 53a and Figure 53b, respectively. The fusion zone of sample B (Figure 53a) solidified in the primary ferrite/secondary austenite (FA) mode, exhibiting a columnar dendritic structure. The core of the dendrites consists of vermicular δ-ferrite surrounded by an austenite phase.

The solidification of sample E also proceeded in FA mode. Figure 53b shows that the fusion zone consists of a mixture of δ-ferrite and austenite. However, in addition to vermicular δ-ferrite, lacy δ-ferrite was identified. Compared to sample B, the presence of lacy δ-ferrite indicates more ferrite in the weld metal, resulting from the test with AISI 304H. This was confirmed by the results of EBSD analysis and ferritoscope inspection, as shown in Table 20. Additionally, this fact is very evident in the EBSD phase maps (Figure 53c and Figure 53d), where the yellow areas correspond to δ-ferrite and the blue areas correspond to the austenite phase.

Table 20 — Ferrite content (%) of the welds with the AWS E347-17 electrode as filler metal

Base Metal	**Ferritoscope**		**EBSD**	
	Average	**Standard Deviation**	**Average**	**Standard Deviation**
AISI 310S	6.90	± 0.26	4.11	± 0.54
AISI 304H	8.43	± 0.21	7.73	± 0.62

Source: elaborated by the author.

Figure 53 — LOM micrographs (100× and 500×) of the fusion zones of (a) sample B (AISI 310S and AWS E347-17 weld, deformed at 3%) and (b) sample E (AISI 304H and AWS E347-17 weld, deformed at 3%); (c,d) EBSD phase maps

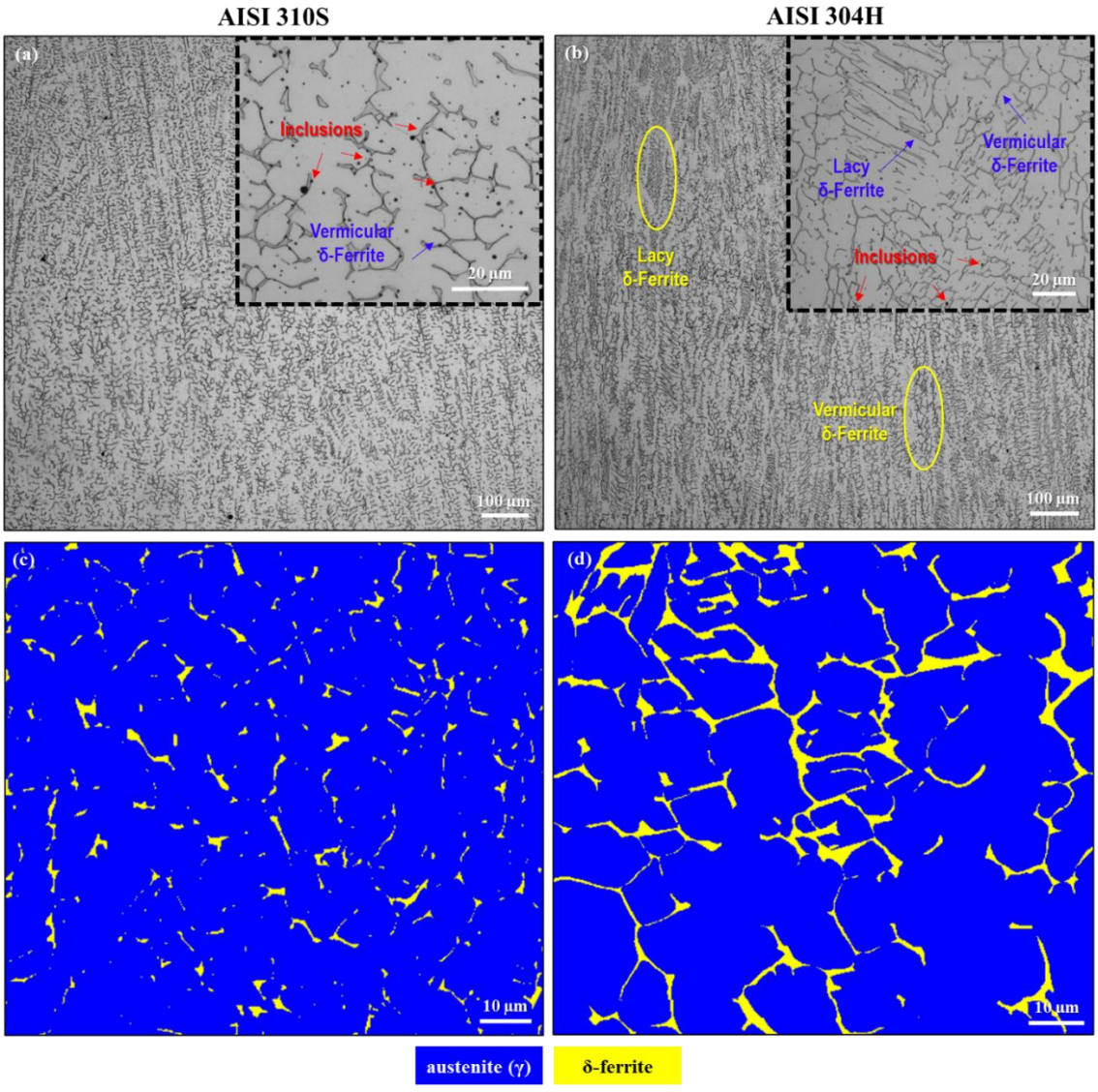

Source: elaborated by the author.

Microstructural analysis of samples B and E using SEM revealed the presence of precipitates distributed in the fusion zone, preferentially located near the δ-ferrite phase. According to the EDS maps in Figure 54 and Figure 55, the precipitates are Nb- and Mo-rich. It is essential to consider that the distinction of elements with similar X-ray characteristics, such as Nb (Lα = 2.166 keV), Mo (Lα = 2.293 keV), and S (Kα = 2.307 keV), is not very effective through EDS analysis. Therefore, due to their morphology, these precipitates are believed to be Nb(C,N), primary carbonitrides of the MX type (Silva et al., 2012; Zhang, Yang, 2018). Moreover, some inclusions were identified. The EDS maps in Figure 54 show a round particle

corresponding to a SiO inclusion. Based on Figure 55, the fusion zone of sample E appears to contain the same type of inclusion and MnO.

Figure 54 — EDS maps of precipitates detected in the fusion zone of sample B (AISI 310S and AWS E347-17 weld, deformed at 3%)

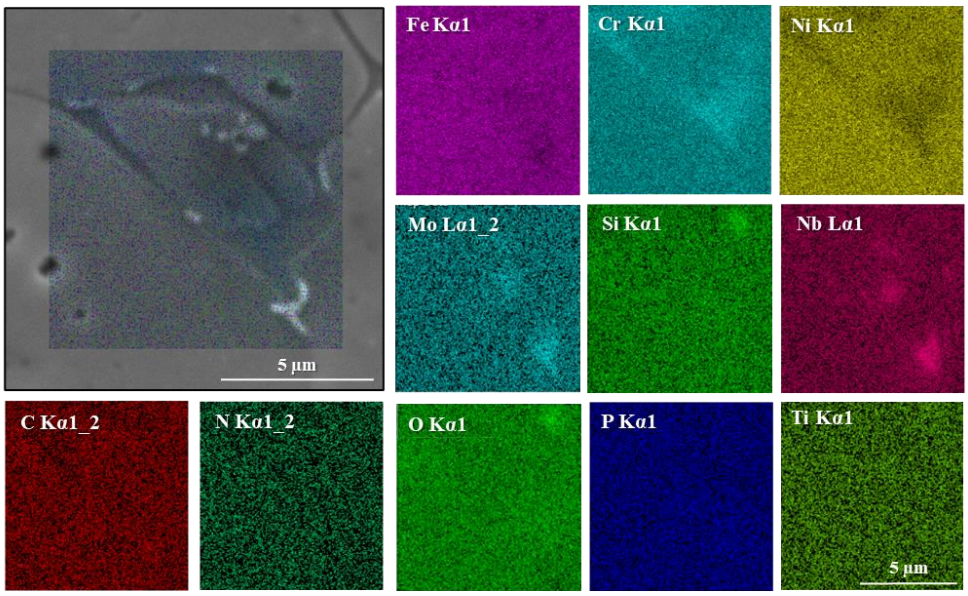

Source: elaborated by the author.

Figure 55 — EDS maps of precipitates detected in the fusion zone of sample B (AISI 310S and AWS E347-17 weld, deformed at 3%)

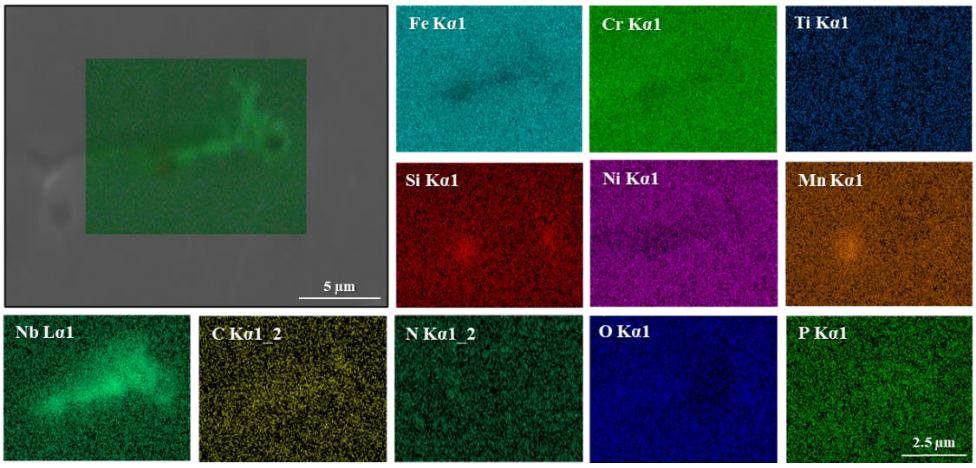

Source: elaborated by the author.

Figure 56 presents the EBSD analysis results for weld samples made with the AWS E347-17 electrode. As clearly observed in the band contrast maps (Figure 56a,f), the analysed regions in both fusion zones contain the end of a surface crack and internal cracks. The phase maps (Figure 56b,g) show the differences among these weld metals in terms of amount and shape of δ-ferrite. According to the KAM maps (Figure 56c,h), the areas adjacent to the cracks and subgrain boundaries have higher misorientation levels. Thus, the behaviour of these weld

metals was similar to that verified for welds with the AWS E310-15 electrode.

Figure 56 — EBSD analysis of the fusion zones of sample B (AISI 310S and AWS E347-17 weld, deformed at 3%) and sample E (AISI 304H and AWS E347-17 weld, deformed at 3%): (a,f) band contrast, (b,g) phase, (c,h) KAM, (d,i) IPF, and (e,j) Taylor factor maps

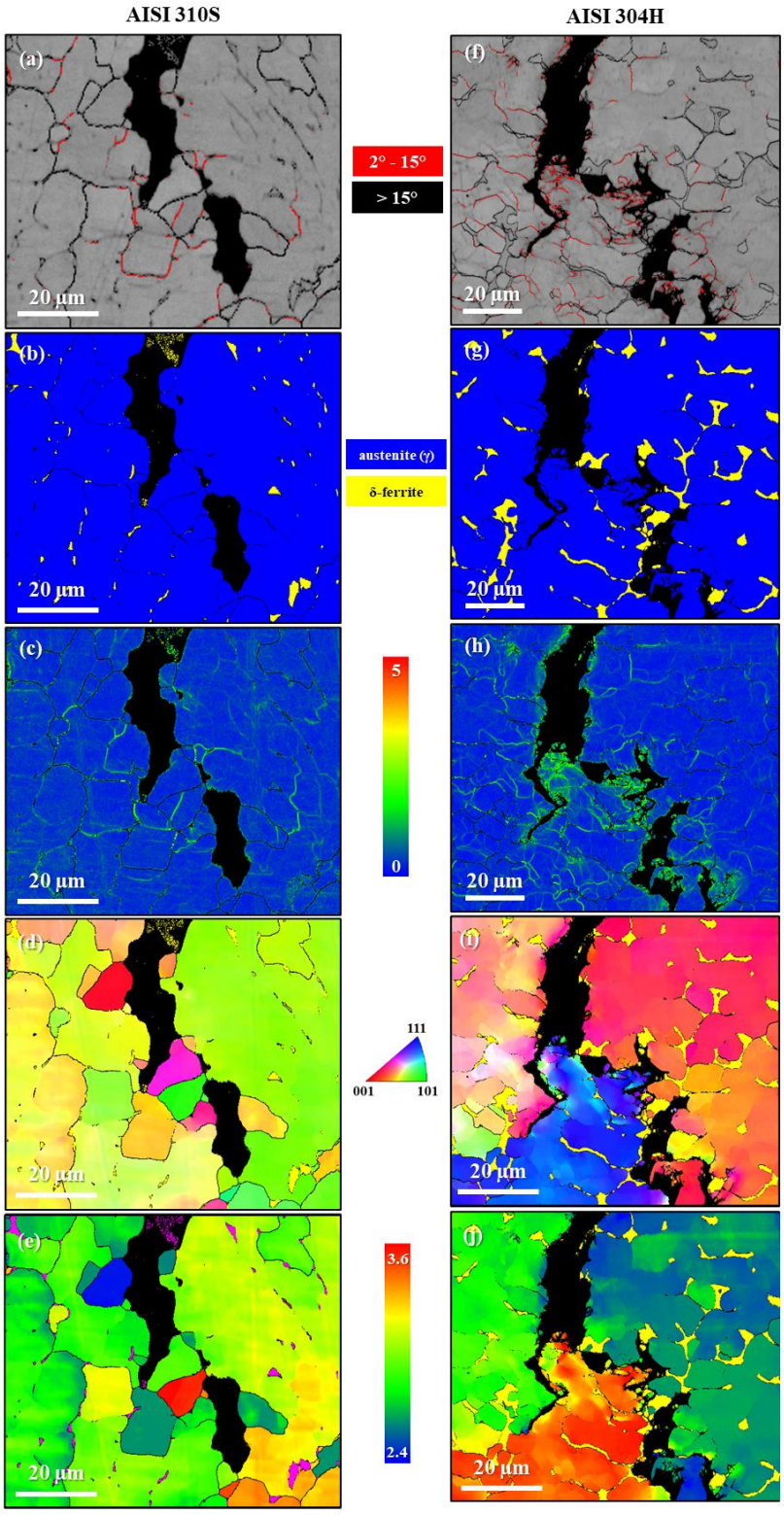

Source: elaborated by the author.

The IPF (Figure 56d,i) and Taylor factor (Figure 56e,j) maps show that (1) the crystals in the vicinity of the cracks underwent rotation and that (2) the propagation of the cracks was interrupted by grains oriented along <111> and <101>, which had higher Taylor factors. Another important characteristic of cracking was observed for sample E: internal cracks stopped growing when δ-ferrite was encountered, as shown in Figure 56f.

4.4.3 Welds with the AWS ENiCrFe-2 electrode

The microstructure of the weld metals resulting from the deposition of the AWS ENiCrFe-2 electrode on the base metals is shown in Figure 57, where Figure 57a corresponds to the fusion zone of the welding with the AISI 310S specimen (sample C) and Figure 57b is the fusion zone of the test using AISI 304H (sample F). Both fusion zones exhibited a columnar dendritic morphology and are primarily composed of the fcc phase of nickel (γ-Ni). The etching revealed the presence of tiny particles precipitated in interdendritic volumes and several inclusions distributed along the matrix.

Figure 57 — LOM micrographs (100× and 500×) of the fusion zones of (a) sample C (AISI 310S and AWS ENiCrFe-2 weld, deformed at 1%) and (b) sample F (AISI 304H and AWS ENiCrFe-2 weld, deformed at 1%)

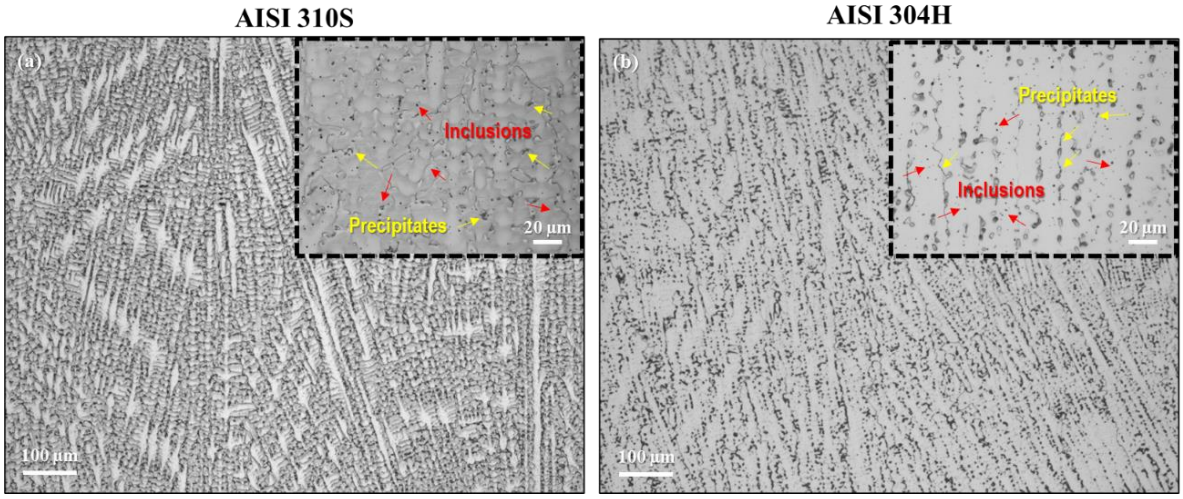

Source: elaborated by the author.

Samples C and F were examined using SEM for more detailed characterisation. Examples of the precipitates identified in the fusion zone of sample C are presented in Figure 58a, which contains an SE image. An enlargement of this area is presented in Figure 58b, indicating where the EDS analysis was carried out. The EDS maps shown in Figure 58c indicate that the precipitates are rich in Mo, Nb, S, C, and N. Considering their morphology, they were

understood to be niobium carbonitrides, NbC or NbN (Silva et al., 2012; Zhang, Yang, 2018). In turn, the inclusions (round particles) were identified as MnO and TiO. The formation of these types of precipitates and inclusions was also verified in sample F, as presented in Figure 59.

Figure 58 — (a,b) SEM-SE images of the precipitates in the interdendritic region of the fusion zone of sample C (AISI 310S and AWS ENiCrFe-2 weld, deformed at 1%); (c) EDS maps

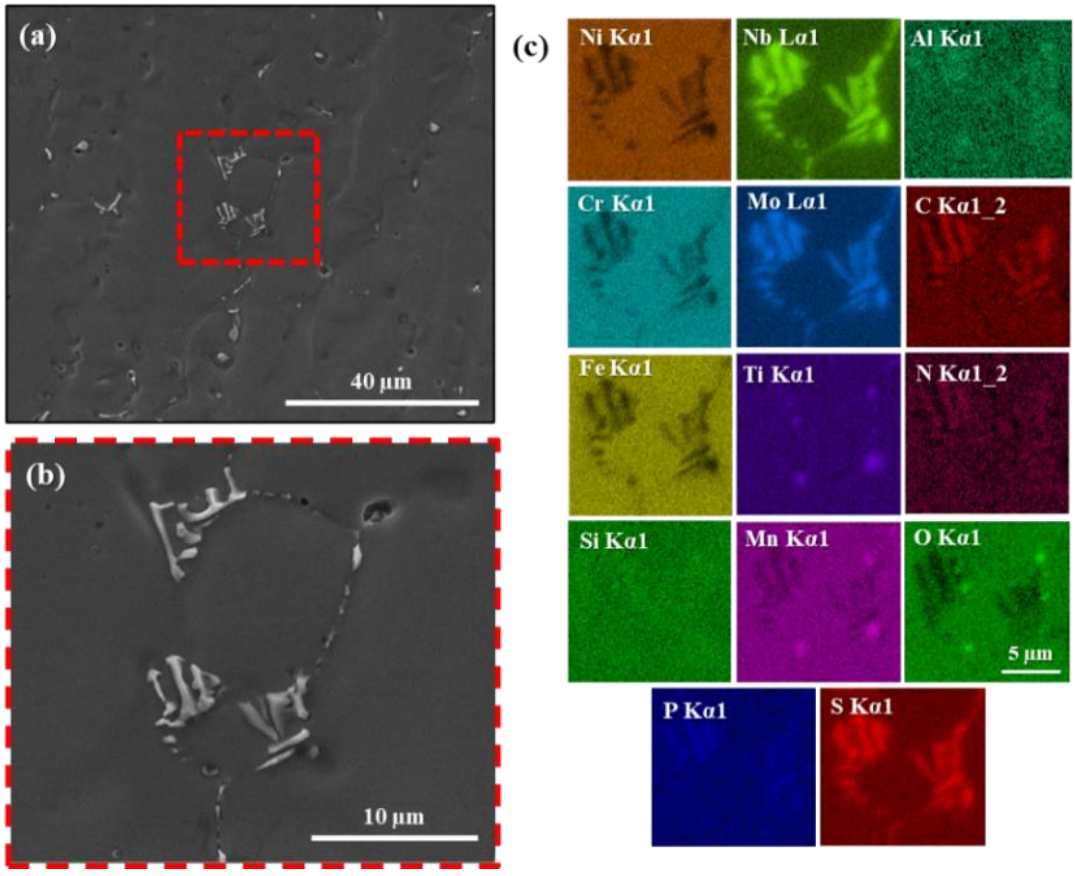

Source: elaborated by the author.

Figure 59 — (a) SEM-SE image of the precipitates in an interdendritic region of the fusion zone of sample F (AISI 304H and AWS ENiCrFe-2 weld, deformed at 1%); (b) EDS maps

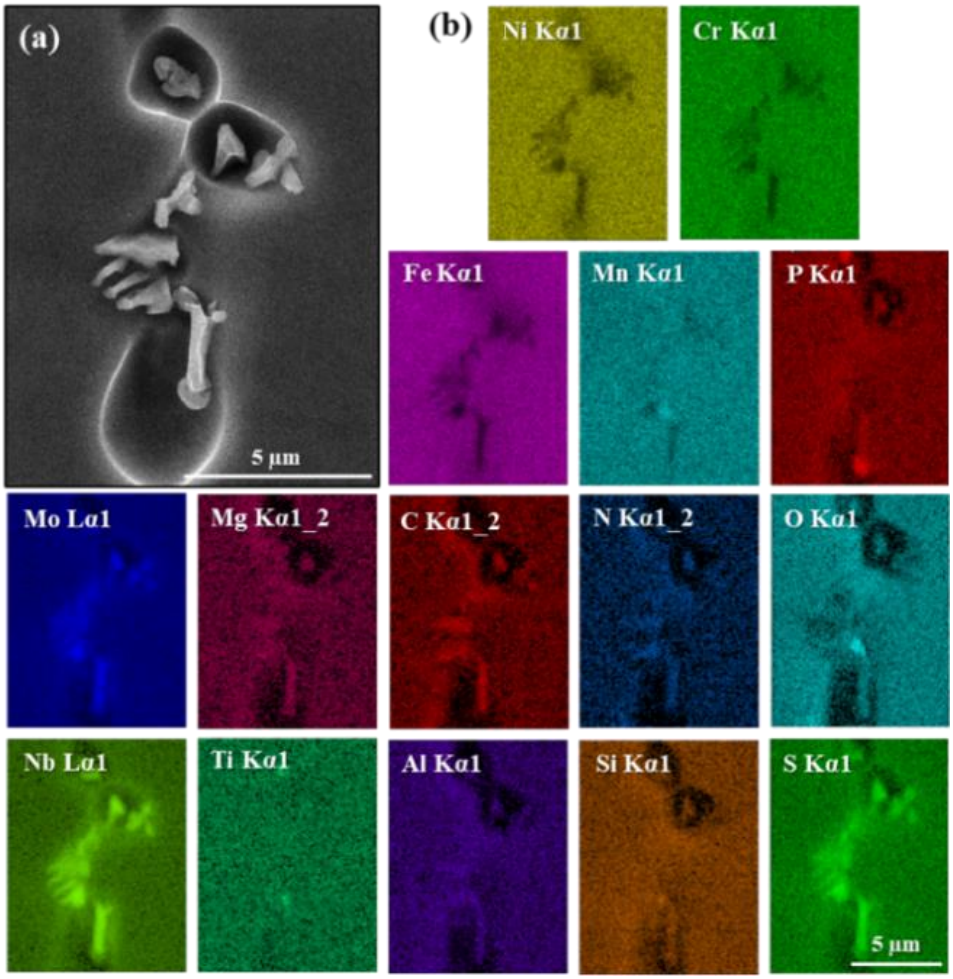

Source: elaborated by the author.

During the microscopic observation of the fusion zone of sample C, one eutectic structure, along with some precipitates, was identified. Figure 60a is the SE image corresponding to the interdendritic volume where these particles were located, and an amplification focusing on the eutectic is shown in Figure 60b. Furthermore, the EDS results (Figure 60c) confirmed that this eutectic was rich in P and Si, and it formed immediately adjacent to the Nb(C,N) precipitates.

Figure 60 — Eutectic identified in the fusion zone of sample C (AISI 310S and AWS ENiCrFe-2 weld, deformed at 1%): (a,b) SEM-SE images; (c) EDS maps

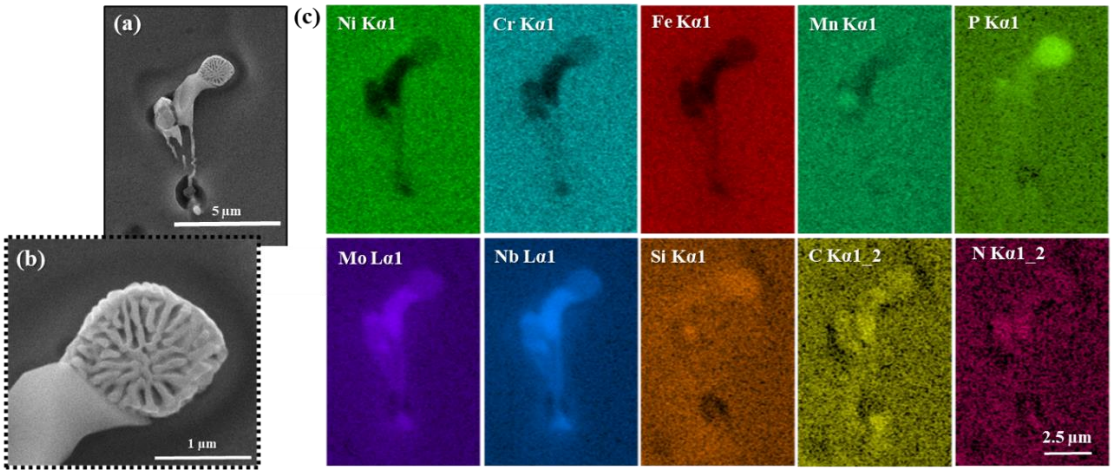

Source: elaborated by the author.

Figure 61a presents a macrograph of sample C. The blue-dashed rectangle indicates the area where the EBSD investigation was initially conducted. Figure 61b is the band contrast map of the marked region. The cracks on the right and left sides are surface cracks, and the central crack is an internal crack.

Figure 61 — (a) Macrograph of sample C (AISI 310S and AWS ENiCrFe-2 weld, deformed at 1%); (b) band contrast, (c) IPF, and (d) Taylor factor maps from EBSD analysis

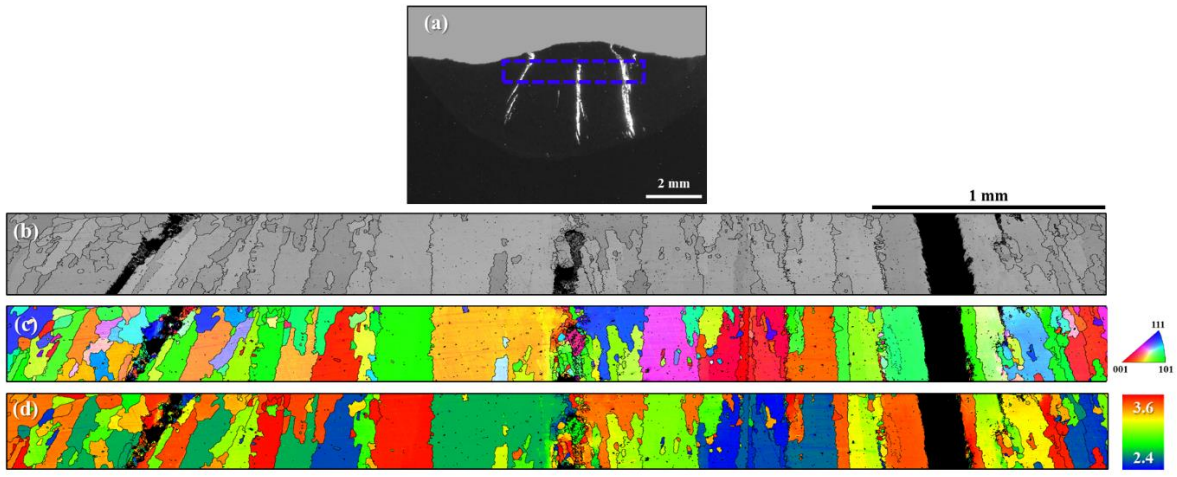

Source: elaborated by the author.

As shown in the IPF map (Figure 61c), grain refinement was confirmed near the cracks, i.e., the grains adjacent to the cracks being significantly smaller than the other grains in the matrix. The correlation between the IPF (Figure 61c) and Taylor factor (Figure 61d) maps indicated that the higher TF grains are oriented along the <101> direction.

An examination of sample C at enlarged magnification was performed to assess the misorientation characteristic. The findings are clearly illustrated in Figure *62*. Notably, this region of the fusion zone presents certain scratches, marked by the horizontal green lines indicating regions of elevated misorientation. These issues arose during metallographic preparation. Despite diligent and thorough polishing of all samples subjected to EBSD, the detachment of hard particles located embedded within the cracks was frequently observed. These hard particles often lead to the formation of extensive and deep scratches adjacent to the cracks. Furthermore, the polishing of the neighbouring crack regions was particularly challenging due to the significant deformation experienced in these areas. Nevertheless, for sample C, the misorientation levels (Figure 62c) were markedly higher in proximity to the high-TF grains (Figure 62e), which were located adjacent to solidification cracks.

Figure 62 — EBSD analysis of sample C (AISI 310S and AWS ENiCrFe-2 weld, deformed at 1%): maps of (a) band contrast, (b) phase, (c) KAM, (d) IPF, and (e) Taylor factor

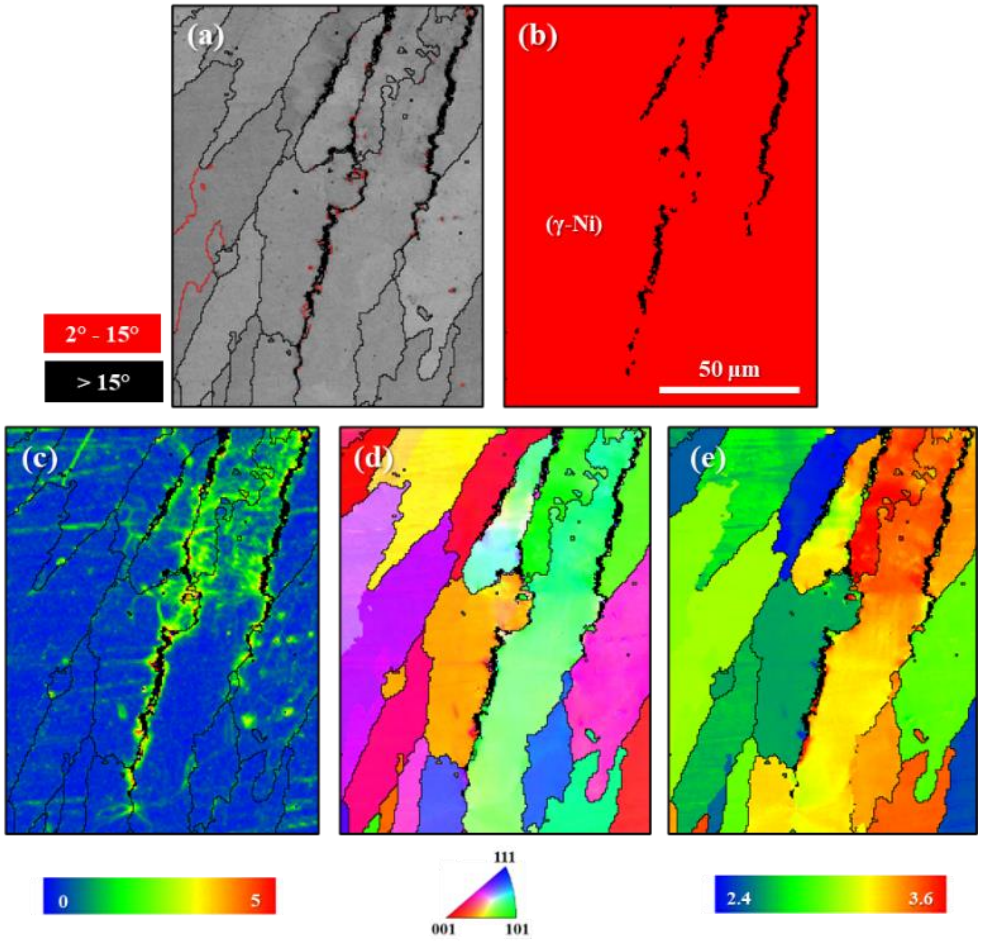

Source: elaborated by the author.

According to the EBSD maps shown in Figure 63, sample F exhibited similar

characteristics to sample C. More pronounced TFs were observed in grains positioned along <101> direction. Furthermore, grain refinement in the vicinity of the cracks is evident.

The analysis of sample F at higher magnification, focusing on some crack tips, is presented in Figure 63e-h. The KAM map in Figure 63f shows that the misorientation is elevated in the vicinity and along subgrain boundaries, as was verified for the austenitic stainless steel weld metals. The band contrast map in Figure 63e shows the grain refinement in the crack tips, another aspect already perceived for sample C.

Figure 63 — (a) Macrograph of sample F (AISI 304H and AWS ENiCrFe-2 weld, deformed at 1%); (b,e) band contrast, (c,g) IPF, (d,h) Taylor factor, and (f) KAM maps from EBSD analysis

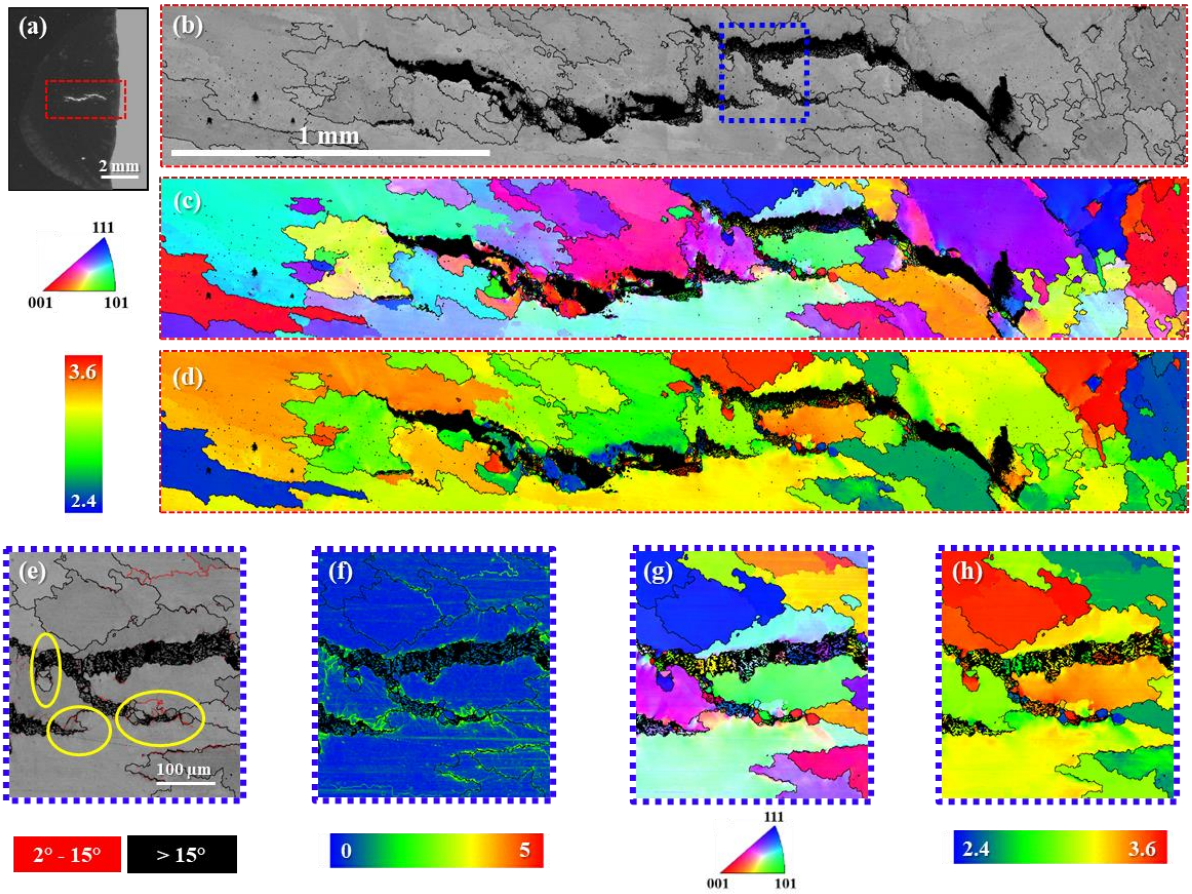

Source: elaborated by the author.

4.4.4 General observations

The fusion zones of the welds exhibited different characteristics in terms of grain size and morphology. For a clearer comparison between the samples, a general observation of the fusion zones resulting from welding with the three types of filler metal is shown in Figure 64, where the IPF maps from the EBSD analyses of samples D, E, and C are shown.

In Figure 64a, the microstructure of the fusion zone specimens welded with the AWS E310-15 electrode shows large austenite grains aligned parallel to each other. The grain boundaries are smooth, with no significant presence of secondary phases. In the fusion zones of the welds obtained using the AWS ENiCrFe-2 electrode, grain refinement was observed near the crack tips. Additionally, the other grains in the matrix are large, and a parallel arrangement between grains was noted. It is important to remember that the grain boundaries of the samples of welds with the AWS ENiCrFe-2 electrode contain several precipitates.

The fusion zones resulting from the welds with the AWS E347-17 electrode are represented in Figure 64b. They exhibited a significant amount of δ-ferrite, and the δ-ferrite formed complex and irregular boundaries with the austenite phase. Additionally, many small grains were detected, not only in the adjacent cracks.

Figure 64 — IPF maps of (a) sample D (AISI 304H and AWS 310-15 weld, deformed at 1%), (b) sample E (AISI 304H and AWS 347-17 weld, deformed at 3%), and (c) sample C (AISI 310S and AWS ENiCrFe-2 weld, deformed at 1%)

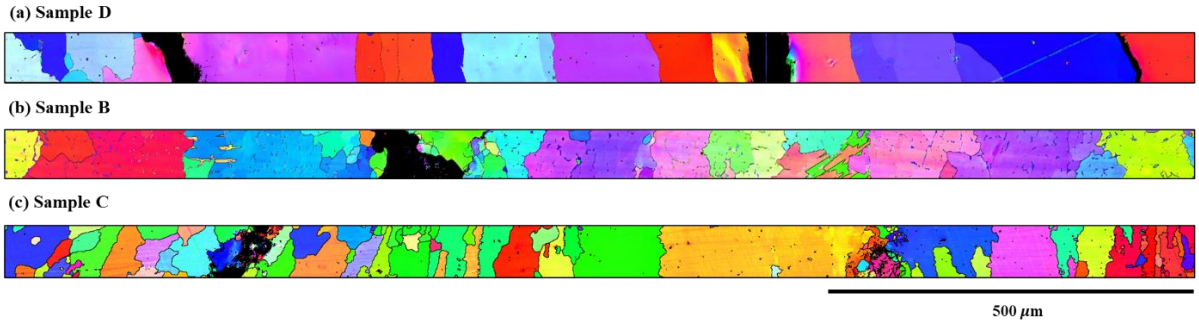

Source: elaborated by the author.

4.5 Discussion

Beyond the surface cracks, which propagated from the surface to the centre of the fusion zone, internal cracks were also identified when analysing the data from the microstructural characterisation of the weld bead cross-sections. Examples can be seen in Figure 52a, Figure 61a, and Figure 63a. This is very important because the evaluation of Trans-Varestraint Test results often aims only to measure surface cracks.

An intriguing feature observed in the cracks within weld bead cross-sections is the transition in their propagation mechanisms from solidification cracking to ductility-dip cracking. The IPF map in Figure 52c illustrates an internal crack that initially begins its development, behaving as a solidification crack, nucleating and growing through grain boundaries. However, at a certain point, it shifts into a transgranular crack, detaching regions

of the same grains, as a ductility dip crack. This duality of the crack's behaviour can also be observed in Figure 63. In any case, since this work focused on correlating the weld bead's microstructural features to solidification cracking, the conclusions took into account the results obtained specifically for those regions where the solidification crack comportment was properly identified.

All the fusion zones of the examined samples contained inclusions. The formation of inclusions was attributed to the welding process. In SMAW, slag-metal reactions often involve the oxidation of alloy elements originating from oxides. These oxides can be eliminated from the weld pool by entering the slag or remain in the liquid metal, becoming inclusion particles that are trapped in the weld metal during solidification (Kou, 2003).

The solidification mode greatly influences the resistance of the weld metal to solidification cracking. In stainless steel, the literature shows that four solidification modes can occur depending on the microchemical composition of the liquid phase. These modes are: completely austenitic (A), primary austenite/secondary ferrite (AF), primary ferrite/secondary austenite (FA), and completely ferrite (F) (Shankar et al., 2003). In addition, after the end of solidification, solid-state transformation from the primary phase to a secondary phase may occur depending on the chemical composition (David, 1981; Suutala, Takalo, Moisio, 1980).

The weld metals resulting from the deposition of the AWS E310-15 electrode in both base metals occurred in the A mode due to their high content of nickel and other austenitising elements. According to the inclusions detected in the interdendritic volumes of samples A and D, the EDS maps (Figure 50c) show intense segregation of ferritising alloy elements, such as Cr and Mo, which are partitioned in the stabilisation process of austenite, the primary phase in solidification. Phosphorus also segregates to interdendritic areas. The accumulation of impurity elements in this region may indicate the tendency of these weld metals to form residual low-melting-point eutectic or peritectic liquids (Brooks, Thompson, 1991). The existence of the remaining low-melting-point liquid at the final stages of solidification promotes solidification cracking (Koseki et al., 1994; Aucott, 2018).

In contrast to the samples with the AWS E310-15 electrode as the filler metal, the fusion zones of the samples from the welds produced with the AWS E347-17 electrode solidified in FA mode. This occurred due to the reduction in the content of austenitising elements, such as Ni, Mn, and C. Although there is an apparent decrease in the amount of Cr, the lower Ni level was more influential in promoting δ-ferrite formation (Silva et al., 2013). The δ-ferrite stabilisation causes segregation of austenitising elements to regions adjacent to the core of dendrites, where the austenite phase nucleates by a peritectic reaction (Suutala,

Takalo, Moisio, 1980).

The rapid cooling rate implied by the welding process favours the retention of δ-ferrite (SHANKAR et al., 2003). However, the ferrite percentages shown in Table *20* are much lower than the values predicted in previous work via thermodynamic simulation of solidification (Chapter 3). This may indicate that, due to the chemical composition of the weld metal, most of the δ-ferrite primarily originated during solidification and transformed into austenite through a solid-state transformation that occurred after the end of solidification (Brooks, Thompson, 1991; Suutala, Takalo, Moisio, 1980; Shankar et al., 2003). The austenite formed during solidification and the austenite resulting from the solid-state transformation are very similar in terms of phase (Suutala, Takalo, Moisio, 1980; David, 1981).

The higher content of δ-ferrite in the weld made with the AWS E347-17 electrode on AISI 304H base metal (sample E) was greater than that in the weld with the combination of AISI 310S (sample B) because of its lower amount of austenitising elements. The formation of Nb-rich carbonitrides in the fusion zones of samples B and E was also suggested by thermodynamic simulation (Chapter 3), which indicated the possible precipitation of niobium or titanium carbonitrides during solidification.

The results of Trans-Varestraint tests (Chapter 3) showed that the resistance to solidification cracking is significantly higher in welds using AWS E347-17 as the filler metal. Studies of austenitic stainless steel welds confirmed that cracks propagated along grain boundaries free of ferrite and halted when ferrite intersected (Hull, 1967; Brooks, Thompson, Williams, 1980; Brooks, Thompson, 1991). Here, Figure 56g provides evidence of this. This was linked to the beneficial effect of δ-ferrite in increasing the weldability of austenitic stainless steel welds (Arata, Matsuda, Saruwatari, 1974). Several authors have demonstrated that the presence of some δ-ferrite can significantly decrease the susceptibility to solidification cracking (Arata, Matsuda, Saruwatari, 1974; Lundin, Chou, Sullivan, 1980; Kujanpää, 1985). Austenitic stainless steel welds containing 4-10% δ-ferrite and fine dendrites are also resistant to stress and severe impacts under high-temperature conditions (Kaçar, Baylan, 2004; Meola et al., 2004; Naffakh, Shamanian, Ashrafizadeha, 2009).

Reviewing conclusions from numerous prior investigations, Brooks and Thompson (1991) listed the most relevant reasons to explain the benefit of ferrite. These include the following: (1) ferrite/austenite boundaries are anchored and irregular paths for crack propagation, whereas austenite/austenite have less complex morphologies, facilitating cracking (MATSUDA et al., 1967); (2) compared to austenite/austenite boundaries, ferrite/austenite boundaries have lower surface energies, which prevent these boundaries from being wetted by

the liquid remaining at the final stages of solidification, preventing the concentration of harmful low-melting point liquids (HULL, 1967); and (3) the solubility of impurities in ferrite is notably greater than that in austenite, causing less segregation and reducing the amount of low-melting point liquid accumulated in the interdendritic volumes (Brooks, Thompson, 1991).

The first rationale can be clearly seen in Figure 64. Contrasting Figure 64a to Figure 64b, austenite/austenite boundaries may offer more susceptibility to solidification cracking than ferrite/austenite boundaries, which tend to act as solid links and prevent separation (Hull, 1967). Furthermore, their grain size and morphology are also influenced. As mentioned before, the austenite/austenite boundaries appear to be more likely to tear when subjected to shear stress due to grain parallelism. In turn, the fusion zone of the welds with the AWS E347-17 electrode has smaller grains, which are misaligned with each other. This may imply a higher resistance to cracking since there are more grains with arbitrarily aligned slip planes, providing a chance for some slips to occur when stress is applied. If dislocations can easily move, the response of the material to the stress is deforming, which prevents cracking. Grains with more equiaxed geometry can better deform to accommodate stress. Additionally, fine-grained microstructures favour backfilling, which is the transfer of liquid into developing cracks to promote healing.

Kou (2015) stablished a criterion for solidification cracking criterion based on the characteristics of grain boundaries, which serve as nucleation sites for such cracks. This criterion considers three key factors: (1) the stress that causes the separation of grains; (2) the lateral growth of the grains towards each other to resist cracking; and (3) the liquid feeding along the grain boundary. When the contribution of factor 1 exceeds the combined contributions of factors 2 and 3, solidification cracking occurs (Kou, 2015; Liu et al., 2023). By analysing Kou's criterion and the results obtained in the present work, the greater resistance to solidification cracking of the welds with the AWS E347-17 electrode can again be understood. The presence of δ-ferrite can significantly affect factors 2 and 3, thereby contributing to their increase.

Nickel-alloy weld metals have exhibited a high tendency for cracking in previous research (Chapter 3). This can be explained by the effects of grain size, as previously discussed. However, it is understood that the precipitation of secondary phases significantly influences the susceptibility of these weld metals to solidification cracks. The weldability and mechanical properties of nickel alloy welds are known to be negatively affected by Cr precipitates (α-chromium), which form in the fusion zone and heat-affected zone, and by Nb-rich precipitates, which develop in the fusion zone within the interdendritic regions. Specifically, Nb precipitates adversely affect on ductility, fracture toughness, fatigue, and creep rupture (Caironi et al., 1993;

Belloni et al., 2001; Kuo, Lee, Tu, 2003; Naffakh, Shamanian, Ashrafizadeha, 2009).

The findings of this study show that the weld metals of samples C and F contain the highest levels of Nb and Mo among the examined conditions. Consequently, their fusion zones exhibited Nb carbonitrides (which could also be composed of some Mo) in the interdendritic regions. The solubility of Nb in γ-Ni is low. Therefore, Nb tends to segregate to the liquid during weld metal solidification. Additionaly, the low diffusion rate of Nb in γ-Ni hinders its diffusion to the dendrite core, which eliminates the concentration gradient and favours the formation of Nb-rich precipitates (Naffakh, Shamanian, Ashrafizadeha, 2008).

Another relevant aspect of the fusion zones in welds using the AWS ENiCrFe-2 electrode is the tendency to form low-melting-point eutectics in the liquid during the final stage of solidification, which may be greater than in austenitic stainless steel weld metals. An example of a phosphorus eutectic formed in the interdendritic region of the sample resulting from the weld with this electrode and AISI 310S is shown in Figure 58. Therefore, it is important to emphasise that this eutectic was not only observed after careful examination of the sample via SEM. Consequently, it is believed that the primary reason for its low resistance to solidification cracking is based on the explanations mentioned earlier.

The grain refinement near the crack tips verified for the nickel-alloy weld metals is probably related to dynamic recrystallisation caused by the concentration of tension in these regions during weld pool cooling.

The EBSD investigation furnished relevant information about the behaviour of the weld metals subjected to the Trans-Varestraint test. The higher misorientation levels surrounding the cracks are justified by the severe deformation level to which the microstructure is subjected to cracking; near the cracks, there is a very deformed portion of the grain, commonly denoted by the origination and accumulation of dislocations. The regions where dislocations accumulate eventually become subgrain boundaries.

The rotation of the crystals near the tips of the cracks, verified in all the samples, serves as evidence that some of the stress was indeed absorbed by the microstructure. Since the remaining stress was not enough to cause further deformation in high Taylor factor grains, crack propagation was halted. A comparison between the IPF maps and the band contrast maps that display grain and subgrain boundaries shows that these rotations are linked to the formation of subgrain boundaries.

The change in a crack's propagation behaviour from solidification cracking to ductility dip cracking mentioned before can be understood through the Taylor factor. Boundaries that separate grains with a larger difference in the Taylor factor are more prone to

intergranular fracture. Conversely, grains with higher Taylor factors tend to be less likely to deform and may be more prone to transgranular fracture, as shown in Figure 50d.

4.6 Conclusion

The present study offered valuable insights into the behaviour of dissimilar corrosion-resistant weld metals subjected to external stress during solidification tests using advanced microstructural characterisation techniques, supplementing previous work. The main conclusions are as follows:

(I) The solidification of the weld metals resulting from the deposition of the AWS E310-15 electrode occurred in the completely austenitic mode, which promoted the occurrence of solidification cracking. The fusion zones of the samples from the welds produced with the AWS E347-17 electrode solidified in the primary ferrite/secondary austenite mode, and their higher resistance to solidification cracking was associated with the beneficial effect of δ-ferrite in increasing the weldability of the ASSs. The welds with AWS ENiCrFe-2 were mostly composed of the γ-Ni phase, but the formation of Nb(C,N) precipitates in interdendritic volumes was very notable.

(II) The tendency of nickel-alloy weld metals to crack may be related to the precipitation of Nb(C,N) carbonitrides. The observed grain refinement near the crack tips may be attributed to dynamic recrystallisation driven by stress concentrations in these areas during the cooling of the weld pool. Furthermore, the presence of precipitates likely acts as nucleation sites for the formation of new grains, facilitating this microstructural evolution.

(III) The higher misorientation levels surrounding the cracks are justified by the severe deformation level to which the microstructure is subjected to cracking. Regions where dislocations accumulate eventually become subgrain boundaries.

(IV) Boundaries separating grains with a greater discrepancy in the Taylor factor may be more susceptible to intergranular fracture. In turn, grains with higher Taylor factors appeared to be less likely to deform and may be more susceptible to transgranular fracture.

5 SUMMARY

This work contributes to understanding the metallurgical aspects associated with the solidification cracking in corrosion-resistant alloy weld metals for high temperature operation in oil and gas industry. The main conclusions drawn were:

I) The ranking from least to most susceptible to the solidification cracking weld combination is as follows: (AISI 310S + AWS E347-17) > (AISI 304H + AWS E347-17) > (AISI 304H + AWS E310-15) > (AISI 310S + AWS E310-15) > (AISI 304H + AWS ENiCrFe-2) > (AISI 310S + AWS ENiCrFe-2).

II) Between the welds evaluated, the welds with the AWS E347-17 electrode exhibited the highest critical strain. Testing with AISI 310S revealed that cracks only developed at a strain of 3%, while its combination with AISI 304H showed cracks at a strain of 2%. Furthermore, the weld metal produced from the deposition of this electrode with both base metals had the lowest variation in crack lengths with increasing deformation, resulting in the lowest saturated strain.

III) The weld metals resulting from the deposition of the AWS E310-15 electrode solidified in the completely austenitic mode, which favoured solidification cracking. The fusion zones of the samples from the welds produced with the AWS E347-17 electrode solidified in the primary ferrite/secondary austenite mode, and their higher resistance to solidification cracking was associated with the beneficial effect of δ-ferrite in increasing the weldability of ASSs. The welds with AWS ENiCrFe-2 were mostly composed of the γ-Ni phase, but the formation of Nb(C,N) precipitates in interdendritic volumes was very notable.

IV) The higher misorientation levels were verified surrounding the cracks and along subgrain boundaries.

REFERENCES

ABOU-ELAZM, A.S.; MAHALLAWI, I.E.; ABDEL-KARIM, R.; RASHAD, R. Failure investigation of secondary super-heater tubes in a power boiler. **Engineering Failure Analysis**, Netherlands, vol. 16, pp. 433-448, 2009.

AFRIANSYAH, A.; ARIFIN, A. Dissimilar metal welding using shielded metal arc welding: a review. **Technology Reports of Kansai University**, Osaka, v. 62, n. 04, p. 1935-1948, 2020.

APBLETT, W. R.; PELLINI, W. S. Factors which influence weld hot cracking. **Welding Journal**, Miami, FL, v. 33, n. 2, p. 83-90, 1954.

ARATA, Y.; MATSUDA, F.; NAKATA, K.; SASAKI, I. Solidification crack susceptibility of aluminum alloy weld metals (Report I) — characteristics of ductility curves during solidification by means of the Trans-Varestraint test. **Transactions of Journal of Welding Research and Innovation**, Osaka, v. 5, n. 2, p. 153-167, 1976.

ARATA, Y.; MATSUDA, F.; KATAYAMA, S. Solidification Crack Susceptibility in Weld Metals of Fully Austenitic Stainless Steels (Report II) — Effect of Ferrite, P, S, C, Si and Mn on Ductility Properties of Solidification Brittleness. **Transactions of Journal of Welding Research and Innovation**, Osaka, vol. 6, pp. 105-116, 1977.

ARATA, Y.; MATSUDA, F.; NAKAGAWA, H.; KATAYAMA, S. Solidification Crack Susceptibility in Weld Metals of Fully Austenitic Stainless Steels (Report IV) — Effect of Decreasing P and S on Solidification Crack Susceptibility of SUS 310S Austenitic Stainless Steel Weld Metals. **Transactions of Journal of Welding Research and Innovation**, Osaka, vol. 7, pp. 169-172, 1978.

ARATA, Y.; MATSUDA, F.; NAKAGAWA, H.; KATAYAMA, S.; OGATA, S. Solidification Crack Susceptibility in Weld Metals of Fully Austenitic Stainless Steels (Report III) — Effect of strain rate on cracking threshold in weld metal during solidification. **Transactions of Journal of Welding Research and Innovation**, Osaka, vol. 6, pp. 197-207, 1977.

ARATA, Y.; MATSUDA, F.; SARUWATARI, S. Varestraint Test for Solidification Crack Susceptibility in Weld Metal of Austenitic Stainless Steels. **Transactions of the Welding Research Institute of Osaka University**, Osaka, vol. 3, pp. 79-88, 1974.

THE AMERICAN SOCIETY OF MECHANICAL ENGINEERS (ASME) INTERNATIONAL. **Weld Integrity and Performance, Chapter 14 "Properties of Stainless Steel Welds"**, p. 250, 1997. ISBN: 0/87170-600-8

THE AMERICAN SOCIETY OF MECHANICAL ENGINEERS (ASME). **Boiler and Pressure Vessel Code (BPVC), Section II, Part C:** Specifications for Welding Rods, Electrodes, and Filler Metals – SFA-5.4: Specification for Stainless Steel Electrodes for Shielded Metal Arc Welding. 2015.

AUCOTT, L.; HUANG, D.; DONG, H. B.; WEN, S. W.; MARSDEN, J.; RACK, A.; COCKS, A. C. F. A Three-Stage Mechanistic Model for Solidification Cracking During Welding of Steel. **Metallurgical and Materials Transactions A**, Warrendale, vol. 49A, 1674-1682, 2018.

BAESLACK, W.; LIPPOLD, J.; SAVAGE, W. F. Unmixed Zone Formation in Austenitic Stainless Steel Weldments. **Welding Research Supplement**, Miami, vol. 06, pp. 168s-176s, 1979.

BELAN, J. GCP and TCP phases presented in nickel-base superalloys. Elsevier Science Ltd.: **Materials Today: Proceedings**, Netherlands, vol. 3, pp. 936-941, 2016.

BELLONI, G.; CAIRONI, G.; GARIBOLDI, A.; LO CONTE, A.; DI MILANO, P. Effect of microstructural alteration on the creep behaviour and effect of flaws in 50Cr50Ni-Nb engineering alloy. **Transactions SMiRT**, Washington D.C., vol. 16, paper 1546, 2001.

BOCHVAR, A.; SVIDERSKAYA, Z. Failure of castings under the effect of shrinkage stresses during solidification in relation to the composition of the alloy. **Izv. Akad. Nauk SSSR, Otd. Tekhm. Nauk.**, Moscow, vol. 3, pp. 349-354, 1947.

BORDÍN, S. F.; LIMANDRI, S.; RANALLI, J. M.; CASTELLANO, G. EBSD spatial resolution for detecting sigma phase in steels. **Ultramicroscopy**, Netherlands, vol. 171, pp. 177-185, 2016.

BORLAND, J. Generalized theory of super-solidus cracking in welds (and castings). **British Welding Journal**, London, vol. 7, no. 8, pp. 508-512, 1960.

BREWER, L. N.; FIELD, D. P.; MERRIMAN, C. C. **Mapping and assessing plastic deformation using EBSD**. In: SCHWARTZ, A.; KUMAR, M.; ADAMS, B.; FIELD, D. (Ed.). Electron Backscatter Diffraction in Materials Science. Boston, MA: Springer, 2009. p. 251-262.

BROOKS, J. A.; THOMPSON, A. W. Microstructural development and solidification cracking susceptibility of austenitic stainless steel welds. **International Materials Reviews**, London, vol. 36:1, pp. 16-44, 1991.

BROOKS, J.A.; THOMPSON, A.W.; WILLIAMS, C. Microstructural development and solidification cracking susceptibility of austenitic stainless steel welds. In: KOSSOWSKY, R.; GLICKSMAN, M.E. (Eds.). **Physical Metallurgy of Metal Joining**. Warrendale, PA: The Metallurgical Society of AIME, 1980. p. 117-136.

CAIRONI, G.; GARIBOLDI, E.; SILVA, G.; VEDANI, G. Influence of heat treatments on the mechanical properties and microstructure of a 50Cr-50Ni niobium containing alloy. **Proceedings of Journal de Physique IV**, France, vol. 3, no. 7, pp. 289-295, 1993.

CAMPBELL, R. D.; WALSH, D. W. Weldability Testing. In: **ASM HANDBOOK, Volume 6: Welding, Brazing, and Soldering**. Ohio: ASM International, 1993. p. 603-613.

COLLINS, M. G.; LIPPOLD, J. C. An Investigation of Ductility Dip Cracking in Nickel-Based Filler Materials — Part I. **Welding Research**, Miami, vol. 10, pp. 288s-295s, 2003.

CONIGLIO, N.; CROSS, C. E. Initiation and growth mechanisms for weld solidification cracking. **International Materials Reviews**, London, vol. 58, no. 7, pp. 375-397, 2013.

CROSS, C. On the Origin of Weld Solidification Cracking. In: BÖLLINGHAUS, T.; HEROLD, H. **Hot Cracking Phenomena in Welds**. Heidelberg: Springer, 2005.

DAVID, S. A. Ferrite morphology and variations in ferrite content in austenitic stainless steel welds. **Welding Journal**, Miami, vol. 60, no. 4, pp. 63-71, 1981.

DELONG, W. T. Ferrite in Austenitic Stainless Steel Weld Metal. **Welding Research Supplement**, Miami, vol. 53, no. 7, pp. 273s-286s, 1974.

DIVYA, M.; PRASANTHI, T. N.; DAS, C.R.; SUDHA, C.; VASUDEVAN, M. Weldability study of 304HCu stainless steel using varestraint and “Gleeble” based hot ductility tests. **Materials Today Communications**, Amsterdam, vol. 37, 106938, 2023.

DUPONT, J. N.; LIPPOLD, J. C.; KISER, S. D. **Welding Metallurgy and Weldability of Nickel-base Alloys**. New Jersey: John Wiley & Sons. 2009. ISBN 978-0-470-08714-5

DUPONT, J.N. Solidification of an alloy 625 weld overlay. **Metallurgical and Materials Transactions A**, Warrendale, vol. 27, pp. 3612-3620, 1996.

ERNST, F.; LI, D.; KAHN, H.; MICHAL, G. M.; HEUER, A. H. The carbide M_7C_3 in low-temperature-carburized austenitic stainless steel. **Acta Materialia**, Oxford, vol. 59, pp. 2268-2276, 2011.

FINK, C.; WANG, H.; ALEXANDROV, B. T.; PENSO, J. Filler Metal 16-8-2 for Structural Welds on 304H and 347H Stainless Steels for High-Temperature Service. **Welding Journal**, Miami, vol. 99, pp. 312s-322s, 2020.

GHALAMBAZ, M.; ABDOLLAHI, M.; ESLAMI, A.; BAHRAMI, A. A case study on failure of AISI 347H stabilized stainless steel pipe in a petrochemical plant. **Case Studies in Engineering Failure Analysis**, Amsterdam, vol. 9, pp. 52-62, 2017.

GOODWIN, G. M. Test Methods for Evaluating Hot Cracking: Review and Perspective. In: **Proceedings of the First United States-Japan Symposium on Advances in Welding Metallurgy**, San Francisco, CA, USA & Yokohama, Japan, 7–13 June 1990. p. 59-78.

HALL, E.O. The deformation and ageing of mild steel: {III} discussion of results. **Proceedings of the Physical Society. Section B**, London, vol. 64, pp. 747-753, 1951.

HEMSWORTH, B.; BONISZEWSKI, T.; EATON, N. F. Classification and definition of high-temperature welding cracks in alloys. **Metal Construction and British Welding Journal**, London, vol. 1, no. 1, pp. 5-15, 1969.

HSIEH, C. C.; WU, W. Overview of Intermetallic Sigma (σ) Phase Precipitation in Stainless Steels. **ISRN Metallurgy**, Cairo, v. 2012, art. 732471, 2012.

HULL, F. C. Effect of delta ferrite content on hot cracking of stainless steel. **Welding Journal**, Miami, vol. 46, pp. 399s-409s, 1967.

INTERNATIONAL ORGANIZATION FOR STANDARDIZATION. **ISO 8249**: Welding — Determination of Ferrite Number (FN) in austenitic and duplex ferritic-austenitic Cr-Ni stainless steel weld metals. 2018.

INTERNATIONAL ORGANIZATION FOR STANDARDIZATION. **ISO TR 17641-3**: Destructive tests on welds in metallic materials — Hot cracking tests for weldments — Arc Welding Processes, part 3: Externally loaded tests. 2005.

JANG, A.Y.; LEE, D. J.; LEE, S.H.; SHIM, J. H.; KANG, S.W.; LEE, H.W. Effect of Cr/Ni equivalent ratio on ductility-dip cracking in AISI 316L weld metals. **Materials and Design**, Oxford, vol. 32, pp. 371-376, 2011.

JIANG, Y.; KAN, Y.; WU, C.; CHEN, H. Irradiation-Assisted Microstructure Evolution and Mechanical Properties Loss of 310S Welded Joints. **Metals**, Basel, vol. 13, 858.

KAÇAR, R.; BAYLAN, O. An investigation of microstructure/property relationships in dissimilar welds between martensitic and austenitic stainless steels. **Materials & Design**, Oxford, vol. 25, pp. 317-329, 2004.

KAEWKUMSAI, S.; KHONRAENG, W.; SATHIRACHINDA, N. High temperature failure of natural gas feed burner pipe. **Engineering Failure Analysis**, Oxford, vol. 27, pp. 74-83, 2013.

KANEKO, K.; FUKUNAGA, T.; YAMADA, K.; NAKADA, N.; KIKUCHI, M.; SAGHI, Z.; BARNARD, J. S.; MIDGLEY, P. Formation of M23C6-type precipitates and chromium-depleted zones in austenite stainless steel. **Scripta Materialia**, Oxford, vol. 65, pp. 509-512, 2011.

KANNENGIESSER, T.; BOELLINGHAUS, T. Hot cracking tests — an overview of present technologies and applications. **Welding in the World**, Roissy-Charles-de-Gaulle, vol. 58, pp. 397–421, 2014.

KATAYAMA, S. Solidification phenomena of weld metals (2nd Report). Solidification theory, solute redistribution and microsegregation behaviour. **Welding International**, Abingdon, vol. 14, pp. 952-953, 2000.

KATAYAMA, S.; FUJIMOTO, T.; MATSUNAWA, A. Correlation among Solidification Process, Microstructure, Microsegregation and Solidification Cracking Susceptibility in Stainless Steel Weld Metals. **Transactions of the Welding Research Institute of Osaka University**, Osaka, vol. 14, pp. 123-138, 1985.

KINGTON, A. V.; NOBLE, F. W. σ Phase embrittlement of a type 310 stainless steel. **Materials Science and Engineering**, Lausanne, vol. A138, pp. 259-266, 1991.

KOLTS, J. Alloy 718 for the Oil and Gas Industry. In: LORIA, E. A. (Ed.). Superalloys 718, 625 and Various Derivatives. Warrendale, PA: **The Minerals, Metals & Materials Society (TMS)**, 1989. p. 329–344.

KOSEKI, T.; MATSUMIYA, T.; YAMADA, W.; OGAWA, T. Numerical Modeling of Solidification and Subsequent Transformation of Fe-Cr-Ni Alloys. **Metallurgical and Materials Transactions A**, Warrendale, vol. 25a, pp. 1309-1321, 1994.

KOTECKI, D. J. Ferrite Determination in Stainless Steel Welds — Advances since 1974. **Welding Research Supplement**, Miami, vol. 1, pp. 24s-37s, 1997.

KOTECKI, D. J.; SIEWERT, T. A. WRC-1992 Constitution Diagram for Stainless Steel Weld Metals: A Modification of the WRC-1988 Diagram. **Welding Journal**, Miami, vol. 71, no. 5, pp. 171-178, 1992.

KOU, S. A criterion for cracking during solidification. **Acta Materialia**, Oxford, vol. 88, pp. 366-374, 2015.

KOU, S. Solidification and Liquation Cracking Issues in Welding. **Journal of the Minerals, Metals & Materials Society**, Oxford, vol. 55, pp. 37-42, 2003.

KOU, S. **Welding Metallurgy**. 2nd ed. New Jersey: John Wiley & Sons, 2002.

KROMM, A.; THOMAS, M.; KANNENGIESSER, T.; GIBMEIER, J.; VOLLERT, F. Assessment of the Solidification Cracking Susceptibility of Welding Consumables in the Varestraint Test by Means of an Extended Evaluation Methodology. **Advanced Engineering Materials**, Weinheim, vol. 24, 2022.

KUJANPÄÄ, V. P. Effect of steel type and impurities in solidification cracking of austenitic stainless steel welds. **Metal Construction**, London, vol. 17, no. 1, pp. 40R-60R, 1985.

KUJANPÄÄ, V. P.; DAVID, S. A.; WHITE, C. L. Formation of Hot Cracks in Austenitic Stainless Steel Welds — Solidification Cracking. **Welding Journal**, Miami, vol. 8, pp. 203s-212s, 1986.

KUJANPÄÄ, V. P.; SUUTALA, N.; TAKALO, T.; MOISIO, T. Correlation between solidification cracking and microstructure in austenitic and austenitic-ferritic stainless steel welds. **Welding Research International**, London, vol. 9, no. 2, pp. 55-76, 1979.

KUO, T.Y.; LEE, H.T.; TU, C.C. Evaluation of effects of niobium and manganese addition on nickel base weldments. **Science and Technology of Welding and Joining**, Abingdon, vol. 8, pp. 39-48, 2003.

MIRANDA H.C.; PEQUENO D.A.C.; AGUIAR, W.M.; MOMBRU, R.G.; MINA, E.M.; SILVA, C.C.; MOTTA, M.F.; CAVALCANTE, N.E.; SILVA, R.S. **Desenvolvimento de Técnicas Especiais de Soldagem para Manutenção em UEPs**. Fortaleza: ANP; PETROBRAS; 2018. Laboratório de Pesquisa e Tecnologia em Soldagem (LPTS), Research Project, Process 2016/00309-0, SAP 4600554504 – SIGITEC.

LANCASTER, J. F. **Metallurgy of Welding**. 6th ed. Cambridge: Woodhead Publishing Limited, 1999.

LI, Y.; WANG, J.; HAN, E. H.; WU, W.; HÄNNINEN, H. Multi-scale study of ductility-dip cracking in nickel-based alloy dissimilar metal weld. **Journal of Materials Science & Technology**, Amsterdam, vol. 35, pp. 545-559, 2019.

LIPPOLD, J.C. **Recent Developments in Weldability Testing**. In: Hot cracking phenomena in welds. Heidelberg: Springer-Verlag, pp. 271-290, 2005. ISBN: 3-540-22332-0.

LIPPOLD, J. C. Recent developments in weldability testing for advanced materials. In: **Joining of Advanced and Specialty Materials VII**. Materials Park, OH: ASM International, 2005. (no. 05116G).

LIPPOLD, J.C; KOTECKI, D. J. **Welding metallurgy and weldability of stainless steel**. 1st ed. New Jersey: John Wiley & Sons Incorporated, 2005.

LIPPOLD, J. C.; CLARK, W. A.; TUMULURU, M. An Investigation of Weld Metal Interfaces. In: **The Metal Science of Joining**. Materials Park, OH: ASM International, 1992. pp. 141–146.

LIPPOLD, J. C.; LIN, W. Weldability of Commercial Al-Cu-Li Alloys. **Materials Science Forum**, Stafa-Zurich, vols. 217-222, pp. 1685-1690, 1996.

LIU, K.; WANG, H.; LI, J.; GENG, S.; CHEN, Z.; OKULOV, A. A Review on Factors Influencing Solidification Cracking of Magnesium Alloys During Welding. **Metals and Materials International**, Seoul, vol. 30, pp. 1723-1742, 2024.

LUNDIN, C. D.; CHOU, C.- P. D.; SULLIVAN, C. J. Hot Cracking Resistance of Austenitic Stainless Steel Weld Metals. **Welding Journal**, Miami, vol. 8, pp. 226s-232s, 1980.

LUNDIN, C. D.; DELONG, W. T.; SPONDS, D. F. Ferrite-Fissuring Relationship in Austenitic Stainless Steel. **Welding Journal**, Miami vol. 54, pp. 241s-246s, 1975.

LUTHER, S. J.; ALEXANDROV, B. T.; MCCRACKEN, S. L.; TATMAN, J. K. Correlation of imposed mechanical energy with ductility-dip cracking in a highly restrained weld of Alloy 52. **Journal of Manufacturing Processes**, Oxford, vol. 79, pp. 767-788, 2022.

MAHDI, E.; ESMAIELI, A. Failure Analysis of a Flare Tip Used in Offshore Production Platform in Qatar. **Materials**, Basel, vol. 13, pp. 3426, 2020.

MARQUES, P. V.; MODENESI, P. J.; BRACARENSE, A. Q. **Soldagem**: fundamentos e tecnologia. 4th ed. Rio de Janeiro: Elsevier, 2017.

MATSUDA, F.; ARATA, Y.; KATAYAMA, S. Solidification crack susceptibility in weld metals of fully austenitic stainless steels (Report III)—effect of strain rate on cracking threshold in weld metal during solidification. **Transactions of Journal of Welding Research and Innovation**, Tokyo, vol. 6, pp. 197-207, 1977.

MATSUDA, F.; NAKAGAWA, H.; SORADA, K. Dynamic observation of solidification and solidification cracking during welding with optical microscope. **Transactions of Joining and Welding Research Institute**, Osaka, vol. 11, no. 2, pp. 67-77, 1982.

MATSUDA, F.; NAKAGAWA, H.; UEHARA, T.; KATAYAMA, S.; ARATA, Y. A new explanation for role of delta-ferrite improving weld solidification crack susceptibility in austenitic stainless steel. **Transactions of Joining and Welding Research Institute**, Osaka, vol 8, pp. 105-112, 1979.

MCLOUGHLIN, B.; HUIZINGA, S.; DE JONG, J. G.; LIEK, W. E.; PATERSON, S. J. Offshore 22Cr Duplex Stainless Steel Cracking – Failure and Prevention. In: NACE Corrosion, Houston, TX: **NACE International**, 05474, 2005.

MEOLA, C.; SQUILLACE, A.; MEMOLA, F.; MINUTOLO, C.; MORACE, R.E. Analysis of stainless steel welded joints a comparison between destructive and non-destructive techniques. **Journal of Materials Processing and Technology**, Amsterdam, vol. 155-156, pp. 1893–1899, 2004.

MODENESI, P. J.; MARQUES, P. V.; SANTOS, D. B. **Introdução à Metalurgia da Soldagem**. Belo Horizonte: Universidade Federal de Minas Gerais, Departamento de Engenharia Metalúrgica e de Materiais, 2012.

MUÑOZ, J.A.; BOLMARO, R.E.; JORGE, A.M; ZHILYAEV, A.; CABRERA, J.M. Prediction of Generation of High- and Low-Angle Grain Boundaries (HAGB and LAGB) During Severe Plastic Deformation. **Metallurgical and Materials Transactions A**, Warrendale, vol. 51A, pp. 4674–4684, 2020.

NAFFAKH, H., SHAMANIAN, M.; ASHRAFIZADEH, F. Weldability in dissimilar welds between Type 310 austenitic stainless steel and Alloy 657. **Journal of Materials Science**, New York, vol. 43, pp. 5300-5304, 2008.

NAFFAKH, H.; SHAMANIAN, M.; ASHRAFIZADEH, F. Dissimilar welding of AISI 310 austenitic stainless steel to nickel-based alloy Inconel 657. **Journal of Materials Processing Technology**, Amsterdam, vol. 209, pp. 3628-3639, 2009.

NELSON, T. W.; LIPPOLD, J. C.; MILLS, M. J. Nature and Evolution of the Fusion Boundary Ferritic-Austenitic Dissimilar Weld Metals, Part 1 — Nucleation and Growth. **Welding Research Supplement**, Miami, vol. 10, pp. 329s-337s, 1999.

NEUHARTH, J. J.; CAVALLI, M. N. Investigation of high-temperature hydrogen embrittlement of sensitized austenitic stainless steels. **Engineering Failure Analysis**, Oxford, vol. 49, pp. 49-56, 2015.

PADILHA, A. F.; RIOS, P. R. Decomposition of austenite in austenitic stainless steels. **Iron and Steel Institute of Japan International**, Tokyo, vol. 42, no. 4, pp. 325-337, 2002.

PADILHA, A.F.; PLAUT, R.L.; RIOS, P.R. Annealing of cold-worked austenitic stainless steels. **Iron and Steel Institute of Japan International**, Tokyo, vol. 43, no. 2, pp. 135-143, 2003.

PARDAL, J. M.; CARVALHO, S. S.; BARBOSA, C.; Montenegro, T. R.; TAVARES, S. S. M. Failure analysis of AISI 310S plate in an inert gas generator used in off-shore oil platform. **Engineering Failure Analysis**, Amsterdam, vol. 18, pp. 1435-1444, 2011.

PELLINI, W. S. Strain theory of hot tearing. **Foundry**, Cleveland, vol. 80, no. 11, pp. 125-133, 1952.

PLAUT, R. L.; HERRERA, C.; ESCRIBA, D. M.; RIOS, P.R.; PADILHA, A. F. A Short Review on Wrought Austenitic Stainless Steels at High Temperature. **Materials Research**, São Carlos, vol. 10, no. 4, pp. 453-460, 2007.

PROKHOROV, N. The technological strength of metals while crystallizing during welding. **Welding Production**, Cambrigde, vol. 9, no. 4, pp. 1-8, 1962.

PUGH, J. W.; NISBET, J. D. Iron-chromium-nickel ternary system. **Trans. AIME**, New York, vol. 188, pp. 268-276, 1950.

PUMPHREY, W.; JENNINGS, P. A consideration of the nature of brittleness at temperatures above the solidus in castings and welds in aluminum alloys. **Journal of the Institute of Metals**, London, vol. 75, pp. 235-256, 1948.

RAPAZZ, M.; DREZET, J.-M.; GREMAUD, M. A New Hot-Tearing Criterion. **Metallurgical and Material Transactions A**, Warrendale, vol. 30A, pp. 449-455, 1999.

RASHMI, B.; BHAVSAR, P. E. Use of Alloy 718 and 725 in Oil and Gas Industry. **The Minerals, Metals & Materials Society**, Warrendale, pp. 47 – 55, 2001.

ROTH, H.A.; DAVIS, C.L.; THOMSON, R.C. Modeling Solid Solution Strengthening in Nickel Alloys. **Metallurgical and Materials Transactions A**, Warrendale, vol. 28A, pp. 1329-1335, 1997.

ROUT, M. Texture-tensile properties correlation of 304 austenitic stainless steel rolled with the change in rolling direction. **Materials Research Express**, Bristol, vol. 7, 016563, 2020.

RUI, S.S.; HAN, Q.N.; WANG, X.; LI, S.; MA, X.; SU, Y.; CAI, Z.; DU, D.; SHI, H.J. Correlations between two EBSD-based metrics Kernel Average Misorientation and Image Quality on indicating dislocations of near-failure low alloy steels induced by tensile and cyclic deformations. **Materials Today Communications**, Amsterdam, vol. 27, 102445, 2021.

RUTTER, J. W.; CHALMERS, B. The mechanism of Dendritic Growth in Crystals. **Canadian Journal of Physics**, Ottawa, vol. 31, pp. 15–39, 1953.

SABOORI, A.; AVERSA, A.; MARCHESE, G.; BIAMINO, S.; LOMBARDI, M.; FINO, P. Microstructure and mechanical properties of AISI 316L produced by directed energy deposition-based additive manufacturing: A review. **Applied Sciences**, Basel, vol. 10, 3310, 2020.

SAFARI, A.R.; FOROUZAN, M. R.; SHAMANIAN, M. Hot cracking in stainless steel 310s, numerical study and experimental verification. **Computational Materials Science**, Amsterdam, vol. 63, pp. 182-190, 2012.

SAIDA, K.; NOMOTO, Y.; OKAUCHI, H.; OGIWARA, H.; NISHIMOTO, K. Influences of phosphorus and sulphur on ductility-dip cracking susceptibility in multipass weld metal of alloy 690. **Science and Technology of Welding and Joining**, Abingdon, vol. 17, no, 1, pp. 1-8, 2012.

SAIDA, K.; MATSUSHITA, H.; NISHIMOTO, K.; KIUCHI, K.; NAKAYAMA, J. Quantitative influence of minor and impurity elements on solidification cracking susceptibility of extra high purity type 310 stainless steel. **Science and Technology of Welding and Joining**, London, vol. 18, no 7, pp. 616-623, 2013.

SANTILLANA, B.; BOOM, R.; ESKIN, D.; MIZUKAMI, H.; HANAO, M.; KAWAMOTO, M. High-Temperature Mechanical Behavior and Fracture Analysis of a Low-Carbon Steel Related to Cracking. **Metallurgical and Material Transactions A**, Warrendale, vol. 43A, pp. 5048-5057, 2012.

SANTOS, G. E.; MINÁ, E. M.; PEQUENO, D. A. C.; MIRANDA, H. C.; SILVA, C. C. Evaluation of solidification cracking of Ni-based alloy dissimilar welds based on Trans-Varestraint test. **Welding in the World**, Roissy-Charles-de-Gaulle, vol. 65, pp. 1696-1982, 2021.

SAVAGE, W. F.; LUNDIN, C. D. The Varestraint Test. **Welding Journal**, Miami, vol. 10, pp. 433s-442s, 1965.

SAVAGE, W. F.; NIPPES, E. F.; SZEKERES, E. S. Study of weld interface phenomena in a low alloy steel. **Welding Journal**, Miami, vol. 55, no. 9, pp. 260s-268s, 1976.

SCHAEFFLER, A. L. Constitution diagram for stainless steel weld metal. **Metal Progress**, s.l., vol. 56, no. 11, pp. 680-680b, 1949.

SCHEIL, E. Bemerkungen zur schicht kristallbildung. **Z. Metallkunde**, München, vol. 34, no. 3, pp. 70-72, 1942.

SCHERER, R.; RIEDRICH, G.; HOUGARDY, H. **US Patent 2,240,672**, Washington, D.C.: United States Patent Office, 1941.

SENDA, T.; MATSUDA, F.; TAKANO, G.; WATANABE, K.; KOBAYASHI, T.; MATSUZAKA, T. Fundamental investigations on solidification crack susceptibility for weld metals with Trans-Varestraint test. **Trans. Jpn. Weld. Soc.**, Tokyo, vol. 2, pp. 1-22, 1971.

SHANKAR, V.; GILL, T. P. S.; MANNAN, S. L.; SUNDARESAN, S. Solidification cracking in austenitic stainless steel welds. **Sadhānā**, Bangalore, vol. 28 (3 & 4), pp. 359-382, 2003.

SHORE, D. Making the flare safe. **Journal of Loss Prevention in the Process Industries**, Oxford, vol. 9, no. 6, pp. 363-381, 1996.

SILVA, C.C.; AFONSO, C.R.M.; RAMIREZ, A.J.; MOTTA, M.F.; DE MIRANDA, H.C. Aspectos Metalúrgicos de Revestimentos Dissimilares com a Superliga à Base de Níquel Inconel 625. **Rev. Soldag. Insp.**, São Paulo, vol. 17, pp. 251-263, 2012.

SILVA, C.C.; DE MIRANDA, H.C.; DE SANT'ANA, H.B.; FARIAS, J.P. Austenitic and ferritic stainless steel dissimilar weld metal evaluation for the applications as-coating in the petroleum processing equipment. **Materials and Design**, Amsterdam, vol. 47, pp. 1-8, 2013.

SRINIVASAN, G.; BHADURI, A. K.; SHANKAR, V.; RAJ, B. Evaluation of hot cracking susceptibility of some austenitic stainless steels and a nickel-base alloy. **Welding in the World**, Roissy-Charles-de-Gaulle, vol. 52, pp. 4–17, 2008.

STATHARAS, D.; ATKISON, H.; THORNTON, R.; MARSDEN, J.; DONG, H.; WEN, S. Getting the Strain Under Control: Trans-Varestraint Tests for Hot Cracking Susceptibility. **Metallurgical and Materials Transactions A**, Warrendale, vol. 50A, pp. 1748-1762, 2019.

STEFANESCU, D.M.; RUXANDA, R. **Fundamentals of Solidification, Metallography and Microstructures**. Ohio: ASM International. 2004. ISBN 9781615834150

STEWART, M. **Surface Production Operations, Chapter 6 – Fabrication, Welding, and In-shop Inspection**. Oxford: Gulf Professional Publishing, 2021. pp. 197–284.

STOJAKOVIC, D. Electron backscatter diffraction in materials characterization. **Processing and Application of Ceramics**, Novi Sad, vol. 6, pp. 1-13, 2012.

SUTTON, B. J. **Solidification Behavior and Hot Cracking Susceptibility of High Manganese Steel Weld Metals**. 2013. 140 pp. Master Degree Thesis (Graduate Program in Welding Engineering) — Graduate School of The Ohio State University, Ohio, 2013.

SUUTALA, N.; TAKALO, T.; MOISIO, T. Ferritic-Austenitic Solidification Mode in Austenitic Stainless Steel Welds. **Metallurgical Transactions A**, Ohio, vol. 11A, pp. 717-725, 1980.

TAKALO, T.; SUUTALA, N.; MOISIO, T. Austenitic Solidification Mode in Austenitic Stainless Steel Welds. **Metallurgical Transactions A**, Ohio, vol. 10A, pp. 1173-1181, 1979.

TAVARES, S. S. M.; MOURA, V.; COSTA, V. C.; FERREIRA, M. L. R.; PARDAL, J. M. Microstructural changes and corrosion resistance of AISI 310S steel exposed to 600-800 °C. **Material Characterization**, New York, vol. 60, pp. 573-578, 2009.

TAYLOR, G.I. Plastic strain in metals. **Journal of the Institute of Metals**, London, vol. 62, pp. 307-324, 1938.

TILLER, W. A.; JACKSON, K. A.; RUTTER, J. W.; CHAMLER, B. **Acta Met.**, Oxford, vol. 1, 1953.

VITEK, J. M.; DASGUPTA, A.; DAVID, S. A. Microstructural modification of austenitic stainless steels by rapid solidification. **Metallurgical Transactions A**, Ohio, vol. 14, pp. 1833-1841, 1983.

VYAZOVKIN, S. **Isoconversional Kinetic of Thermally Stimulated Processes**. 1st ed. Cham: Springer, 2015.

WANG, D.; SAKODA, S.; KADOI, K.; SHINOZAKI, K.; YAMAMOTO, M. Investigation of Evaluation Method for Hot Cracking Susceptibility of 310S Stainless Steel during Laser Welding using Trans-Varestraint Test. **Quarterly Journal of the Japan Welding Society**, Tokyo, v. 33, n. 2, p. 39s–43s, 2015.

WRIGHT, S.I.; NOWELL, M.M.; FIELD, D.P. A Review of Strain Analysis Using Electron Backscatter Diffraction. **Microscopy and Microanalysis**, Cambridge, vol. 17, pp. 316-329, 2011.

WU, W.; TSAI, C. H. Hot Cracking Susceptibility of Fillers 52 and 82 in Alloy 690 Welding. **Metallurgical and Materials Transactions A**, Warrendale vol. 30A, pp. 417-426, 1999.

YOUSEFI, M.; FARGHADIN, M.H.; FARZADI, A. Investigate the causes of cracks in welded 310 stainless steel used in the Flare tip. **Engineering Failure Analysis**, Oxford, vol. 53, pp. 138-147, 2015.

ZHANG, S.; SHI, X.; LIANG, Y.; XU, H.; YAN, C.; YAN, W.; RONG, L. YANG, K. χ phase and its effect on the mechanical properties of a Mo-bearing high-Si austenitic stainless steel after aging at 650 °C. **Journal of Materials Research and Technology**, São Paulo, vol. 23, pp. 4280-429, 2023.

ZHANG, Y.; YANG, J. Formation of Nb(C,N) Carbonitride in Cast Austenitic Heat-Resistant Steel during Directional Solidification under Different Withdraw Rates. **Materials**, Basel, vol. 11, 2397, 2018.

ZHOU, Y.; LI, Y.; LIU, Y.; GUO, Q.; LIU, C.; YU, L.; LI, C.; LI, H. Precipitation behavior of type 347H heat-resistant austenitic steel during long-term high-temperature aging. **Journal of Materials Research**, Pittsburgh, vol. 30, no. 3, pp. 3642- 3652, 2015.

ZIELIŃSKI, A.; WERSTA, R.; SROKA, M. The study of the evolution of the microstructure and creep properties of Super 304H austenitic stainless steel after aging for up to 50,000 h. **Archives of Civil and Mechanical Engineering**, Warsaw, vol. 22, no. 89, 2022.